An ultracold, optically trapped mixture of ^{87}Rb and metastable ^{4}He atoms

509242-L-bw-Flores
Processed on: 3-4-2017

This thesis was reviewed by:

prof.dr. L. Visscher	VU Amsterdam
prof.dr. F. Schreck	UvA Amsterdam
prof.dr. J.J. Arlt	Aarhus University
prof.dr. S.Y.T. van de Meerakker	Radboud University Nijmegen
dr. D. Clément	Institut d′Optique, CNRS, Universite Paris Palaiseau

ISBN: 978-94-028-0622-9

Cover photo is a mixture of marbles in a shallow sand burrow. Photo taken by Xavier Bacalla.
Simplified summary at the back cover edited by Mary Jane Flores, Marian Salumbides, Albert Licup, and Edcel Salumbides.

This work is part of the research programme of the 'Stichting voor Fundamenteel Onderzoek der Materie' (FOM), which is financially supported by the 'Nederlandse Organisatie voor Wetenschappelijk Onderzoek' (NWO). The research was performed at the LaserLab of the Vrije Universiteit Amsterdam.

509242-L-bw-Flores
Processed on: 3-4-2017

VRIJE UNIVERSITEIT

An ultracold, optically trapped mixture of ^{87}Rb and metastable ^{4}He atoms

ACADEMISCH PROEFSCHRIFT

ter verkrijging van de graad Doctor aan
de Vrije Universiteit Amsterdam,
op gezag van de rector magnificus
prof.dr. V. Subramaniam,
in het openbaar te verdedigen
ten overstaan van de promotiecommissie
van de Faculteit der Exacte Wetenschappen
op woensdag 31 mei 2017 om 9.45 uur
in de aula van de universiteit,
De Boelelaan 1105

door

Adonis Silva Flores

geboren te Cebu, Filipijnen

promotor:	prof.dr. W.M.G. Ubachs
copromotoren:	dr. S. Knoop
	dr. W. Vassen

509242-L-bw-Flores
Processed on: 3-4-2017

To my wife Mary Jane

You are an essential variable in an equation of my life. You keep the balance when the other side seems to be lost.

509242-L-bw-Flores
Processed on: 3-4-2017

509242-L-bw-Flores
Processed on: 3-4-2017

Contents

1 Introduction **1**
- 1.1 Ultracold atomic gases . . . 3
- 1.2 Ultracold mixtures . . . 5
- 1.3 Metastable He and Penning ionization . . . 5
- 1.4 He^*+alkali mixtures . . . 7
- 1.5 $^4He^*+^{87}Rb$ . . . 9
- 1.6 Outline of this thesis . . . 10

2 Experimental background **11**
- 2.1 Overview of experimental approach . . . 13
- 2.2 Laser systems . . . 15
- 2.3 Two-species magneto-optical trap . . . 17
- 2.4 Evaporative cooling in the quadrupole magnetic trap . . . 19
  - 2.4.1 Radio-frequency source . . . 19
  - 2.4.2 Microwave source . . . 20
- 2.5 Hybrid trap and optical dipole trap . . . 22
- 2.6 Detection scheme . . . 28
  - 2.6.1 Absorption imaging . . . 28
  - 2.6.2 Microchannel plate detection . . . 31
- 2.7 Preparation of different spin-states . . . 33
  - 2.7.1 Rapid adiabatic passage . . . 33
  - 2.7.2 RF and MW sweeps . . . 34

3 Simple method for producing Bose-Einstein condensates of metastable helium using a single-beam optical dipole trap **37**
- 3.1 Introduction . . . 39
- 3.2 Single-beam hybrid trap for $^4He^*$ . . . 40
- 3.3 Experimental setup . . . 43
- 3.4 Results . . . 46
  - 3.4.1 Loading of HT or ODT . . . 46
  - 3.4.2 Control of QMT displacement in HT . . . 48
  - 3.4.3 Evaporative cooling in HT and ODT . . . 49

3.5 Conclusions 55

4 An ultracold, optically trapped mixture of ^{87}Rb and metastable ^{4}He atoms 57
4.1 Introduction 59
4.2 Experiment 60
4.2.1 Two-species MOT 62
4.2.2 Simultaneous evaporative cooling in the QMT 63
4.2.3 Transfer to single-beam ODT 66
4.2.4 Dual absorption imaging and MCP detection 69
4.2.5 Preparation of different spin-states 70
4.3 Lifetimes in optical dipole trap 70
4.4 Conclusions and prospects 72

5 Quantum-state-controlled Penning-ionization reactions between ultracold alkali and metastable helium atoms 75
5.1 Introduction 77
5.2 Experiment 79
5.3 Interspecies two-body loss rate 80
5.4 Comparison with multichannel quantum-defect theory 83
5.5 Conclusions 85
Appendix A: Doublet character 85
Appendix B: Finite temperature correction 88
Appendix C: Spin-exchange collisions 89
Appendix D: Overview of loss rates 90

6 Outlook 93
6.1 Highlights 95
6.2 Towards a dual-species BEC in a single-beam ODT 96
6.3 Prospect for interspecies Feshbach resonances 97

Bibliography 101

List of Publications 117

Summary 119

Samenvatting 123

Acknowledgements 127

Chapter 1

Introduction

In this chapter, a brief introduction on (ultra)cold atom experiments is given, starting with the early experiments on laser cooling, the realization of quantum degenerate atomic samples, and the evolution of the field to include experiments with ultracold heteronuclear mixtures. A description about the atomic species used in our experiment, namely helium (in its metastable triplet state) and alkali atoms (in particular Rb), is presented.

509242-L-bw-Flores
Processed on: 3-4-2017

509242-L-bw-Flores
Processed on: 3-4-2017

1.1 Ultracold atomic gases

Experiments with cold neutral atoms started around the 1980's with the demonstration of laser cooling of sodium atoms [1–6]. Immediately, the topic attracted fast growing interest, and with the demonstration of various cooling and trapping techniques such as Doppler cooling [7], magneto-optical trapping [8] and evaporative cooling in a magnetic trap [9, 10], neutral atoms could be confined with average velocities close to zero and sample temperatures were pushed down below 1 mK, which is called the ultracold regime. In 1997, the Nobel prize in Physics was awarded jointly to Steven Chu, Claude Cohen-Tannoudji and William Phillips for their pioneering work on laser cooling. In 1995, the group of Cornell and Wieman and the group of Ketterle demonstrated cooling of a dilute gaseous sample containing neutral atoms (Rb: NIST group [11] and Na: MIT group [12]) to temperatures of a few μK down to a few hundreds of nK, reaching a new state of matter known as a Bose-Einstein condensate (BEC). In 2001, the Nobel prize in Physics was also awarded jointly to Eric Cornell, Carl Wieman and Wolfgang Ketterle for their work on realizing and characterizing a BEC. The success of cooling down neutral atoms towards BEC owes mainly to the efficiency of the evaporative cooling technique, which relies on sufficiently fast rethermalization by means of elastic collisions between the trapped atoms. Bose-Einstein condensation occurs when an ensemble of identical particles with integer spin (bosons) are cooled down to ultralow temperature where the interatomic separation becomes comparable to or smaller than the de Broglie wavelength such that the individual atomic wave functions overlap, and a significant fraction of the ensemble occupies the lowest available quantum state. In contrast, particles with half-integer spin (fermions) obey the Pauli exclusion principle, and are governed by Fermi-Dirac statistics. The evaporative cooling technique applicable to bosons does not directly apply to fermionic species, simply because at ultralow temperature, indistinguishable fermions do not collide. Nonetheless, it did not take long before cooling a fermionic species to quantum degeneracy was also reported. In 1999, DeMarco and Jin demonstrated quantum degeneracy of fermionic potassium (^{40}K) using the same laser cooling and magnetic trapping techniques applied for bosons, however, using two distinguishable Zeeman states [13].

While the first BECs and quantum degenerate Fermi gases (DFGs) were realized in a magnetic trap, there have been efforts and proposals in the earlier development of the field to prepare cold atom samples in an optical trap [14]. Among the various motivations is that, in contrast to a magnetic trap, an optical trap can in principle provide confinement independent of the spin-state, thereby allowing trapping of high-field seeking states and zero magnetic moment atoms such as the alkaline-earth. Another example is the case of Cs, for which evaporative cooling in a magnetic trap is not favorable because of strong two-body losses [15]. First principles of pure

optical trapping were already introduced in 1986 by Steven Chu [16] but it was only until 1998 that the first realization of trapping a BEC in an optical dipole trap was reported by the group of Ketterle [17]. It was a significant breakthrough, and was immediately followed by the observation of magnetically induced Feshbach resonances [18], for which a trapping potential that is independent of magnetic field is essential. A Feshbach resonance occurs when the energy of a colliding atom pair becomes degenerate with a bound molecular state, and for ultracold atoms such a resonance can be induced by an applied magnetic field. A comprehensive discussion about Feshbach resonances in ultracold atomic gases can be found in the review paper by Chin *et al.* [19]. Around a Feshbach resonance, the elastic and inelastic collision properties are strongly modified, opening the realization of BEC for atomic species that have unfavorable collision properties at zero magnetic field, such as ^{85}Rb [20] and Cs [21], and more generally gives rise to quantum gases with tunable interaction strength. Furthermore, because of the coupling with a bound molecular state, Feshbach resonances can be used to associate ultracold molecules from ultracold atoms [22, 23], which paved the way for the creation of ultracold ground state molecules [24–26].

Several atomic species (bosonic and fermionic) have been cooled down to quantum degeneracy including all the stable alkali isotopes [11–13, 20, 21, 27–30]. An alkali atom has a relatively simple electronic structure with a single valence electron. Laser cooling can be easily applied in which only one additional laser is needed for repumping due to the presence of hyperfine structure. Later, quantum degenerate samples of alkaline-earth (Sr [31] and Ca [32]), metastable He [33–36], Cr [37] and lantanides (Yb [38, 39], Dy [40, 41] and Er [42]) were also realized.

The ultracold regime offers exquisite control over the internal and external quantum degrees of freedom. This makes ultracold atomic gases an ideal platform to study various fascinating physical phenomena. One example in few-body physics is the observation of Efimov quantum states using an ultracold sample of Cs atoms [43]. A review about the application of ultracold atoms to study few-body system can be found in the paper by Wang *et al.* [44]. Ultracold atomic samples also offer a range of applications in many-body physics (see e. g. review paper by Bloch *et al.* [45]), for instance in quantum simulations, such as experiments with optical lattices to simulate condensed-matter systems (e. g. the study of the superfluid to Mott insulator transition [46]). A review about quantum simulations with ultracold gases can be found in the article by Bloch *et al.* [47]. Furthermore, ultracold samples have also been used for high precision spectroscopy, in which a good handle on the systematics (e. g. precise knowledge of the lineshape) and long interaction times are possible, allowing to probe very weak transitions [48, 49].

1.2 Ultracold mixtures

Experiments with ultracold atoms have been extended to mixtures of chemically distinct atomic species. In general, working with ultracold mixtures poses additional experimental challenges because in principle it requires twice the infrastructure for laser cooling as compared to the single species. There are also additional losses in a magneto-optical trap (MOT) due to interspecies inelastic collisions [50, 51]. More often, the distinct magnetic properties of the atomic species involved put additional constraints for forced evaporative cooling in a magnetic trap. Another example is the separation of the atomic clouds caused by a differential gravitational sag. Still, ultracold mixtures offer fascinating scientific opportunities. To name a few, for atomic species in which typical evaporative cooling will not work (like fermions or bosons with unfavorable collision properties), it enables the realization of ultracold samples via sympathetic cooling with another species [28, 52, 53]. Another example is the creation of ultracold heteronuclear molecules (via association of two distinct ultracold atomic species), that can possess an electric dipole moment [25], in contrast to homonuclear molecules. Ultracold mixtures have also been used to study impurities immersed in Bose or Fermi gases [54–56], and testing the universality for free-fall [57].

Mostly, ultracold mixtures of chemically distinct atomic species consist of alkali atoms [28, 52, 58–65]. These experimental efforts laid the foundation for the creation of ultracold heteronuclear ground-state molecules, which possess a large permanent dipole moment: KRb [25], RbCs [66, 67], NaK [68] and NaRb [69]. Another example is the observation of successive Efimov states in Li+Cs [70, 71], benefiting from the largest possible mass ratio within the alkali group. Recently, mixtures of alkali and alkaline-earth [72] or Yb [73–77] atoms have also been reported where the main interest comes from the doublet $^2\Sigma^+$ molecular ground state potential that gives rise to both electric and magnetic tunability of the associated molecules, in contrast to the singlet $^1\Sigma^+$ ground state potential of bialkali molecules.

The main goal of this thesis is to realize an optically trapped ultracold mixture of an alkali and helium in the metastable triplet $2\,^3S_1$ state (denoted as He*). Ultracold mixtures of alkali atoms and fermionic ^{3}He* or bosonic ^{4}He* provide new Bose-Bose, Bose-Fermi and Fermi-Fermi mixtures, with an extended range of possible mass ratios.

1.3 Metastable He and Penning ionization

The two naturally occurring abundant isotopes of He are ^{3}He (fermion) and ^{4}He (boson). In our experiment, we are only using bosonic ^{4}He. Thus, the succeeding sections and chapters only refer to ^{4}He unless otherwise specified. The He atom, having only two electrons, has a relatively simple electronic

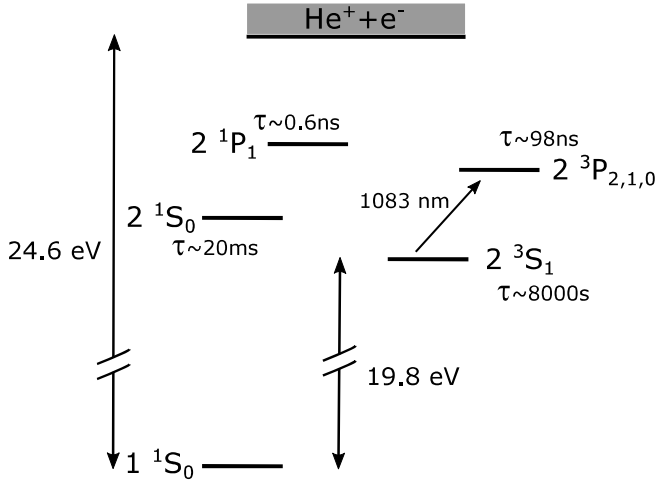

Figure 1.1: Energy level scheme of the first few states of the He atom. The metastable triplet state and the ionization limit lie 19.8 eV and 24.6 eV, respectively, above the ground state.

structure (see Fig. 1.1 for the energy level scheme of the first few states of the He atom). In contrast to alkali atoms, laser cooling of He in its ground state is not (yet) possible as the required wavelength is in the extreme ultraviolet. However, one can use the metastable triplet state $2\ ^3S_1$ (He*), which can be accessed using a dc-discharge. The lifetime of this metastable state is about 8000 s, which is more than sufficient to perform laser cooling and subsequent trapping experiments. For laser cooling, the $2\ ^3S_1 \rightarrow 2\ ^3P_2$ transition at 1083 nm can be used, for which fiber lasers are available.

An important feature of He* is the high internal energy of 19.8 eV, enough to ionize almost any atom or molecule, in a process that is known as Penning ionization (PI). For ultracold He* samples, collisions between He* atoms are relevant, where besides PI (leading to a ground state neutral He atom and a He ion) also a molecular ion via associative ionization (AI) can be formed:

$$\mathrm{He^* + He^* \rightarrow \begin{cases} He + He^+ + e^- \\ He_2{}^+ + e^- \end{cases}} \tag{1.1}$$

These strong two-body inelastic processes, to which we both refer to as PI, lead to trap loss. Initial experiments with He* in a MOT suffered from strong PI loss, limiting the number of atoms in the trap on the order of 10^4 [78]. However, later experiments demonstrated that using a large capture volume and far-detuned laser cooling light allows trapping of at least 10^7 [79] and up to 10^9 [80] atoms in a MOT. Moreover, it was also shown that PI can be suppressed by several orders of magnitude in spin-polarized samples due

to spin conservation [81–83]. This can be explained as follows: A He* atom has a total electron spin $s = 1$ thus the left side of the PI reaction described in Eq. 1.1 can in principle carry a total spin $S = 0, 1, 2$ (corresponding to the singlet, triplet or quintet interaction potentials, respectively). The right hand side (product side) of the PI reaction however can only carry $S = 0, 1$. Thus, PI can only proceed via the singlet ($S = 0$) or triplet ($S = 1$) potentials, and is forbidden for the case of pure quintet scattering ($S = 2$). Evaporative cooling is also favorable (for the bosonic ^{4}He*+^{4}He*) because of the large quintet scattering length $a = 142a_0$ [84], where a_0 is the Bohr radius. In 2001, realization of ^{4}He* BEC's were reported [33, 34]. In 2006, DFG of ^{3}He* was also realized using ^{4}He* to sympathetically cool ^{3}He* [36]. To suppress PI, a pure quintet spin-state combination is also necessary for the ^{3}He*+^{4}He* mixture. Note that the scheme of using two distinguishable Zeeman states as for instance applied for the fermionic ^{6}Li and ^{40}K will not work for ^{3}He* due to the presence of PI loss. The large internal energy of 19.8 eV also provides additional detection schemes that are not possible for other atomic species, most prominently, one can use microchannel plates (MCP). A overview on (ultra)cold metastable noble gas experiments, with an emphasis on He*, can be found in a review paper by Vassen *et al.* [85].

1.4 He*+alkali mixtures

With He* having electron spin $s = 1$ and an alkali atom with electron spin $s = 1/2$, the scattering properties of a He*+alkali mixture are described by two interaction potentials, namely the shallow quartet $^4\Sigma^+$ (total spin $S = 3/2$) and the much deeper doublet $^2\Sigma^+$ (total spin $S = 1/2$) potentials (see Fig. 1.2 for the specific case of He*+Rb). In addition, similar to the homonuclear He* case, there is also the possibility of Penning ionization:

$$\mathrm{He}^* + \mathrm{A} \rightarrow \begin{cases} \mathrm{He} + \mathrm{A}^+ + \mathrm{e}^- \\ \mathrm{HeA}^+ + \mathrm{e}^- \end{cases} \tag{1.2}$$

leading to trap loss. The left hand side of the PI reaction in Eq. 1.2 can carry a total spin $S = 1/2$ or $S = 3/2$ while the right hand side can only carry $S = 1/2$. Thus, like in the homunuclear case, PI can be also suppressed if the mixture is prepared in the doubly spin-stretched spin-state combinations corresponding to a magnetic and hyperfine quantum numbers as $|m_s = \pm 1\rangle_{\mathrm{He}^*} + |f = f_{\max}, m_f = \pm f_{\max}\rangle_{\mathrm{A}}$, where $f_{\max} = i + 1/2$ and i is the nuclear spin of the alkali isotope. This combination corresponds to pure quartet scattering. Here, the main assumption is that the first excited ionic state is not accessible, which is true for all alkali atoms except Cs, where the energy of the first excited ionic state is only 17.2 eV [86]. PI proceeds predominantly via the doublet interaction potential. The possibility of suppression of PI for particular spin-state combinations is quite unique,

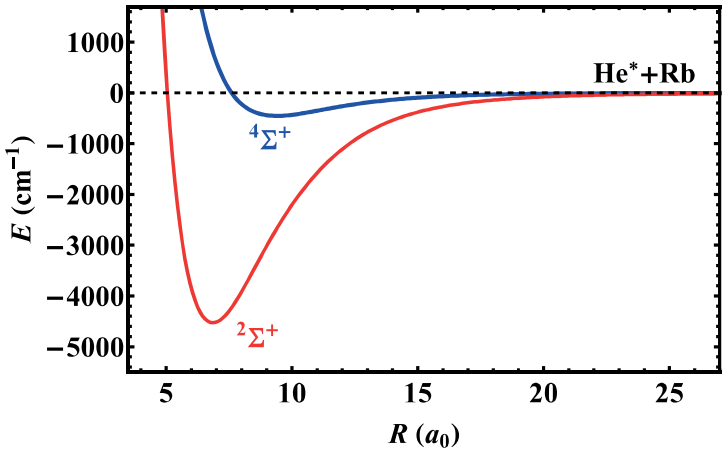

Figure 1.2: Doublet $^2\Sigma^+$ (red) and quartet $^4\Sigma^+$ (blue) interaction potentials for the case of He*+Rb. The quartet potential is an exact trace based on *ab initio* calculation [87, 88] while the doublet potential is an approximate trace based on the position of the minimum energy and well depth [89].

present in He*+He*, He*+H and He*+alkali collisions, but not for various other combinations with He* like with the alkaline-earth atoms. The stable doubly spin-stretched spin-state combination can be used for the preparation stage to reach the ultracold regime, possibly reaching doubly quantum-degenerate mixtures. However, the study of Feshbach resonances or Penning ionization requires a mixture with scattering properties given by both doublet and quartet potentials. Feshbach resonances are in principle possible for this collision system due to the hyperfine coupling between the doublet and quartet interaction potentials.

Previous experimental studies of He*+alkali collisions have been performed at thermal energies in stationary afterglow and merged-beam experiments (see e. g. [89, 90]). It must be noted that here only the doublet potential is being probed because the measurements were based from electron spectra and/or losses that are related to PI. In contrast, experiments with ultracold gases allow to also probe the quartet potential via measurement of elastic cross-sections [88]. Recently, quartet scattering lengths for the various He*+alkali mixtures, obtained from *ab initio* calculations, became available [87]. *Ab initio* calculations of the doublet potential are not yet available. These are much more challenging than the quartet ones, because the PI channel needs to be implemented. But even without PI, the possible accuracy of doublet scattering lengths will be much less, as the doublet potentials are much deeper than the quartet ones (at least a factor of

10) [89], leading to a higher sensitivity of the calculated potentials to the scattering lengths.

1.5 ^{4}He*+^{87}Rb

For the alkali partner, ^{87}Rb was chosen for two main reasons. First, it is experimentally convenient to prepare via standard laser cooling and trapping techniques, and therefore has been used extensively in various (ultra)cold atom experiments, including several mixtures. Second, among the various atoms in the alkali group (excluding Cs because the spin-stretched state suffers from strong two-body loss), Rb provides the highest mass ratio which is an interesting feature for a heteronuclear mixture (see e. g. [70, 71]).

Prior to the start of our experiment (2011), not much was known about the interaction potentials and collisional properties of He*+Rb. The first simultaneous laser cooling and trapping of ^{4}He* and ^{87}Rb was demonstrated by the Truscott group [91], and they measured an interspecies two-body loss rate of $(6 \pm 2) \times 10^{-10}$ cm^{3}s^{-1} in a magneto-optical trap. They had also demonstrated pure magnetic trapping of the low-field seeking doubly spin-stretched spin-state combination, and measured an upper limit of the PI rate of $L_2 = 5 \times 10^{-12}$ cm^{3}s^{-1} for pure quartet scattering by comparing the ion production signal with and without the presence of Rb [92]. In the first stage of our experiment, we performed magnetic trapping of the doubly spin-stretched spin-state and measured the time evolution of the number of atoms and temperatures of the sample in the trap, in which we were able to extract an upper limit for the pure quartet two-body loss rate of $L_2 = 1.5 \times 10^{-12}$ cm^{3}s^{-1} [88]. In addition, from the thermalization measurements, we were also able to extract the elastic cross-section and found a small quartet scattering length [88], in agreement with *ab initio* calculations of the quartet $^4\Sigma^+$ potential [87, 88]. As already mentioned in Section 1.4, the knowledge on the doublet $^2\Sigma^+$ potential is limited [89], and the doublet scattering length is unknown.

In principle, the two Rb (85 and 87) and two He* (3 and 4) isotopes provide four possible mixture combinations. However, the small interspecies quartet scattering length of these combinations [87] will limit the efficiency of sympathetic cooling, which already excludes the possibility of using fermionic ^{3}He*. The small quartet scattering length for the case of ^{4}He*+Rb means that forced evaporative cooling on both species is required. Forced evaporative cooling is much easier for ^{87}Rb than for ^{85}Rb, so a mixture of ^{4}He* with ^{85}Rb is also not favorable.

1.6 Outline of this thesis

In **Chapter 2**, a description about the experimental strategy is presented. These include: the laser systems, cooling and trapping techniques, detection schemes and technical details of the electronics used for evaporative cooling.

In **Chapter 3**, experimental details and results about the realization of a ^{4}He* BEC are presented. Here, of particular interest is the discussion on the application of a simple method, known as the hybrid trap to light atomic species such as He. Prior to this work, such technique was only applied to heavy atomic species.

In **Chapter 4**, results of loading both He* and Rb into a pure optical trap are discussed, highlighting the comparison between single- and two-species loading.

In **Chapter 5**, results demonstrating control of Penning ionization reactions via internal state preparation of He* and Rb are discussed.

In **Chapter 6**, a general summary and outlook about our experiment and prospects towards dual-species BEC and Feshbach spectroscopy are outlined.

Chapter 2

Experimental background

In this chapter, an overview of our experiment to realize an ultracold optically trapped mixture of ^{87}Rb and metastable ^{4}He is presented. The laser systems implemented for laser cooling and optical trapping, and the microwave and radiofrequency sources used for the evaporative cooling and preparation of the different spin-states are described. General descriptions about the trap configurations used are given while details regarding their implementation for specific experiments are discussed in the succeeding chapters. The detection schemes to measure atom number and temperature are also explained.

509242-L-bw-Flores
Processed on: 3-4-2017

2.1 Overview of experimental approach

Experiments with ultracold ($T < 1$ mK) neutral atoms rely mostly on laser cooling and subsequent evaporative cooling. In laser cooling, atoms are slowed down or cooled by repeated absorption and emission of photons from a red-detuned laser beam propagating opposite to the direction where the atoms are moving [93]. When performed with six laser beams for all directions and combined with a magnetic field, the atoms can be confined with temperatures close to absolute zero. An example of this scheme is a three-dimensional magneto-optical trap (3D-MOT) [8]. Typical configuration consists of three retro-reflected red-detuned laser beams combined with a magnetic field gradient from a pair of coils in anti-Helmholtz configuration. In the 3D-MOT, atoms are laser-cooled and trapped to temperatures in the order of mK down to a hundred μK.

To achieve even colder samples, trapping in a pure magnetic potential (magnetic trap) is usually implemented in which evaporative cooling can be performed on the sample. Here, the magnetic potential is truncated in a controlled way, with microwave (MW) or radiofrequency (RF) radiation that couples trappable states to non-trappable states, such that the more energetic atoms can escape from the trap while the remaining atoms rethermalize to a much lower temperature. Magnetic traps, however can only confine atoms in low-field seeking magnetic substates. There are various magnetic trap configurations and the simplest is the quadrupole magnetic trap (QMT) [94]. One major drawback of a QMT is the existence of a zero magnetic field at the trap center in which the atoms can undergo so called Majorana spin-flips, leading to transition to non-trappable spin-sates and therefore trap loss. This also limits the temperature that can be achieved in a QMT, because colder atoms spend more time at the center of the trap, and are more likely to undergo these spin-flips. Their rate scales inversely with mass and is therefore more pronounced for light atomic species [9, 95].

Another possibility to confine atoms is optical trapping [16, 96]. In its simplest form, an optical trap is a high power far off-resonant Gaussian laser beam focused to a waist of a few tens to hundreds of micrometers. The atom in the vicinity of the focus experiences a force due to the huge intensity gradient. This creates a dipole potential for the atom, and thus the commonly used term optical dipole trap (ODT). In contrast to magnetic traps, a far off-resonant ODT can provide confinement that is independent of the spin-state. Mostly, crossed-beam ODT's in which focused laser beams are crossed and atoms are trapped in the intersection region are utilized, offering tighter confinement as compared to single-beam ODT's.

Recently, a technique based on combining a single-beam ODT and a weak QMT, i. e. a hybrid trap, was introduced [97]. The addition of the weak QMT provides extra confinement along the axial direction of the single-beam ODT. In here, the QMT gradient is chosen to be slightly below the

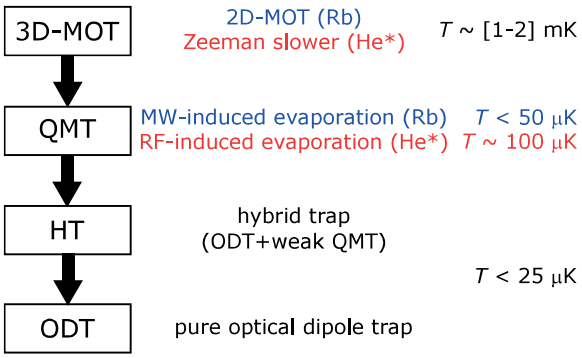

Figure 2.1: Overview of the experimental scheme to realize an ultracold mixture of Rb and He* in an optical trap (see text). The typical temperature T for the different trapping stages are also indicated.

gradient at which the magnetic force balances gravity, i. e. the levitation gradient, to ensure that atoms are confined in the hybrid trap and not by the QMT. In addition, the single-beam ODT is aligned slightly away from the QMT center to avoid Majorana spin-flips.

Our experiment utilizes standard laser cooling techniques, and the optical and magnetic trapping configurations mentioned above. In this chapter, a general description of the various traps and cooling scheme will be given only in the context as they are used in the experiment. A detailed discussion about laser cooling and the magneto-optical trap can be found in the book by Metcalf and van der Straten [98]. A comprehensive review about magnetic trapping and evaporative cooling can be found in the paper by Ketterle and van Druten [99]. Optical dipole traps are explained in the review paper by Grimm *et al.* [100].

Our goal is to realize an ultracold mixture of ^{87}Rb and metastable ^{4}He in an optical dipole trap. For this, a few trap configurations are implemented and sequentially applied (see Fig. 2.1). First, the two species are loaded and laser cooled in a 3D-MOT. He* atoms are loaded from a Zeeman slower in which they are slowed down to velocities in the order of a few 10 m/s. A detailed description of our Zeeman slower can be found in the thesis by Stas [101]. Rb atoms are loaded from a two-dimensional magneto-optical trap (2D-MOT), which is added on top of the main chamber of an existing He* setup [102]. In the 2D-MOT, laser cooling is performed only in two directions forming a cold beam of atoms along the other direction. Afterward, the sample is transferred into a QMT in which forced evaporative cooling of Rb and He* is performed using MW and RF, respectively. Lastly, the mixture is loaded into a single-beam ODT using the hybrid trap as an intermediate stage.

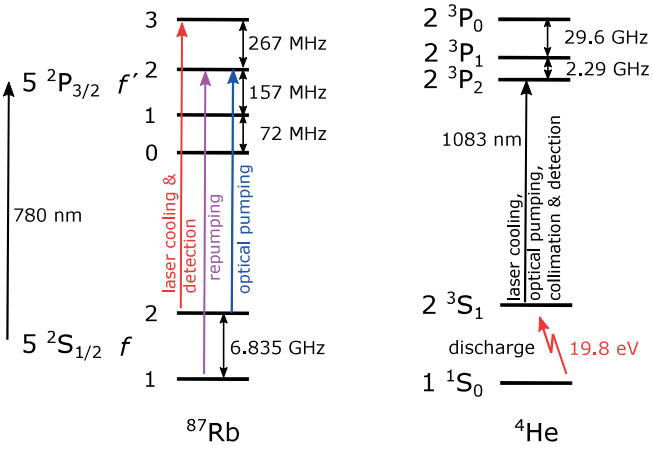

Figure 2.2: (Left) Hyperfine structure splittings of ^{87}Rb and (right) fine structure splittings of ^{4}He showing the different optical transitions used in the experiment. The metastable state of ^{4}He is accessed using a dc-discharge.

2.2 Laser systems

In Fig. 2.2, the hyperfine structure splittings of ^{87}Rb (left) and fine structure splittings of ^{4}He (right) are shown, indicating the different optical transitions used in the experiment. For laser cooling of ^{87}Rb, we use a Toptica diode laser with tapered amplifier (TA pro) operating at 780 nm. The 2 W output power is distributed over the MOT, optical pumping (OP), pushing and absorption imaging beams (see Fig. 2.3(a)). Due to the hyperfine structure of Rb, repumper beams are also needed in order to keep the atoms in the laser cooling cycle. We use a Toptica (DL 100) diode laser at 780 nm for the repumping with an output of 100 mW. For ^{4}He*, the 1083 nm light is derived from a 2 W Nufern fiber amplifier seeded with a narrowband fiber laser (NKT Koheras Adjustik). The output power is distributed to the 3D-MOT, optical pumping/imaging, Zeeman slowing and collimation beams (see Fig. 2.3(b)). No repumper is needed for ^{4}He* due to the absence of hyperfine structure. The laser beams pass through an acousto-optic modulator (AOM) either in a single- or double-pass configuration in order to allow for fast switching and precise control of the power and detuning. The double-pass configuration is necessary in order to avoid misalignment of beam output when tuning over a considerable range of frequencies [103]. The beams are delivered to the setup using polarization maintaining (PM) fibers. Although we typically lose around 30% of the optical power, the gain is in terms of flexibility in alignment and mechanical stability.

The single-beam ODT light at a wavelength of 1557 nm is derived from a 10 W Nufern fiber amplifier seeded with a narrowband fiber laser (NP

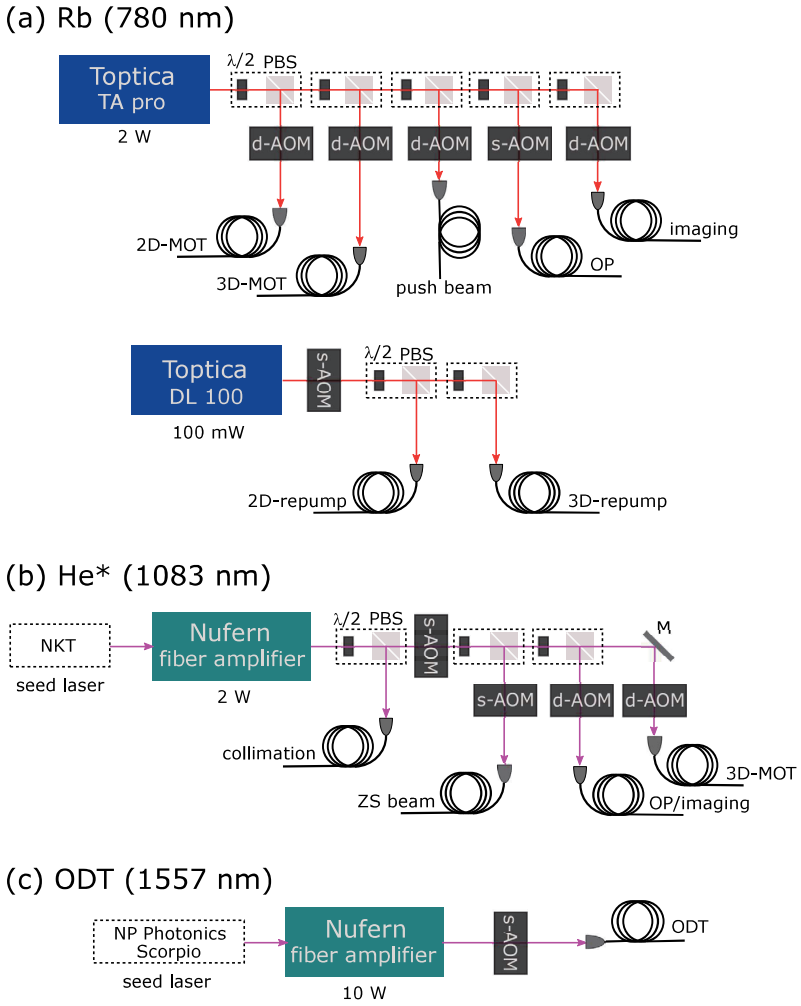

Figure 2.3: Overview of the laser system used for (a) Rb and (b) He*. The light is distributed over the MOT, optical pumping (OP), pushing, collimation and absorption imaging beams using a half waveplate ($\lambda/2$) and polarizing beam splitter (PBS) combination. (c) Laser system for the optical dipole trap (ODT). ZS: Zeeman slower, s-AOM: single-pass configuration and d-AOM: double-pass configuration.

509242-L-bw-Flores
Processed on: 3-4-2017

Photonics Scorpio). The output of the amplifier passes through an AOM to allow for fast switching and control of the power when performing evaporative cooling in the HT or ODT. In here, it is not necessary to tune the AOM frequency, so we use a single-pass configuration to keep most of the optical power (see Fig. 2.3(c)). Typically, we have around 60 to 70% AOM coupling efficiency. Finally, the ODT light is delivered to the setup using a PM fiber with a typical coupling efficiency of also around 75%. After passing through the AOM, fiber and collimating and focusing lenses, the total available power for optical trapping is around 4 W.

2.3 Two-species magneto-optical trap

Our 3D-MOT consists of three retro-reflected beams and a quadrupole magnetic field derived from a pair of coils in anti-Helmholtz configuration. The laser beam for the 3D-MOT of each species passes through an AOM in a double-pass configuration. The typical total 3D-MOT power used is between 20 to 50 mW for both species. For Rb, the beam is detuned by around -15 MHz with respect to the $f = 2$ to $f' = 3$ transition. For He*, a large detuning of around -33 MHz is used in order to minimize light-assisted intraspecies Penning ionization [79, 80, 104]. To make the alignment easier and save optical access around the main chamber, we couple the 3D-MOT beams for the two species in the same fiber using dichroic mirrors (see Fig. 2.4). With this, the 3D-MOT of both species are automatically overlapped. Lastly, a 920 nm quarter waveplate is used to create the necessary circular polarization. The coils are water-cooled and can provide a magnetic

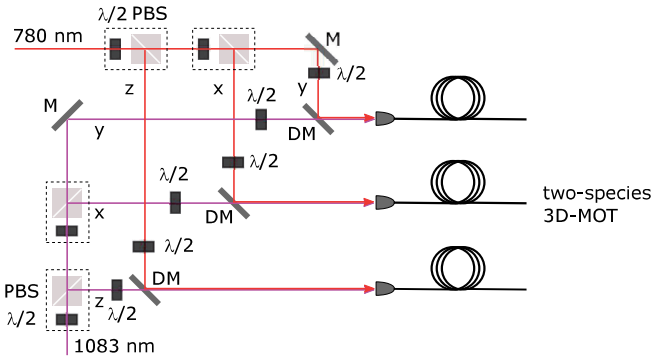

Figure 2.4: Rb and He* 3D-MOT beams coupled in the same fibers using dichroic mirrors (DM). The 3D-MOT beam powers (for the three directions) are distributed using half waveplate ($\lambda/2$) and polarizing beam splitter (PBS) combinations. Also shown are the separate $\lambda/2$ plates for aligning the input polarization of the light with respect to the input polarization of the PM fiber.

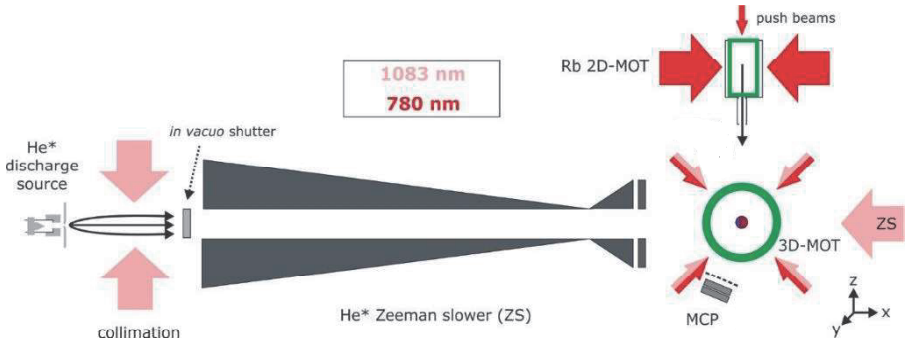

Figure 2.5: A schematic overview of the two-species MOT. The vertical direction is along the z-axis. Note that the pair of laser beams along the y-axis of the collimation section, the 2D-MOT, the 3D-MOT, and optical pumping and/or absorption imaging beams are not shown. (ZS: Zeeman slower; MCP: microchannel plate).

field gradient of 0.6 (G/cm)/A along the weak axis. In the MOT stage, we typically apply between 10 to 20 A to the coils.

Fig. 2.5 shows a schematic diagram of the experimental setup illustrating the preparation and loading of the atomic species into the 3D-MOT. Rb atoms, that are initially laser cooled in the 2D-MOT, are transferred to the 3D-MOT using two distinct pushing beams [105]. One pushing beam is red-detuned to redirect the atoms that are initially going in the opposite direction while the other pushing beam is blue-detuned to guide the atoms toward the 3D-MOT. He* atoms are loaded from a zero-crossing Zeeman slower where the atoms are initially slowed down. We use a dc-discharge to access the metastable state (typical metastable fraction of 10^{-4} [106]). The source is cooled with liquid nitrogen and the beam of metastable atoms is collimated after exiting through a skimmer before entering the 2.5-m Zeeman slower. We first load the Rb atoms followed by He* loading. To minimize the continuous flux of ground state He towards the 3D-MOT, two in-vacuo shutters are introduced between the source and the Zeeman slower (before and after a differential pump tube), which are only opened during the He* loading. We typically load at least 10^9 Rb and 10^8 He* atoms. After loading the two atomic species, we compress the sample by increasing the 3D-MOT gradient (cMOT stage). Afterward, the gradient is switched off to start the optical molasses (OM) stage for further cooling. After the OM stage, we apply simultaneous optical pumping (OP) on both species in order to prepare the sample in the desired low-field seeking doubly spin-stretched spin-state ($|m_s = +1\rangle_{^4\mathrm{He}^*} + |f = 2, m_f = +2\rangle_{^{87}\mathrm{Rb}}$) before transferring to the QMT for evaporative cooling. The two OP beams are also coupled in the same fiber using a dichroic mirror (see Fig. 2.13(a)).

2.4 Evaporative cooling in the quadrupole magnetic trap

For magnetic trapping, we have used the same coils as for the 3D-MOT to create the quadrupole magnetic trap. In the QMT, the current applied to the coils is typically 200 A, corresponding to a magnetic field gradient of 120 G/cm. To perform forced evaporative cooling on Rb, we drive MW transitions between the trappable and non-trappable hyperfine states. The choice of using MW instead of RF is to allow for simultaneous evaporative cooling of both species in the QMT, as He* atoms are not affected by the MW radiation. For He*, we use RF to drive transitions between the Zeeman states. A feature that is generally true for any He*+alkali mixture is that the Zeeman splitting in He* is larger than in the alkali atoms. In the case of He* and Rb, these are $2\mu_B B$ and $\mu_B B/2$ respectively. For Rb in the $|f = 2, m_f = +2\rangle$ state, the trap depth given by the RF is a factor of two larger than that for He*, and therefore RF can be selectively used for He*. The condition that the MW-truncated trap depth of Rb is lower than the RF-truncated one is given by: $\nu_{MW} - \nu_{HFS} < 3\nu_{RF}$, where ν_{RF} and ν_{MW} are the RF and MW frequencies respectively, and ν_{HFS} is the hyperfine splitting of Rb. For the two species to have equal trap depths in which the Rb is governed by MW and He* by RF, the condition is $\nu_{MW} - \nu_{HFS} = 3\nu_{RF}/2$. The duration and frequencies used in the evaporative cooling are mentioned in the next chapters for each specific experiment that is performed. In here, we only describe the technical details of the RF and MW sources used for the evaporative cooling of each species.

2.4.1 Radio-frequency source

The RF radiation used for the evaporative cooling of He* is derived from the output of an 80 MHz tunable signal generator (Agilent 33250A) which is sent to a frequency doubler (Mini-Circuit MK-3) (see Fig. 2.6(a)). The principal signal is suppressed by at least 25 dBm with respect to the frequency doubled signal and is negligible. The 4th and higher harmonic signals are suppressed by only around 10 to 20 dBm with respect to the frequency doubled signal. However, these harmonic signals in principle will not be in resonance with the remaining He* atoms in the QMT during the evaporation process. Afterward, the signal is pre-amplified (Mini-Circuits ZFL-500LN+) to reach the desired input threshold of the next amplification stage. We observe that the overall output power of the RF system changes noticeably within the frequency range used for the evaporative cooling (see Fig. 2.6(b), red squares). To compensate for this non-uniformity in the power, we initially fix the output power at a relatively high value and use a variable attenuator (Mini-Circuits ZAS-3+) to regulate the power throughout the frequency range for the evaporative cooling (see Fig. 2.6(b), blue circles). Finally, the

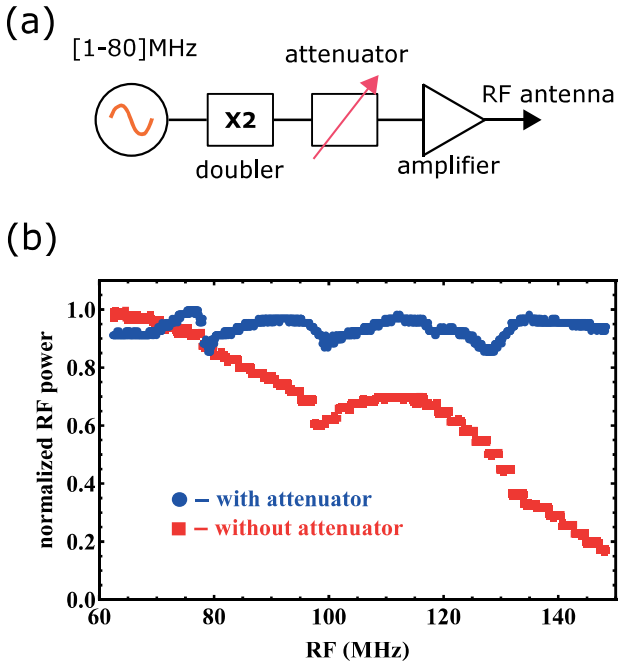

Figure 2.6: (a) Schematic diagram of the RF radiation source used for the evaporative cooling of He* showing the frequency doubling scheme in combination with the variable attenuator to regulate the RF output power. (b) Comparison of the RF output power with (blue circles) and without (red squares) using the variable attenuator (see text).

signal is sent to a 30 W linear amplifier (Mini-Circuits LZY-22+) from which the output is used to drive the RF coil that is positioned inside the main vacuum chamber. During the evaporative cooling in the QMT, we typically send around 5 W to the RF coil with a frequency range up to 160 MHz.

2.4.2 Microwave source

The MW source to be used for the evaporative cooling of Rb should be able to cover the hyperfine splitting of 6.835 GHz. We use a 6.8 GHz phase-locked oscillator (Amplus PLO) mixed (Mini-Circuits ZMX-8GLH) with the output signal of an 80 MHz tunable signal generator (Agilent 33250A), which is also frequency doubled (Mini-Circuits MK-3) (see Fig. 2.7(a)). Due to the presence of several harmonic signals resulting from both frequency doubling and mixing, we also introduce a series of high pass (Mini-Circuits VHF-7150+) and low pass (Mini-Circuits VLF-6000+) filters to allow only signals within the desired frequency range. The frequency response of this filter combination is shown in Fig. 2.7(b). Here we show the insertion loss as

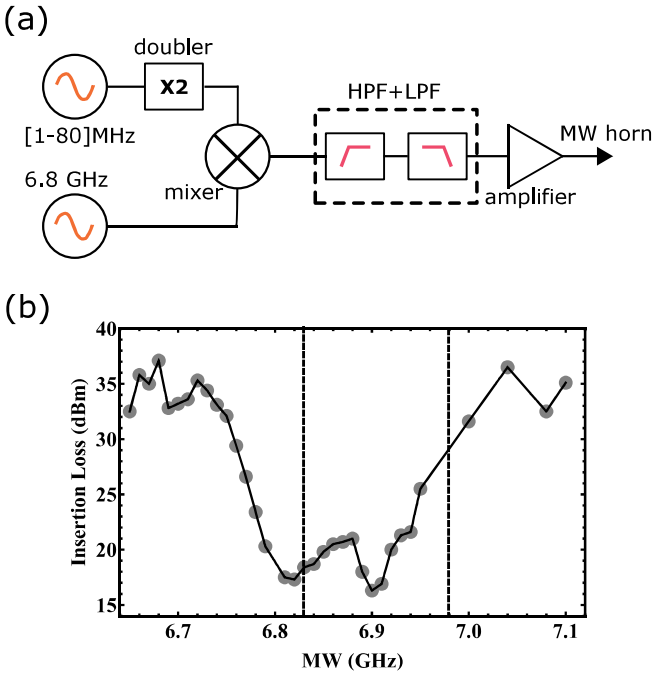

Figure 2.7: (a) Schematic diagram of the MW radiation source used for the evaporative cooling of Rb showing the frequency doubling of the function generator and frequency mixing with the 6.8 GHz phase-locked oscillator signal. Also shown are the added high pass (HPF) and low pass filter (LPF) forming a band pass filter to allow only the frequency range useful for the evaporative cooling. (b) Frequency response of the MW design showing the attenuation of the signals outside the frequencies used for the evaporative cooling. The two vertical dashed-lines indicate the range used for evaporative cooling.

a function of frequency, attenuating most of the signal frequencies outside the range that is useful for the evaporative cooling. We also introduce a series of pre-amplification stages (Mini-Circuits ZJL-7G+). Finally, the signal is sent to a 8 W amplifier (Kuhne KU PA 7000A) from which the output is used to drive the MW horn (LABEM), which is placed outside the vacuum setup and is directed to the center of the main vacuum chamber through a window. However, the amplifier is saturated because it is not possible to completely remove the additional harmonic signals, especially those frequencies that are close to the desired frequency signal. We estimate a total of only around 1 to 2 W sent to the MW horn that corresponds to the actual desired frequency. Nonetheless, these spurious signals that are not significantly suppressed, are either below the hyperfine splitting or higher than the desired frequency signal for the evaporative cooling, and these

signals will also not affect the remaining Rb atoms during the evaporation process. The actual consequence is limited MW power available for the experiment.

2.5 Hybrid trap and optical dipole trap

Our optical dipole trap (ODT) laser beam is delivered to the setup using a polarization maintaining single-mode fiber (OZ optics). After a fiber outcoupler and a telescope, the light is focused into the setup by an achromat doublet 2-inch lens with $f = 400$ mm (Thorlabs, AC508-400-C) at an angle of 11° with respect to the axial direction of the QMT coils and 22° with respect to the imaging beam (see Fig. 2.8(a)). The lens is on a translation stage to axially align the focus of the ODT beam with the center of the QMT. The kinematic mount of the last mirror (before the lens) is piezo-controlled to allow for precise alignment of the ODT in the radial direction. The Rayleigh length is 3 mm, which is much smaller than the 4 cm distance between the glass windows of the vacuum chamber and the waist w_0 is 39.8 ± 0.3 μm, obtained by measuring the radial trap frequency in a pure ODT [107].

Towards the transfer to a pure ODT, we have used the hybrid trap (HT) as an intermediate stage to facilitate the initial transfer from the QMT. In principle, further evaporative cooling can also be performed in the HT. The HT is basically a single-beam ODT combined with a weak QMT, in which the ODT is aligned slightly away from the QMT center in such a way that the atoms remain at a finite magnetic field and thus avoid Majorana spin-flip loss (see Fig. 2.8(b)). The weak QMT provides an additional confinement along the axial direction giving a higher peak density as compared to the pure single-beam ODT, and is chosen to be slightly below the levitation gradient $B'_{\mathrm{lev}} \equiv mg/\mu$ (where m is the mass, μ is the magnetic moment of the atom and g is the gravitational acceleration), to ensure that atoms are trapped in the HT and not by the QMT.

We first implement the HT to Rb and scan the position of the ODT with respect to QMT using the piezo-controlled mirror. We make use of the fact that if the ODT is located at the QMT center, the atoms will undergo Majorana spin-flips and leave the trap. A typical measurement is shown in Fig. 2.8(c). We first do the horizontal scan (see inset) and observe a symmetric loss feature with a $1/e^2$ half width of 30 μm. At the horizontal piezo voltage position where the signal is minimum, we scan in the vertical direction, again showing a clear minimum with a $1/e^2$ half width of 40 μm. Here the data clearly shows more atoms when the ODT is placed below the QMT center, and that the transfer efficiency is constant over a broad range of offsets from the QMT center. Still, to maximize the axial trap frequency and peak density one preferably chooses the offset as small as possible within

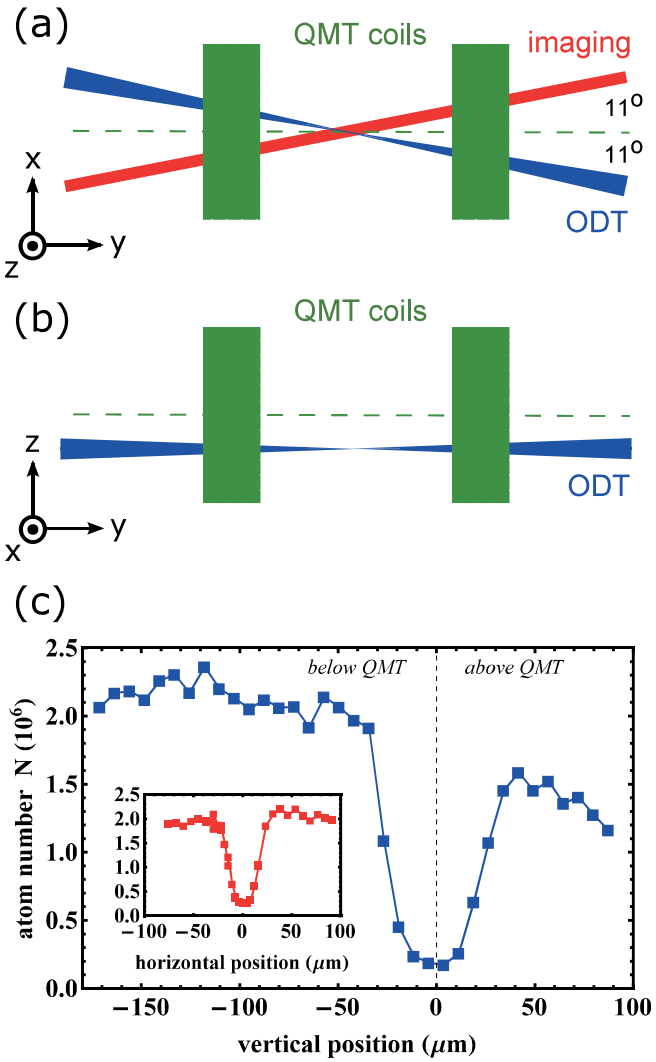

Figure 2.8: Schematic diagram showing (a) the orientation of the ODT beam with respect to the QMT coils and imaging beam, and (b) the hybrid trap configuration (ODT+weak QMT) showing the offset in the $y-z$ plane. (c) Number of atoms loaded in the hybrid trap as function of position of the ODT with respect to the QMT center in the vertical direction (main graph) and horizontal direction (inset).

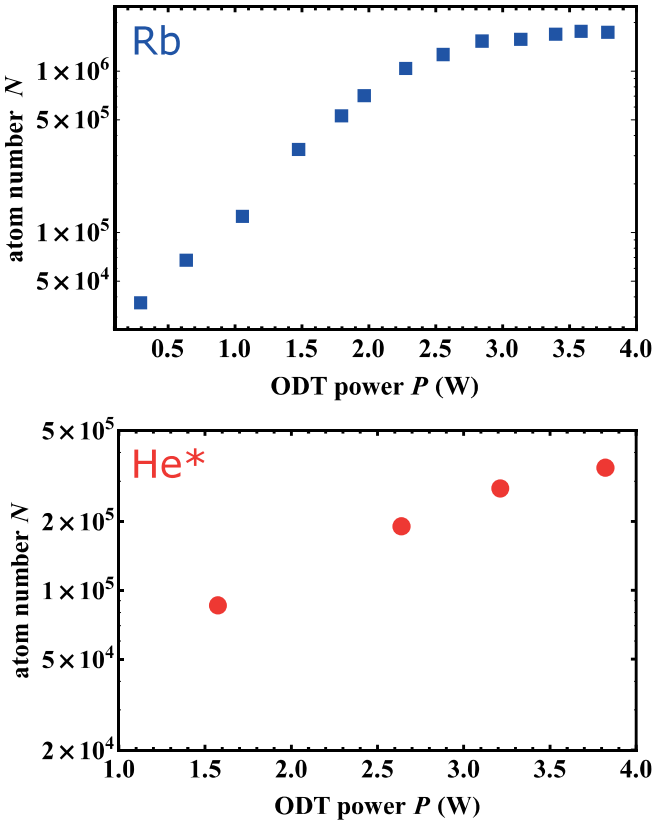

Figure 2.9: Number of atoms loaded in the HT/ODT as function of ODT power, comparing Rb (top) and He* (bottom). For the case of Rb, a clear sign of saturation in the loading is already noticeable at an ODT power of around 2.5 W. In contrast, there is no clear sign of saturation in the loading for He* even at an ODT power close to 4 W. The data shown are typical measurements performed in a single-species preparation.

this broad range [107]. In Fig. 2.9, the number of atoms loaded in the HT as a function of the ODT power is shown, comparing Rb and He*. In the case of Rb, a clear sign of saturation in the loading is visible around 2.5 W. In contrast, the He* data suggest that our available ODT power is limited. This observation is not surprising because the temperature at which we load He* into the ODT is much higher as compared to Rb, limiting the transfer efficiency. This is simply constrained by the Majorana heating which is worse for lighter atomic species [9, 95]. Details regarding the application of the HT to He* is presented in Chapter 3 and a comparison with Rb in the mixture experiment is discussed in Chapter 4. Using the HT scheme, we manage to achieve Bose-Einstein condensation (BEC) of Rb [107] and He*

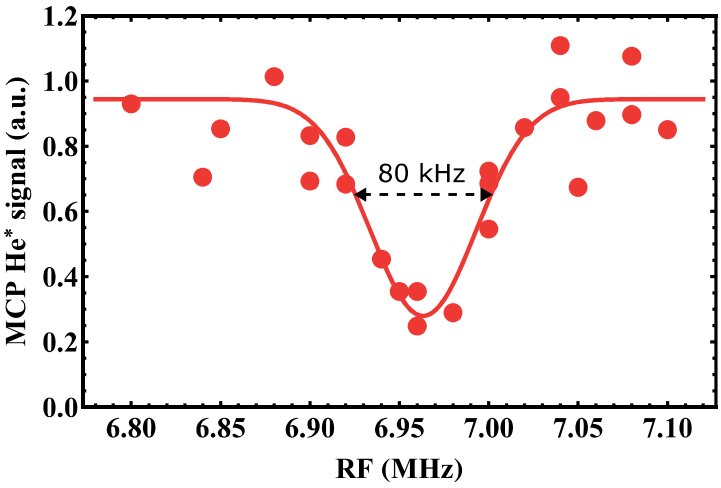

Figure 2.10: RF spectroscopy of He* in the ODT in order to measure and calibrate the small bias magnetic field. He* signal is measured using a microchannel plate (MCP; see section 2.6.2 for detailed discussion). The 80 kHz width is due to the combined effect of temperature (around 5 μK sample) and magnetic field noise (in the order of 10 mG). Solid line is a Gaussian fit.

[108] in our single-species experiments.

An important aspect in our experiment is to investigate different spin-state mixtures. In the HT, due to the presence of the (weak) QMT, the possible spin-state combinations are limited to low field-seeking states, similar as in the QMT. In contrast, a pure (far off-resonant) optical dipole trap allows trapping of all spin-state combinations with a confinement independent of the chosen spin-state. In our experiment with the mixture, we only use the HT to facilitate the initial transfer from the QMT to the pure ODT. For instance, we have used this stage to smoothly introduce and keep a small quantization magnetic field for the atoms. Once in the pure ODT, this small magnetic field is essential to keep the spin-orientation of the atoms. To calibrate and measure this field, we perform RF spectroscopy on the sample in the pure ODT. Fig. 2.10 shows a typical example of such measurement. Here, we use He* atoms as probe and rely on the idea that at resonance, atoms are transferred to the other Zeeman states resulting in a spin-mixture and thus fast Penning ionization loss [109] (additionally, atoms in the $|m_s = -1\rangle$ and $|m_s = 0\rangle$ are not detected on an MCP, see Section 2.6.2). A magnetic field of 2.5 G is obtained from the resonance frequency via the equation $B = h\nu_{\mathrm{RF}}/2\mu_B$, where h is the Planck's constant, ν_{RF} is the RF frequency and μ_B is the Bohr magneton.

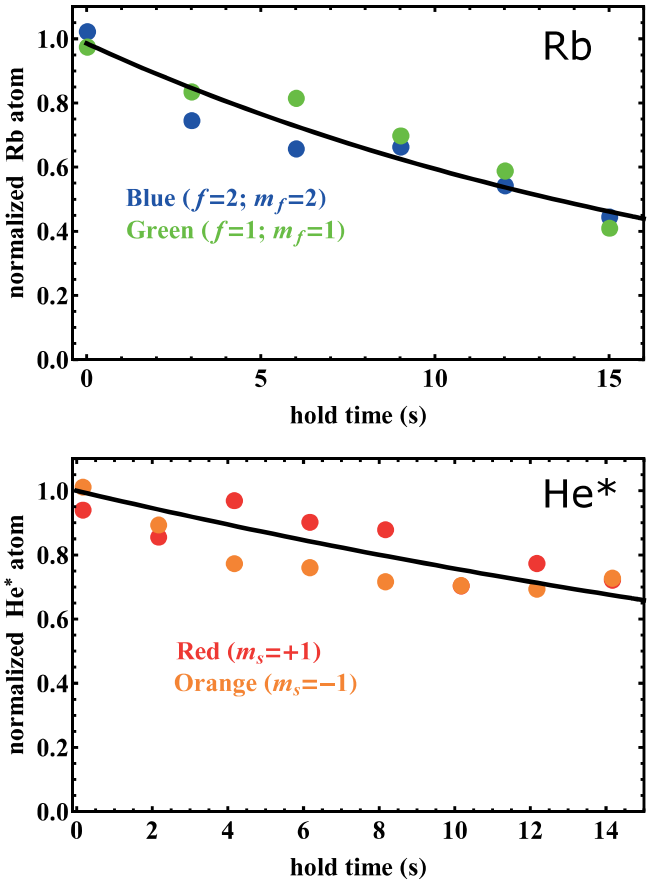

Figure 2.11: Lifetimes of the two different hyperfine states of Rb (top) and of the two different Zeeman states of He* (bottom). Solid lines are guide for the eye.

In Fig. 2.11, we show typical single-species lifetimes of the different spin-states used in the experiment, namely the two hyperfine states of Rb ($|f = 2, m_f = +2\rangle$ and $|f = 1, m_f = +1\rangle$) and two Zeeman states of He* ($|m_s = +1\rangle$ and $|m_s = -1\rangle$). These measurements are performed in the ODT at a temperature of ∼15 μK. We find no observable difference between the two Rb hyperfine states and measure a lifetime of ∼20 s. Similarly, for He*, there is also no significant difference between the lifetimes of the two Zeeman states, which is ∼35 s. We have investigated the contribution of the off-resonant scattering at the typical ODT power of up to 4 W and found no direct correlation with the measured lifetimes, which suggest that the lifetimes are mainly governed by background collisions and scattering from

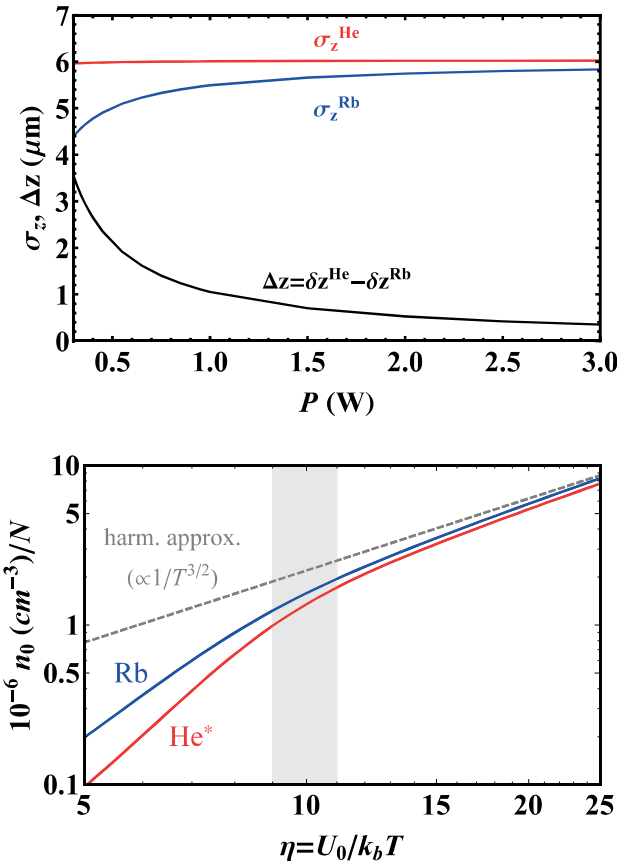

Figure 2.12: (Top) Calculated differential gravitational sag Δz (black line) between the clouds of the two species in the ODT as a function of ODT power. This effect is mainly due to huge difference in the masses of Rb and He*. The differential gravitational sag should be compared with the width (σ_z) of He* (red line) and Rb (blue line) clouds. (Bottom) Comparison of the peak density by solving the exact potential numerically and using the harmonic approximation, showing a deviation at typical truncation parameter η=10. Calculation is done for an ODT power of 4 W and waist of 40 μm.

not completely shielded resonant light.

An important issue which leads to spatial separation of the two clouds is the differential gravitational sag $\Delta z = \delta z^{He} - \delta z^{Rb}$, where $\delta z = -g/\omega_z^2$ is the gravitational sag, $\omega_z = \sqrt{4U_0/mw_0^2}$ is the vertical trap frequency and U_0 is the trap depth, which scales with ODT power. This is inherent to heteronuclear mixtures due to the difference in the masses and more pronounced with mixtures involving a heavy and a light atomic species like

our He*+Rb mixture. Shown in Fig. 2.12 (top panel) is the differential gravitational sag Δz as function of ODT powers (for the case of our single-beam ODT), indicating a more pronounced effect towards lower ODT power (lower trap depths). This is very crucial when realizing colder samples, in particular a dual BEC. In our mixture experiments, we stayed at the highest ODT power available (around 4 W) where the effect of differential gravitational sag is negligible.

In the ODT, the two atomic species experience different trap depths due to the difference in polarizability, which at $\lambda = 1557$ nm is a factor of 1.4 higher for He* compared to Rb [110, 111]. The main consequence is that the two species have different temperatures because interspecies thermalization is absent for the experimentally relevant time scales due to the small interspecies elastic cross-section [88]. In addition, for the analysis involving peak densities and overlap of the two species, we also consider and solve the exact trapping potential numerically. This is necessary because in our single-beam ODT, at the typical truncation parameter of around $\eta = U_0/k_BT = 10$ (where k_B is the Boltzman constant and T is the temperature), there is a significant deviation from the typically used analytic expressions derived from the harmonic approximation, see Fig. 2.12 (bottom panel).

2.6 Detection scheme

In our experiment, two important parameters that we need to determine are the atom number and temperature of the sample. Initially, during the optimization and characterization of our system, we have used several schemes such as fluorescence detection (using photodiode and camera) [112], absorption imaging for both Rb and He*, and time-of-flight (TOF) measurement from a microchannel plate (MCP), applicable only to He*. However, for most of the relevant data, we base the analysis from the absorption imaging and MCP TOF detection as these turned out to be the most accurate. In this section, we only describe these two schemes.

2.6.1 Absorption imaging

Standard absorption imaging is used to measure the atom number and temperature for both species. To save optical access around our main chamber, we also couple the imaging lights for the two species in the same fiber using a dichroic mirror together with the OP light for Rb (see Fig. 2.13(a)). For He*, the same OP light can be applied for imaging because the detuning and power can be adjusted accordingly via an AOM. For both species imaging and to avoid heating or pushing the atoms, we send low intensity beams (much lower than the saturation intensities) with 100 to 200 μW optical power and $\sim$1 inch diameter. To create the proper circular polarization, we implement a 920 nm zero-order quarter waveplate. We send these imaging

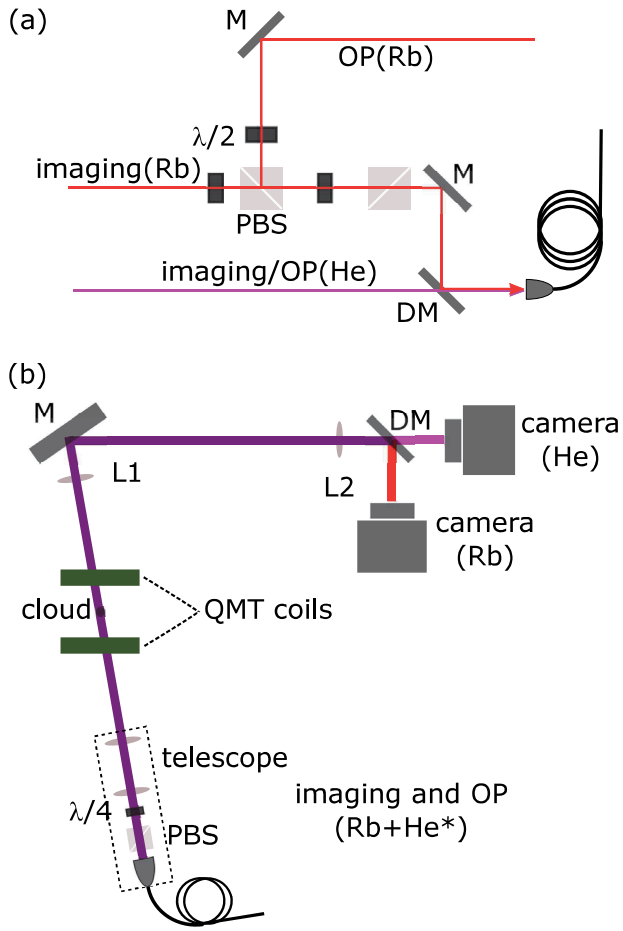

Figure 2.13: (a) OP and imaging beams for He* and Rb are coupled in the same fiber using a dichroic mirror (DM). For OP and imaging of He* , the same beam is used while the detuning and power are adjusted accordingly via an AOM. A mechanical shutter (not shown in the figure) is added before the fiber to minimize stray light. (b) Schematic diagram of the dual imaging. To image the cloud, we use a 2:1 (L1 = 30 cm and L2 = 15 cm) telescope to accommodate the size of the cloud on the camera chip. Enclosed in the dashed rectangle is the typical configuration used for delivering the laser beams into the main chamber. The fiber outcoupler, polarizing beam splitter (PBS), quarter waveplate ($\lambda/4$) and collimating lenses are mounted on a single stage.

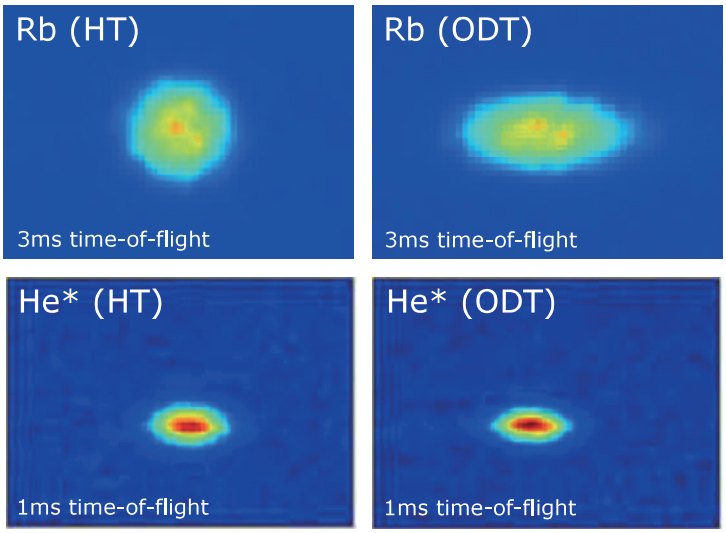

Figure 2.14: Absorption images of Rb and He* atoms released from the HT and/or ODT, comparing the difference in the aspect ratio. The difference is particularly noticeable for Rb due to the stronger additional axial confinement provided by the QMT as compared to He*. Note that the axial direction (see also Fig. 2.8(a)) is only viewed from the 22° projection of the imaging beam with respect to the ODT beam. The size of each rectangular image is approximately 1.5×2.0 mm.

beams at an angle of approximately 11° with respect to the axial direction of the QMT coils (see also Fig. 2.8(a)). We use a magnification of 0.5 to accommodate the size of the cloud onto the camera chip particularly during expansion measurements. We also use a dichroic mirror to image the two clouds on two different cameras. For Rb, we use a CCD camera (QImaging Exi-blue) with 6.45 μm pixel size. For He, we use an InGaAs camera (Xenics Xeva 320) with a 30 μm pixel size. In Fig. 2.14, we show and compare typical absorption images of Rb and He* that are released from the HT and ODT. Note that because of the orientation of the imaging beam with respect to the ODT beam, we can only see the projection of the image along the axial direction from the 22° angle (see Fig. 2.8(a)). For Rb in the HT, the cloud is almost circular because of the additional confinement in the axial direction provided by the QMT in contrast to the elliptical shape in the pure ODT. For He*, there is no significant difference between the HT and ODT clouds. This is because of the much weaker additional confinement in the axial direction due to the much lower levitation gradient. In principle, absorption imaging of the two species can be done simultaneously because the light for Rb is far from any transition in He* and vice-versa. Simultaneous imaging of the two species is essential especially during the

optimization process. For instance, we can easily track the positions of the two clouds when aligning the MOT beams to optimize the OM stage and the subsequent transfer of the mixture to the QMT.

2.6.2 Microchannel plate detection

Additionally for He*, because of the high internal energy (19.8 eV), we also use a microchannel plate (MCP) detection that is positioned below the trap center (at angle 22° with respect to the direction of gravity, see Fig. 2.5) to measure time-of-flight (TOF) distributions. In Fig. 2.15(a), we compare typical TOF distributions for samples released from the 3D-MOT, QMT and ODT. For the higher temperature samples, where the average kinetic energy of the atoms is much higher than the potential energy defined by the distance to the MCP, the TOF clearly exhibits the typical asymmetric Maxwell-Boltzman distribution, as seen for the 3D-MOT. For lower temperature samples (average kinetic energy of the atoms is much smaller than the potential energy), the TOF becomes symmetric and can be approximated with a Gaussian distribution, as seen for the ODT. With the geometry of our MCP detection, the temperature that separates these two regimes (kinetic energy is equal to the potential energy) is on the order of $mgh/k_b \approx 0.5$ mK, where m is the mass of He, $h = l\cos 22°$ is the vertical distance from the center of the trap to the MCP detector and $l = 10.6$ cm. Note that the QMT and ODT TOFs are rescaled for clarity.

It must be noted that towards lower temperature, the sample will not hit the MCP because of the 22° angular displacement from the vertical axis. Therefore a magnetic gradient pulse (from a single deflection coil, with approximately 665 windings and 15 cm inner diameter) is applied to direct the atoms onto the MCP detector [108] for sufficiently low temperature samples, such as a sample that is released from the ODT. In Fig. 2.15(b), we compare MCP signals with and without introducing the deflection gradient. Note that the signal without deflection is also rescaled for clarity. We keep the pulse duration as short as possible (around 10 ms) to minimize the disturbance introduced on the cloud during the time-of-flight. We observe an optimum in the MCP signal at around 6.5 A applied to the deflection coil, consistent with what we expect from a simple classical mechanics calculation based on the distance of travel and the force generated from the magnetic field gradient. TOF measurements of He* can also be done simultaneously with the Rb imaging. After the clouds are released from the ODT, we first capture the images (ballistic expansion typically between 1 ms to 5 ms), after which the magnetic gradient pulse is applied.

Our experiments involve samples of different spin-states. Distinguishing between these different spin-states from the detection scheme is essential. The most common technique employed is Stern-Gerlach imaging, where a magnetic field gradient is applied during expansion to separate atoms of

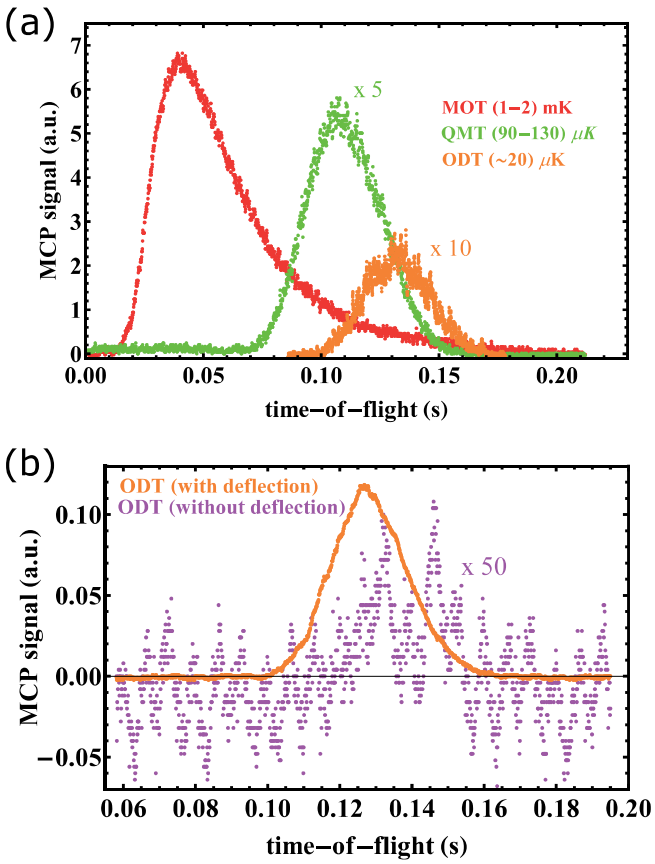

Figure 2.15: (a) Typical TOF distributions as measured by the MCP comparing MOT, QMT, and ODT. Notice the change in the shape from the asymmetric Maxwell-Boltzman distribution (MOT, hotter sample) towards the more symmetric Gaussian shape (ODT, colder sample). For clarity, the QMT and ODT TOF signals are rescaled by a factor of 5 and 10 respectively with respect to the MOT TOF signal. (b) Comparison of the TOF signal for samples released from the ODT (in this example below 10 μK) with and without the deflection gradient. The magnetic gradient pulse duration is around 10 ms. For clarity, the ODT TOF signal without deflection is also rescaled by a factor of 50 with respect to the signal with deflection. The difference in the position of the center of the TOF distributions is due to the small acceleration introduced by the deflection gradient.

different spin-state (due to their distinct magnetic moment). Unfortunately, our deflection coil can only provide a magnetic field gradient (providing a force) along the horizontal direction that coincides with the direction where the absorption images are elongated (see Fig. 2.14), making it difficult to resolve the small shift in the positions between atoms of different spin-state. In addition, it was not feasible to install a different coil around the main chamber that can provide sufficient magnetic field gradient for the purpose due to the limited space. Nonetheless, for Rb, we can use the repumping beam during imaging to distinguish atoms between the two hyperfine states $|f = 2, m_f = +2\rangle$ and $|f = 1, m_f = +1\rangle$. We can only image the atoms in hyperfine state $|f = 1, m_f = +1\rangle$ in the presence of the repumping light. In the case of He^* using the MCP TOF detection, the orientation of the deflection coil and the MCP position will already suffice for the purpose. Note that our deflection coil is designed to give a force that pushes the atoms towards the MCP. Atoms of opposite spins are thus deflected in the opposite direction and not detected. To detect He^* atoms in the $|m_s = -1\rangle$ state, we apply an RF sweep that transfers back the atoms to the $|m_s = +1\rangle$ state (this is discussed in the next section).

2.7 Preparation of different spin-states

For preparation of the ultracold sample, we use the stable mixture in the doubly spin-stretched spin-state $|m_s = +1\rangle_{^4\mathrm{He}^*} + |f = 2, m_f = +2\rangle_{^{87}\mathrm{Rb}}$. However, the study of Feshbach resonances or spin-dependent Penning ionization requires different spin-state combinations. In this section, the preparation of the different spin-state samples using RF and MW frequency sweeps is described.

2.7.1 Rapid adiabatic passage

Consider the case of a two-level atom in a classical oscillating field with frequency ω. In the dressed-states picture (see Fig. 2.16), this constitutes an avoided crossing around a resonance frequency ω_0 where $\Delta = \omega - \omega_0$ is the detuning. The width of the crossing is proportional to the Rabi frequency Ω (i.e. strength of the field). By applying a linear sweep such that $\Delta(t) = \alpha t$, the probability for a diabatic transition is given by the Landau-Zener formula [113, 114], $P = \exp\left[-2\pi\Omega^2/|\alpha|\right]$, where α corresponds to the constant velocity of the sweep. For a sufficiently slow sweep, the atoms undergo a rapid adiabatic passage between the bare states. Given that initially the atoms are in state a, the remaining population P_a after the rapid adiabatic passage, as a function of sweep time t_sweep, is given by,

$$P_\mathrm{a} = P_0 \exp\left[-A t_\mathrm{sweep}\right], \tag{2.1}$$

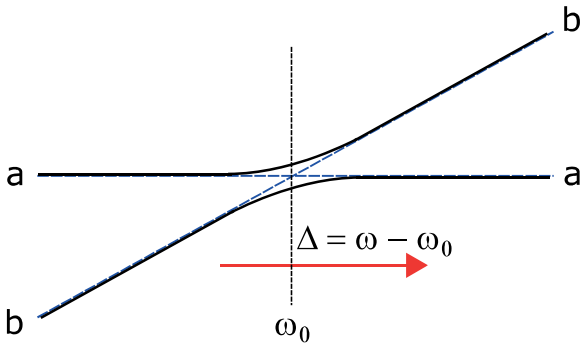

Figure 2.16: Dressed-states picture of a two-level atom in a classical oscillating field with frequency ω showing the avoided crossing around the resonance frequency ω_0. a and b are the bare states, Δ is the detuning, and the width of the crossing is proportional to the Rabi frequency Ω.

where P_0 is the initial atom number, and A is proportional to the square of the Rabi frequency $\Omega^2 = (\mu_B g_J M B_0/\hbar)^2$; μ_B: Bohr magneton, g_J: electron g factor, $M = \langle f, m_f | J_z | f+1, m_f \rangle$: general form of the quantum-mechanical matrix element and J_z is the electron spin, B_0: amplitude of the RF or MW field [115]. Population in state b is then given by $P_0(1 - P_a)$.

2.7.2 RF and MW sweeps

Experimentally, there are two ways to perform a transfer sweep on the atoms. The most commonly used is via a magnetic field sweep in the presence of a RF/MW field at a fixed frequency. The second method is by applying a constant magnetic field while sweeping the frequency of the RF/MW field around the resonance. In our case, the frequency sweeps offer better control and stability as compared to magnetic field sweep. We have used the same RF and MW sources described in Section 2.4 for the sweeps, however without using the frequency doubling scheme and thus free from harmonic signals (for the case of RF). However, in the MW source, the harmonic signals due to the frequency mixing are still present. We realize this scheme by using additional signal generators (only used for the sweep) together with a digitally controlled switch (Mini-Circuits ZASWA-2-50DR+) providing two pathways, one path for transfer and another for evaporative cooling as described in Section 2.4.

For He^*, we apply RF with typical sweep range of 0.5 to 1 MHz (centered around 6.95 MHz) in less than 50 ms at a magnetic field of 2.5 G to transfer the atoms between the Zeeman states. With an RF power of around 1 W, we transfer all of the atoms from the $|m_s = +1\rangle$ to the $|m_s = -1\rangle$ state (see Fig. 2.17(a)). Also shown is a comparison between three different RF powers, which is in good agreement with what is expected from the

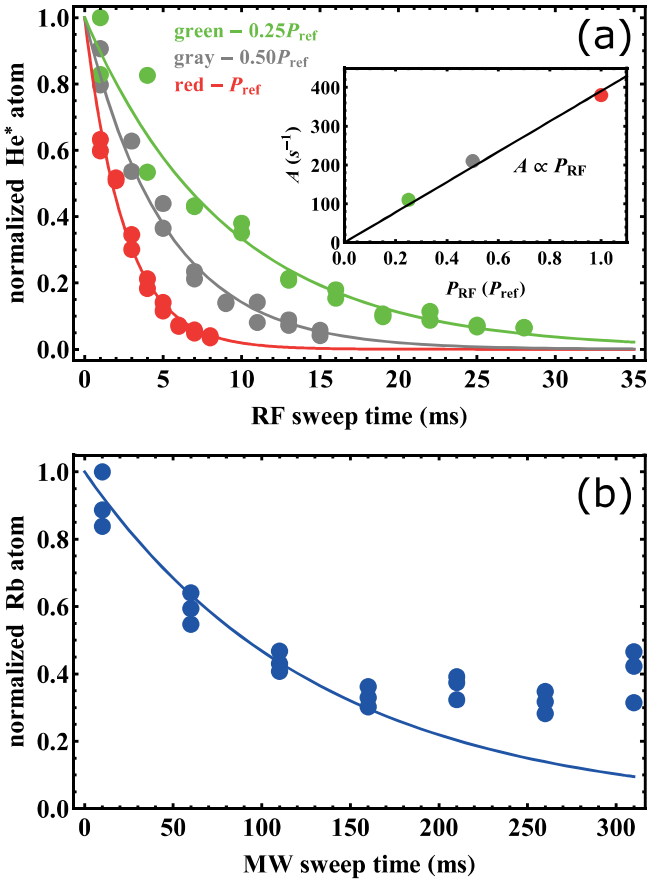

Figure 2.17: (a) ^{4}He* atoms in the $|m_s = +1\rangle$ state that remain in the ODT after adiabatic state transfer to $|m_s = -1\rangle$ via an RF frequency sweep as a function of sweep time for three different RF power. ^{4}He* atoms in the $|m_s = -1\rangle$ state are not detected because the deflection coil pushes these atoms away from the MCP detector. (b) ^{87}Rb atoms in the $|f = 2, m_f = +2\rangle$ state that remain in the ODT after adiabatic state transfer to $|f = 1, m_f = +1\rangle$ as a function of sweep time of the MW frequency sweep. The imaging is performed without repumping light, which means that ^{87}Rb atoms in the $|f = 1, m_f = +1\rangle$ state are not detected. Solid lines are fit from Eq. 2.1 from which the Rabi frequencies are obtained (see text).

proportionality relation: $A \propto \Omega^2 \propto P_{\mathrm{RF}}$ (see inset of Fig. 2.17(a)). For a three-level system, $A = \pi\Omega^2/|\delta\omega_{\mathrm{RF}}|$ where $\delta\omega_{\mathrm{RF}}$ is the RF frequency sweep [116]. Rabi frequencies are obtained by fitting Eq. 2.1 to the data, $\Omega/2\pi = 3.0 \pm 0.3$ kHz; 2.3 ± 0.2 kHz; 1.7 ± 0.2 kHz for the three powers respectively, which corresponds to an RF field amplitude B_0 of a few milliGauss. We confirm the transfer by applying a second sweep that transfers back and recover the atoms to the $|m_s = +1\rangle$.

For Rb, we apply MW with typical sweep range of 0.2 to 1 MHz (centered around 5 MHz above the hyperfine splitting) in a few tens to hundreds of milliseconds at a magnetic field of 2.5 G to transfer the atoms from the hyperfine state $|f = 2, m_f = +2\rangle$ to $|f = 1, m_f = +1\rangle$. However, due to the limited MW power, we only manage to transfer around 50% of the atoms to the $|f = 2, m_f = +1\rangle$ (see Fig. 2.17(b)). Nonetheless, to keep only a single spin-state of Rb, we send resonant light to clean the remaining atoms in the $|f = 2, m_f = +2\rangle$. For the case of Rb transfer between the hyperfine states, the manifold can be considered as an effective two-level system, and $A = 2\pi\Omega^2/|\delta\omega_{\mathrm{MW}}|$, where $\delta\omega_{\mathrm{MW}}$ is the MW frequency sweep. Fitting only the first part of the data in Fig. 2.17(b), we extract typical Rabi frequencies $\Omega/2\pi$ between 200 to 400 Hz, corresponding to a MW field amplitude of only around a milliGauss.

Chapter 3

Simple method for producing Bose-Einstein condensates of metastable helium using a single-beam optical dipole trap

This chapter is based upon: A.S. Flores, H.P. Mishra, W. Vassen and S. Knoop. "Simple method for producing Bose-Einstein condensates of metastable helium using a single-beam dipole trap." *Applied Physics B* 121, 391, 2015.

509242-L-bw-Flores
Processed on: 3-4-2017

Abstract

We demonstrate a simple scheme to reach Bose-Einstein condensation (BEC) of metastable triplet helium atoms using a single beam optical dipole trap with moderate power of less than 3 W. Our scheme is based on RF-induced evaporative cooling in a quadrupole magnetic trap and transfer to a single beam optical dipole trap that is located below the magnetic trap center. We transfer 1×10^6 atoms into the optical dipole trap, with an initial temperature of 14 μK, and observe efficient forced evaporative cooling both in a hybrid trap, in which the quadrupole magnetic trap operates just below the levitation gradient, and in the pure optical dipole trap, reaching the onset of BEC with 2×10^5 atoms and a pure BEC of 5×10^4 atoms. Our work shows that a single beam hybrid trap can be applied for a light atom, for which evaporative cooling in the quadrupole magnetic trap is strongly limited by Majorana spin-flips, and the very small levitation gradient limits the axial confinement in the hybrid trap.

3.1 Introduction

Quantum-degenerate atomic gases in optical dipole traps provide the starting point of many experiments. To realize these samples one can directly load a laser-cooled sample into an optical dipole trap (ODT) and perform evaporative cooling, which however requires very high ODT powers to provide sufficient trap volume, depth and confinement. Alternatively, one loads the atoms first in a magnetic trap and performs evaporative cooling, and afterwards transfers a dense and compact atomic cloud into an ODT, which now requires a much lower ODT power, at the expense of experimental complexity. Within this last category a very elegant approach is the hybrid trap (HT), introduced in Ref. [97], consisting of a simple quadrupole magnetic trap (QMT) and a single beam ODT. Efficient evaporation and Bose-Einstein condensation (BEC) have been demonstrated (see e. g. [97, 107, 117]), using ODT powers of only a few Watts. By switching off the QMT completely the atoms are transferred from the HT to a pure ODT.

The hybrid trap has been mostly applied to ^{87}Rb, but is assumed to be generally applicable to other magnetically trappable atomic species [97]. However, the application of HT strongly depends on the mass of atom. Most importantly, the rates of Majorana loss and heating, which determine the temperature that can be reached by evaporative cooling in a QMT, scale inversely with mass [9, 95]. This limits the transfer efficiency for light atoms, or puts constraints on the trap volume and trap depth, and therefore the power, of the ODT. Furthermore, for light atoms evaporative cooling in the HT is limited as the additional axial confinement provided by the QMT is

small because of the small levitation gradient, below which the QMT has to operate in the HT. Finally, the small levitation gradient puts experimental limits on the control of the displacement of the QMT with respect to the ODT, which further limits the axial confinement.

Here we report on the production of a metastable triplet helium (^{4}He*) BEC using a single beam HT with a moderate power of less than 3 W, demonstrating the application of HT for a light atom. Our work provides a novel and simple method for obtaining a ^{4}He* BEC, which can be used for atom optics experiments [118–122] or precision spectroscopy for fundamental tests of two-electron quantum electrodynamic theory [48, 123, 124]. So far, ^{4}He* BECs have been obtained in Ioffe-Pritchard or cloverleaf type of magnetic traps [33–35, 125–128], which has been subsequently transferred to a single beam [109, 129] or crossed beam ODT [48] (see Ref. [85] for a review on experimental work on ultracold ^{4}He*). Very recently a ^{4}He* BEC has been realized in a crossed beam ODT [130], using a total power of 26 W, in which the ODT is loaded from a QMT, following evaporative cooling to BEC in the ODT.

3.2 Single-beam hybrid trap for ^{4}He*

In the HT a single beam ODT is aligned slightly away from the QMT center, such that the trap minimum of the combined magnetic and optical trapping potential is at a finite magnetic field, and atoms do not suffer Majorana spin-flip losses once loaded in the HT. This also means that the atoms remain spin-polarized, which is crucial for ^{4}He* in order to avoid strong losses due to Penning ionization. After forced evaporative cooling in the QMT the magnetic field gradient of the QMT is ramped down such that the vertical gradient is equal or lower than the levitation gradient $B'_{\rm lev} \equiv mg/\mu$, at which the QMT alone cannot trap atoms. Here m is the mass, g is the gravitational acceleration and μ is the magnetic moment of the atom. Lowering the power in the ODT beam allows further evaporative cooling in the HT, in which the "hot atoms" can escape mainly downwards.

The combined potential of a QMT and single beam ODT is given by:

$$U(x,y,z) = \mu B' \sqrt{x^2 + 4y^2 + (z-z_0)^2} - \frac{2PC}{\pi w(y)^2} \exp\left[-2\frac{x^2+z^2}{w(y)^2}\right] + mgz, \tag{3.1}$$

where the first term is the QMT potential, the second term is the ODT potential, and the third term is the gravitational potential. In our case, the symmetry (strong) axes of the QMT and the ODT beam are along the y-axis. Here B' is the magnetic field gradient along the weak axis of the QMT, z_0 is the vertical displacement of the QMT with respect to the ODT ($z_0 > 0$ means that the ODT is placed below the QMT center), P is the power of the ODT beam, $C = \alpha_{\rm pol}/2\epsilon_0 c$ is a constant proportional to the

polarizability $\alpha_{\rm pol}$ depending on the atomic species and used wavelength λ, $w(y) = w_0\sqrt{1+y^2/y_R^2}$, where w_0 and $y_R = \pi w_0^2/\lambda$ are the beam waist ($1/e^2$ radius) and the Rayleigh length, respectively. We use $\lambda = 1557$ nm at which $C = 1.88 \times 10^{-36}$ J/(W m^{-2}) [111].

For HT the magnetic force in the vertical direction should be equal or smaller than gravity, which means in our geometry that $B' \leq B'_{\rm lev}$. For $B' = B'_{\rm lev}$ the trap depth is always given by $U_0 = 2PC/(\pi w_0^2)$, whereas for $B' < B'_{\rm lev}$ (or $B' = 0$ for a pure ODT) gravity leads to a reduction of the trap depth, which also depends on P, but this starts to be significant only for $P < 100$ mW. The radial confinement is dominated by the ODT potential. For ^{4}He*, the levitation gradient $B'_{\rm lev} = 0.35$ G/cm is very small, due to the small mass and relatively large magnetic moment $\mu = 2\mu_B$, where μ_B is the Bohr magneton. For comparison, the values for ^{87}Rb are 15 or 30 G/cm, depending on the Zeeman state. Therefore the additional axial confinement provided by the QMT, compared to the pure ODT, is limited in the HT, and only for low ODT power P the axial confinement is dominated by the QMT. In Fig. 3.1(a)-(d) we show the trapping potentials in both the radial and axial direction, for two different ODT powers, and z_0=0.1, 1 and 10 mm. Clearly, for $P = 3$ W the axial confinement of the ODT is still significant, while for $P = 0.3$ W the axial trapping potential is dominated by the QMT for sufficiently small z_0.

The peak density n_0 of a thermal sample is obtained from numerically solving the integral $\int \exp\left[-U(\vec{r})/k_BT\right] \mathrm{d}\vec{r} = N/n_0$, where $U(\vec{r})$ is the trapping potential (Eq. 3.1). A comparison between the HT (for z_0=0.1, 1 and 10 mm) and ODT is given in Fig. 3.1(e), showing n_0/N as function of the ODT power P (and T), assuming that T is determined by the trap depth according to $U_0 = \eta k_B T$ (and therefore $T \propto P$), taking a typical value of $\eta = 10$. Indeed, only for low P the peak density n_0 in the HT is significantly higher than that of the ODT. Also the dependence on z_0 becomes more prominent for low P. For heavier atoms, like ^{87}Rb, this regime is already reached at ODT powers well above 1 W.

The small $B'_{\rm lev}$ limits the confinement also in an indirect way. Any stray magnetic field $B_{\rm offset}$ will shift the center of the QMT, and therefore affects the displacement with respect to the ODT center, such that $z'_0 = z_0 + B^z_{\rm offset}/B'$. Those stray magnetic fields can be compensated by additional bias fields, however, magnetic field fluctuations translate in a jitter of the QMT center, which limits the smallest displacement that can be chosen for which the atoms do not experience a magnetic field zero. At $B' = B'_{\rm lev}$ magnetic field fluctuations on the order of 10 mG will already give a jitter of 0.3 mm in the location of the QMT. Furthermore, even in the absence of magnetic field fluctuations, the magnetic field offset at the location of the potential minimum of the HT, $B_0 = B'z_0$, has to be sufficiently large to provide a well-defined quantization axis, in order to suppress Majorana

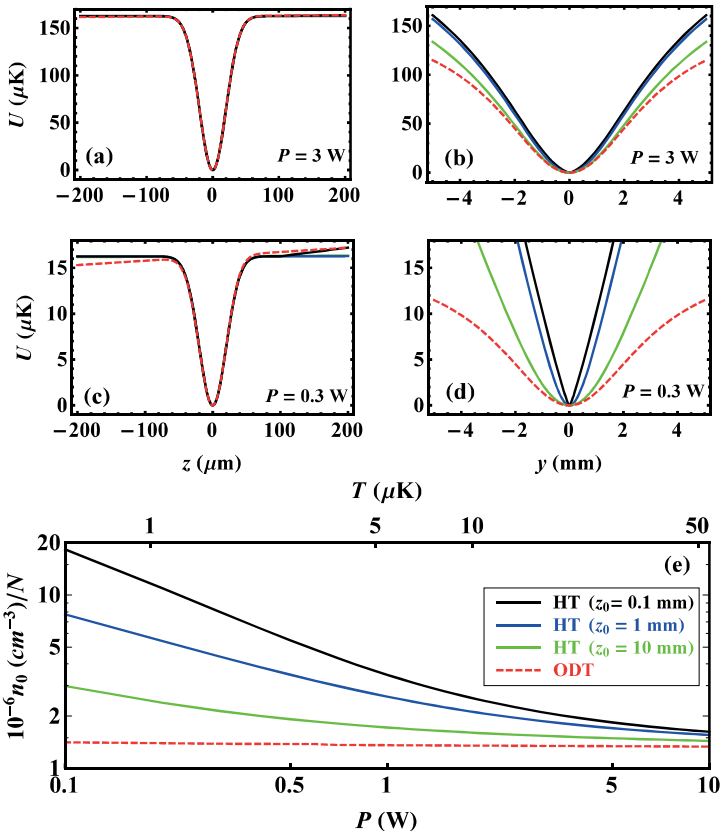

Figure 3.1: Trapping potentials and peak densities of HT (solid lines) and ODT (red dashed lines) for ^{4}He*, calculated for $B' = B_{\rm lev} = 0.35$ G/cm, $\lambda = 1557$ nm and $w_0 = 40$ μm (corresponding to $y_R = 3.2$ mm), using the trap potential given by Eq. 3.1. The displacement in case of the HT is $z_0 = 0.1$ mm (black), $z_0 = 1$ mm (blue) and $z_0 = 10$ mm (green). (a)-(d) Trapping potentials along the z-axis (vertical direction) and y-axis (axial direction), comparing ODT power $P = 3$ W and $P = 0.3$ W. (e) Peak densities n_0/N as function of P and T, assuming $k_BT = (1/10)U_0$ (and therefore $T \propto P$).

spin-flips and Penning ionization. For the heavier atoms this problem is much less severe. For instance, for ^{87}Rb in the $f = 2$, $m_f = 2$ state a small displacement of about a waist, say $z_0 = 50$ μm, already gives an offset field of 75 mG, and a magnetic field fluctuation of 10 mG in the vertical direction only gives a jitter of 6 μm in the displacement.

3.3 Experimental setup

The main part of our experimental setup has been described in Ref. [88], while our HT (applied to ^{87}Rb) has been discussed in Ref. [107]. In addition, a general description is given in Chapter 2. Here we will summarize the most important features and mention changes made compared to previous work. A schematic of the HT is given in Fig. 3.2, showing the QMT coils, ODT beam, absorption imaging beam and micro-channel plate (MCP) detector. The axial direction of the QMT, the ODT beam and the absorption imaging beam are in the horizontal ($x - y$) plane. Absorption imaging is used to

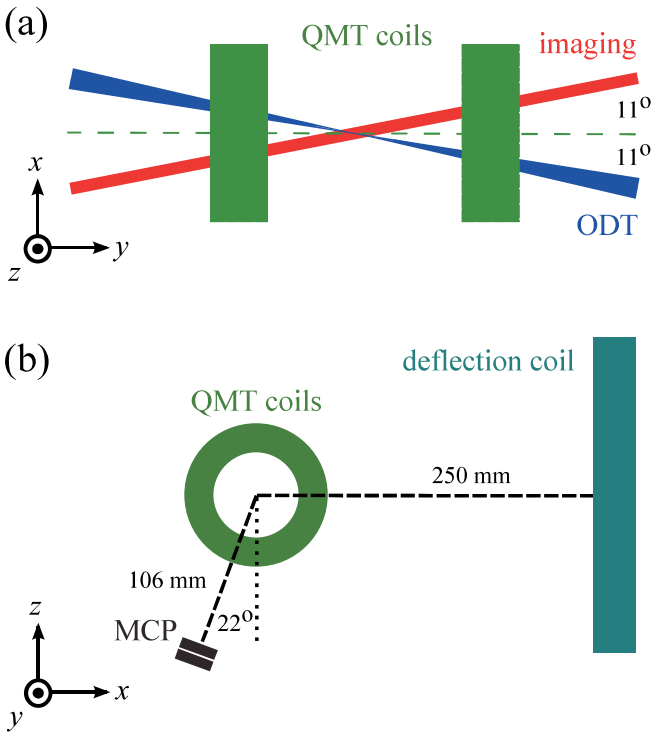

Figure 3.2: Schematics of our experimental setup, (a) showing the angles between the QMT axis, ODT beam and absorption imaging beam in the $x-y$ (horizontal) plane and (b) the location of the MCP detector and deflection coil in the $x - z$ plane.

obtain information about the atom number and temperature, as well as the position of the QMT and ODT. We use an InGaAs camera (Xenics) with 30 μm pixel size and our imaging setup has a magnification of 0.5.

We also record time-of-flight (TOF) spectra using a MCP detector, which is placed at a distance of 106 mm from the trap center, under an angle of 22° with respect to the direction of gravity, and has a diameter of 15 mm. For temperatures below 10 μK the ballistically expanding cloud, after switching off the trap, would not hit the MCP detector during its free fall. Therefore a short (10 ms) magnetic field gradient pulse is applied using a single "deflection" coil (see Fig. 3.2) to direct the atoms towards the MCP after release from the trap. The TOF spectra have a better resolution regarding temperature and observing BEC is much easier compared to expansion measurements with our absorption imaging system. However, the deflection field affects the TOF distribution and we need to use absorption imaging to calibrate the MCP detection regarding atom number and temperature.

Our single beam ODT has a waist $w_0 = 39.8 \pm 0.3$ μm (corresponding to a Rayleigh length of $y_R = 3.2$ mm) and the maximum power available at the setup is about $P = 3$ W, resulting in a maximum trap depth of $U_0 = k_B \times 160$ μK. We control the ODT power by an acousto-optical modulator (AOM), for which the output is coupled into a single mode fiber and sent to the experimental setup. The ODT beam enters the setup under an angle of 11° with respect to the QMT axis (see Fig. 3.2(a)), which leads to a reduction of the axial magnetic field gradient by a factor of $1 - \sin(11°)/2 \approx 0.90$, but does not affect the vertical magnetic field gradient.

An overview of our experimental scheme, in particular the magnetic field gradient B', RF-frequency ν_{RF} and ODT power P, is shown in Fig. 3.3. We use a liquid-nitrogen cooled dc-discharge source to produce a ^{4}He* beam,

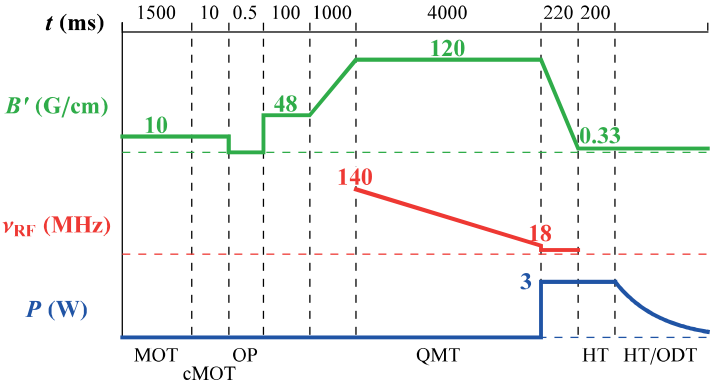

Figure 3.3: Overview of our experimental scheme for loading of and evaporation in the hybrid trap, showing the QMT gradient B', radiofrequency ν_{RF} and ODT power P.

which is collimated and subsequently decelerated in a 2.5 m long Zeeman slower and loaded into a magneto-optical trap (MOT). An *in vacuo* shutter after the collimation section is opened only during the loading time of the MOT. The pressure in the main vacuum chamber is 1×10^{-10} mbar. We load about 5×10^8 ^{4}He* atoms at a temperature of about 1 mK within 1.5 s in the MOT, which consists of three retroreflected 2-inch laser beams at 1083 nm with a total power of $\sim$ 45 mW and a large detuning of -33 MHz (21 linewidths), and a magnetic field gradient (weak axis) of 10 G/cm. Compared to Ref. [88] we have improved our atom number by increasing the MOT beam diameter from 1- to 2-inch. Afterwards we compress the cloud (the "cMOT" stage) by ramping down the detuning to -6 MHz in 10 ms, during which the power is reduced by a factor of ten, while keeping the same magnetic field gradient. After this cMOT stage we end up with 3×10^8 atoms at a temperature of 260(10) μK. Before loading in the QMT we optically pump (OP) the atoms into the m_s=+1 magnetic trappable state in 0.5 ms, during which the magnetic field gradient is switched off. Then we switch on abruptly the QMT at $B' = 48$ G/cm and stay for 100 ms, and then ramp in 1 s to B'=120 G/cm. At this point we have about 1×10^8 atoms at a temperature of about 1 mK.

After loading in the QMT, we apply RF-induced forced evaporative cool-

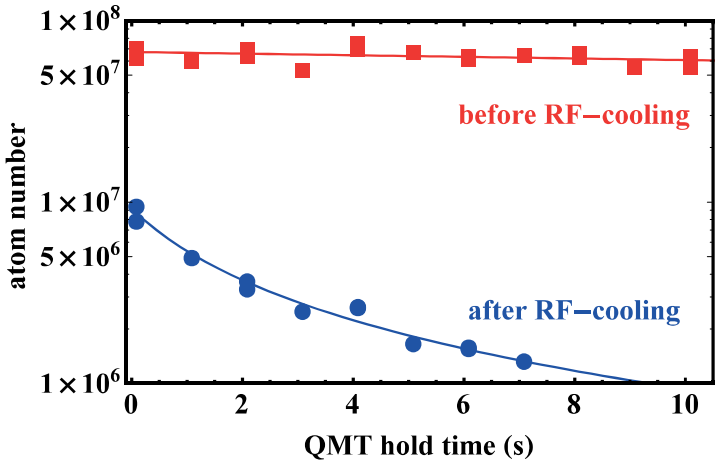

Figure 3.4: Lifetime in the QMT, before RF-cooling (red squares) and after RF-cooling (blue circles). Before RF-cooling we observe a slow, exponential decay of the number of trapped atoms, where the lifetime is limited by background collisions. After RF-cooling we observe a fast, non-exponential decay. Lines are the result of a loss model that includes Majorana loss and heating, fitted to the data.

ing, resulting in an effective trap depth $U_0^{\text{eff}} = h\nu_{\text{RF}}$. We generate the RF frequency ν_{RF} by frequency doubling the output of a tunable 80 MHz function generator. After several amplification stages we send up to 5 W of RF power to a coil that is placed inside the vacuum chamber. We ramp down ν_{RF} from 140 MHz to 18 MHz in 4 s, corresponding to a final trap depth of $k_B \times 0.9$ mK. At this point the lifetime of the trapped atoms is only a few seconds, caused by Majorana spin-flips, which has a loss rate of $\Gamma_{\text{M}} = \chi(\hbar/m)(2\mu B'/k_B T)^2$ [95]. In Fig. 3.4 we show the lifetime of the trapped atoms in the QMT, before and after RF cooling, where we have fitted the data with a loss model that includes Majorana loss and heating [95, 130]. The lifetime data after RF-cooling are consistent with a temperature of $150 - 220$ μK for a χ factor between 0.1 and 0.2 [95, 130]. To load the HT we switch on the ODT light at maximum power and ramp down the QMT gradient from $B' = 120$ G/cm to $B' = 0.33$ G/cm (just below B'_{lev}) in 220 ms. During the ramp down ν_{RF} is set at 9 MHz. Afterwards, an additional 200 ms is used to fine-adjust the bias fields to control the displacement (see Section 3.4.2). For loading of a pure ODT we switch off the QMT gradient during this last stage, while switching on a bias magnetic field in the axial direction to provide a quantization axis in order to keep the atoms spin-polarized.

3.4 Results

3.4.1 Loading of HT or ODT

For the alignment of the ODT beam we use a piezo-mirror to scan in both the horizontal (x-axis) and vertical (z-axis) direction and monitor the number of atoms loaded into the HT or ODT. Typical measurements are shown in Fig. 3.5(a)-(b). In both directions one finds a minimum when the ODT is located at the center of the QMT, which is due to Majorana loss, and the width of the loss feature is on the order of the waist. We position our ODT about 60 μm below the QMT center. We obtain up to 1×10^6 atoms at a temperature of 14 μK for both HT and ODT. The transfer efficiency from the QMT to the HT or ODT is about $5 - 10\%$.

We have measured the number of loaded atoms for different initial ODT powers in order to investigate to what extent we are limited by our maximum ODT power of 2.8 W. The results are shown in Fig. 3.5(c). The number of loaded atoms does not fully saturate, meaning that the number of transferred atoms is limited by our ODT power. At the maximum power we measure a 1/e trapping lifetime of more than 20 s of the HT and pure ODT, at which the calculated off-resonant photon scattering at 1557 nm is $(6\text{ s})^{-1}$, but the recoil temperature of 2 μK is much smaller than the trap depth.

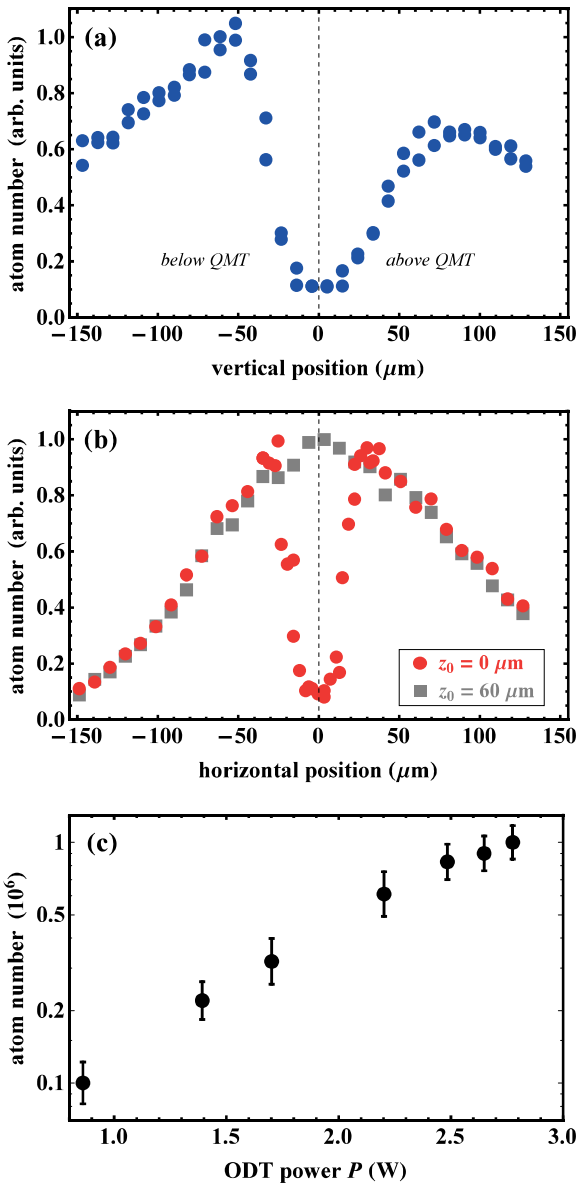

Figure 3.5: Number of atoms loaded in the hybrid trap at $P = 2.8$ W as function of position of the ODT (using a piezo-mirror) with respect to the QMT center in the vertical direction (a) and horizontal direction (b). The gray data in (b) shows a scan in the horizontal, while the vertical position is 60 μm below the QMT center. Panel (c): number of atoms loaded in the hybrid trap as function of ODT power P, with vertical displacement of 60 μm.

3.4.2 Control of QMT displacement in HT

During the QMT stage magnetic bias fields are set to minimize stray magnetic fields at the center of the trap and we use the piezo-mirror to adjust the displacement of the ODT with respect to the QMT center. However, in the HT this displacement becomes very sensitive to bias fields, which provides a much broader tuning range (up to a few cm) compared to the piezo-mirror (limited to 0.3 mm). Therefore, once the atoms are loaded in the HT, we fine-adjust these magnetic bias fields to set the displacement of the QMT center with respect to the ODT, while keeping the piezo-mirror at the optimal loading condition (see Fig. 3.5(a)-(b)). In scanning the bias fields in the

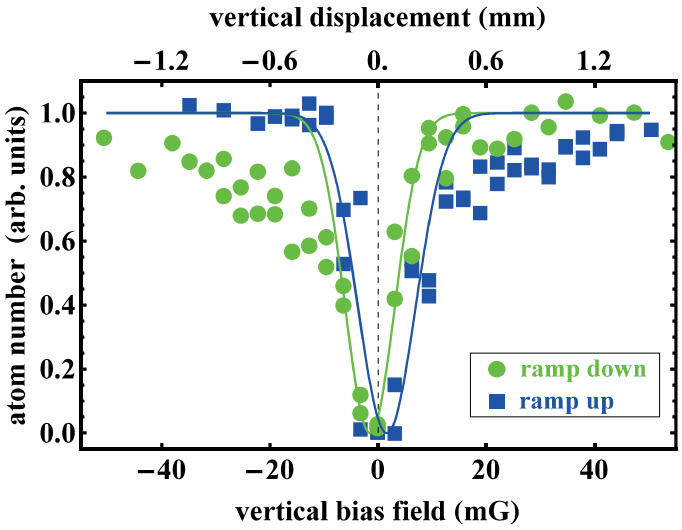

Figure 3.6: Number of atoms in the hybrid trap as function of an applied vertical bias field that controls the positions of the QMT center with respect to the ODT. After the vertical bias field is set to its final value the total hold time is 300 ms, during which the ODT power is ramped down from $P = 2.8$ W to 2.2 W. The loss resonance occurs due to Majorana spin-flips when the center of the QMT is overlapped with the ODT. An asymmetry and broadening of the loss feature is caused by the slow response of the magnetic field coil. Two sets of data are shown, for which we ramp up from a value just below the resonance (blue squares) or ramp down from above the resonance (green circles). The solid lines are Gaussian fits taking into account only the fast slopes. The resonance position is determined by the average of the two Gaussian centers. With the magnetic field gradient of 0.33 G/cm in the vertical direction, the vertical bias field can be converted into vertical displacement using $z_0 = B_z/B'$.

x- and z-direction we do observe loss resonances at which atoms are lost on the time scale of 100 ms. Again, those losses are due to Majorana spin-flips in which the atoms can leave the HT in the axial direction. In Fig. 3.6 we show the number of atoms in the HT as function of vertical bias field after a hold time of 300 ms, in which we jump to the field value from below and above the resonance position. The asymmetry of the loss resonances is due to the slow response of the magnetic field coils. However, by fitting Gaussian distributions to the two scans, in which the slow rising part of the data is omitted, the centers and actual widths can be determined, where the actual center is taken as the average of the two centers. We find a $1/e^2$ width of 5 mG and the center is reproducible within 3 mG on a day-to-day basis.

While the center of the loss resonance fixes $B_z = 0$, the displacement is simply given by $z_0 = B_z/B'$. Here $B' = 0.33$ G/cm, which means that the width of 5 mG already corresponds to 0.15 mm. This width is much larger than observed in scanning the ODT by means of the piezo-mirror to find the optimum loading conditions (see Fig. 3.5), where the width is on the order of the waist. This can be explained by assuming that the atoms are transferred from the QMT to the HT already at $B' >> B'_{\mathrm{lev}}$, where the sensitivity to magnetic bias fields is much less. It also means that the displacement assigned in the measurement of Fig. 3.5 only holds for the loading, not the final HT. While the piezo-mirror is optimized on the loading, we use the magnetic bias fields to set the displacement of the final HT, which also covers a much broader range. In the x-direction we set the bias field "on resonance" ($x_0 = 0$), and control the displacement with the vertical bias field. In order not be effected by Majorana spin-flips a displacement larger than 0.3 mm has to be chosen, which limits the axial confinement and the peak density (see Fig. 3.1), and the displacement jitters by 0.15 mm. Again, such constraints are essentially not present for the heavier atoms, in which the displacement can be chosen to be on the order of a waist and the jitter is much smaller than the waist.

3.4.3 Evaporative cooling in HT and ODT

After loading the HT or ODT we perform forced evaporative cooling to lower the temperature and increase the phase-space density by ramping down the ODT power. A sample of TOF spectra obtained by the MCP detector is shown in Fig. 3.7. In the regime where the kinetic energy is much smaller than the gravitational energy, i. e. $k_B T << mgh$, where h is the height difference between the trap and the detector, the TOF spectrum of a thermal sample is described by a Gaussian distribution with a width that is proportional to the square-root of the temperature. Indeed, for lower ODT power we observe a narrowing of the distribution, but also an increase of the signal, which is due to the finite size of the MCP detector. For a thermalized sample the temperature is proportional to the trap depth $U_0 = 2PC/(\pi w_0^2)$

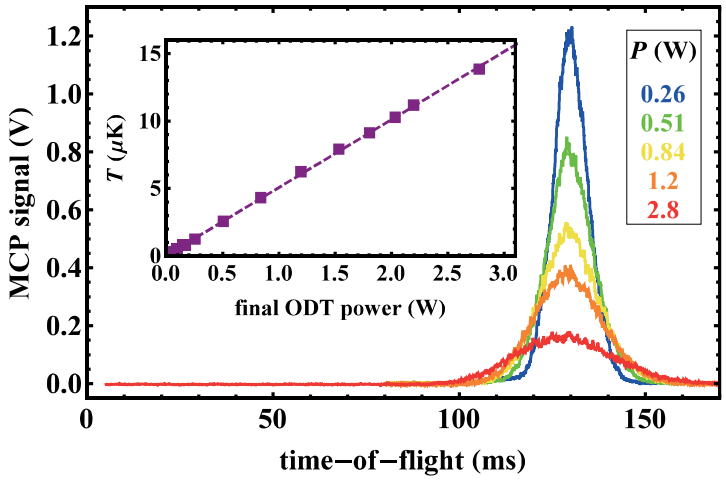

Figure 3.7: Forced evaporative cooling in the pure ODT, showing TOF spectra obtained by the MCP detector for different final ODT powers. The inset shows the temperature, obtained from the width of the TOF spectra, as function of final ODT powers (dashed line is a linear fit), from which a truncation parameter of $\eta = U_0/k_BT = 11$ is obtained. Each TOF spectra is an average over 5 experimental runs.

via the truncation parameter $\eta = U_0/k_BT$. Indeed, we find the width to be proportional to the square-root of the ODT power P. By fitting the relation $\sigma = a\sqrt{P} + b$ to the data we find a small offset b of about 1 ms, which is probably caused by the magnetic field gradient pulse that we apply after release from the trap to direct the atoms towards the MCP. Before converting the width into temperature we correct for this offset. Absolute calibration of the temperature is done by absorption imaging at $P = 2.8$ W, at which we have measured 13.9 ± 0.2 μK. The result is shown in the inset of Fig. 3.7, in which the data shows a linear behavior for the full range of ODT powers. From the slope one directly obtains η, which turns out to be 11 for both HT and ODT.

First we investigate the time-scale of forced evaporative cooling, comparing HT ($z_0 = 1.5$ mm) and ODT. We note that the initial conditions are the same in terms of temperature (14 μK) and atom number (1×10^6), while the peak density and the collision rate are slightly higher for the HT (2.1×10^{12} cm^{-3} and 410 s^{-1} for HT; 1.7×10^{12} cm^{-3} and 320 s^{-1} for ODT). We ramp down the ODT power from $P = 2.8$ W to 0.26 W for variable ramp times. A sample of TOF spectra are shown in Fig. 3.8(a), for the HT and ODT (inset). Two striking observations can be made: first of all the time-scale for thermalization is much shorter for the ODT than

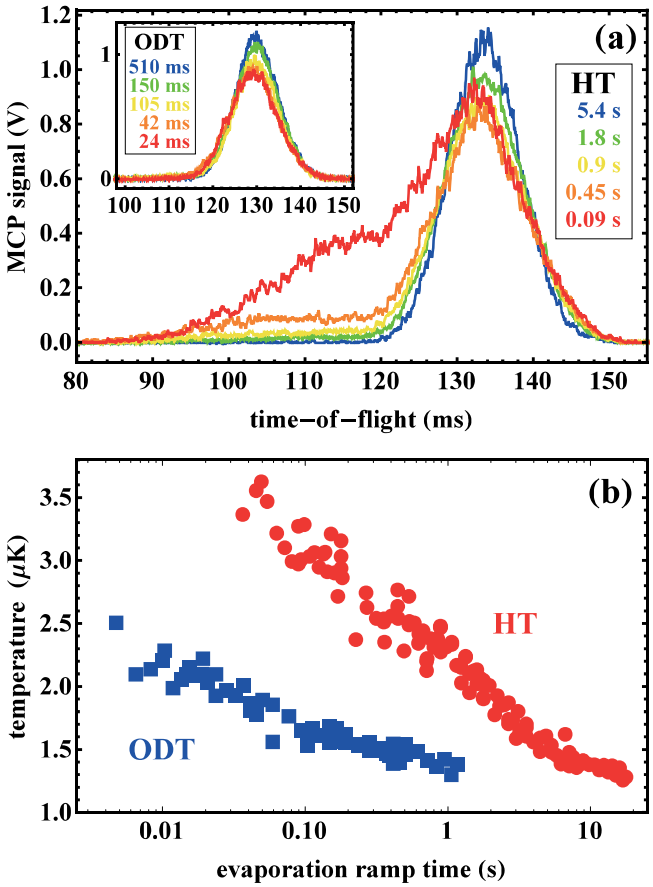

Figure 3.8: Forced evaporative cooling in HT (with $z_0 = 1.5$ mm) and ODT, ramping down the ODT power from $P = 2.8$ W to 0.26 W. (a) TOF spectra for HT and ODT (inset) for different evaporation ramp times (each TOF spectrum is an average over 2 to 4 experimental runs). (b) Temperature as function of ramp time for HT and ODT. The initial temperature at $P = 2.8$ W is 14 μK.

the HT, and secondly, a shoulder on the left side of the TOF peak appears for short evaporation ramp times in the HT, corresponding to "hot atoms" that remain trapped. In Fig. 3.8(a) we show the temperature, obtained by a fit of the main TOF peak, as function of evaporation ramp time. The initial temperature at $P = 2.8$ W is 14 μK, while the final temperature at $P = 0.26$ W is 1.3 μK. For the ODT a temperature of 1.5 μK is reached in 100 ms, which for the HT it takes about 3 s. We have observed similar behavior for a HT at a much larger displacement of $z_0 = 15$ mm, and a HT at about half the levitation gradient ($B' = 0.16$ G/cm, $z_0 = 1.2$ mm).

We explain these observation by the dimensionality of evaporation: while in the ODT the atoms can escape in all directions, in the HT they can only escape downwards. Therefore the removal of "hot atoms" takes much longer, even though the collision rate in the HT at $P = 0.26$ W is about twice that of the ODT (1.5×10^{12} cm^{-3} compared to 7×10^{11} cm^{-3}). The required evaporation ramp time for the ODT compares quite well with a calculated thermalization rate at $P = 0.26$ W of (70 ms)$^{-1}$, while the axial trap frequency is $2\pi \times 12$ Hz. The longest time scale of the HT is the axial trap frequency of $2\pi \times 27$ Hz.

After having determined the appropriate ramp times (also for lower final ODT powers) we study the efficiency of evaporation by measuring the atom number and temperature for different final ODT power. In Fig. 3.9(a) we show the temperature as function of atom number in the HT for two displacements, $z_0 = 0.6$ mm and $z_0 = 1.5$ mm, and the ODT. Here the efficiency is typically quantified as $\alpha = \mathrm{d}[\log T]/\mathrm{d}[\log N]$, and we observe a α parameter between 2 and 3. For the same final temperature we obtain the highest atom number for ODT and the lowest one for the HT with the smallest displacement.

In Fig. 3.9(b) we present the phase-space density $D = n_0 \lambda_{\mathrm{dB}}^3$ (where $\lambda_{\mathrm{dB}} = h/\sqrt{2\pi m k_B T}$ is the de Broglie wavelength) as function of atom number, for which the peak density n_0 is calculated using numerical integration of Eq. 3.1 (see Section 3.2). Here the efficiency is typically quantified as $\gamma = -\mathrm{d}[\log D]/\mathrm{d}[\log N]$, and we observe a γ parameter between 2 and 3. We reach the onset of BEC ($D > 1$) in all three cases, with the most atoms of 2×10^5 for the HT with $z_0 = 1.5$ mm, showing a slightly better performance than the one with $z_0 = 0.6$ mm. But even for the single beam ODT we obtain efficient evaporation up to $D = 1$ with $\gamma > 2$, which is probably explained by the sufficiently large axial trap frequencies of at least a few Hz.

The appearance of BEC can be observed in the TOF spectra obtained by MCP detection, as it provides a distinct TOF distribution described by an inverted parabola,

$$\Phi_{\mathrm{BEC}}(t) \propto \max\left[0, 1 - \left(\frac{t - t_0}{\sigma}\right)^2\right]^2, \tag{3.2}$$

where the width σ is given by the chemical potential [33, 35, 126]. Compared

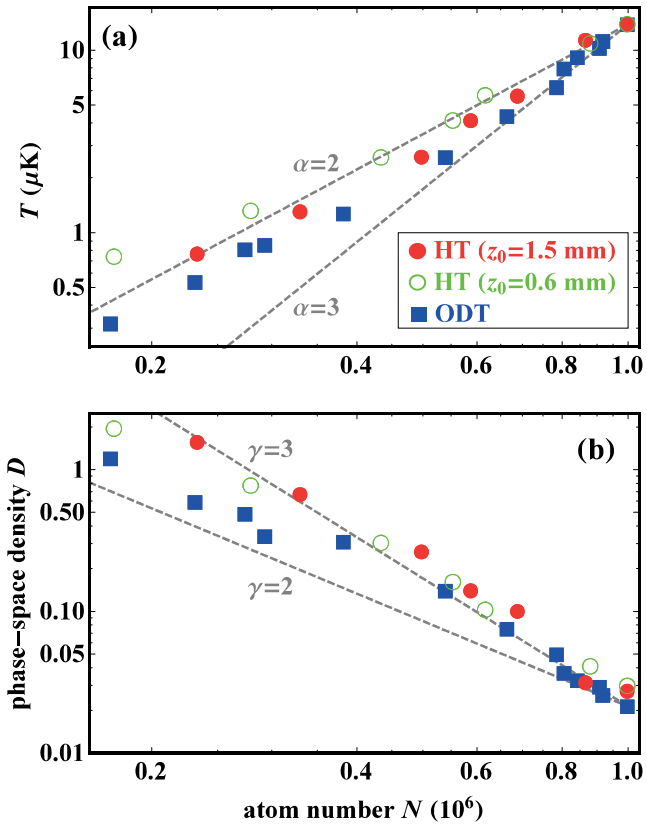

Figure 3.9: Evaporative cooling in the HT $z_0 = 0.6$ mm and $z_0 = 1.5$ mm and ODT, showing (a) the temperature and (b) phase-space density as function the atom number. The gray dashed lines indicate the efficiency in terms of $\alpha = \mathrm{d}[\log T]/\mathrm{d}[\log N]$ and $\gamma = -\mathrm{d}[\log D]/\mathrm{d}[\log N]$ parameters.

to the Gaussian distribution associated with a thermal sample, a BEC gives rise to much sharper wings of the distribution. In our case, the magnetic field gradient pulse, which is required to direct the atoms towards the MCP after release from the trap, affects the narrow BEC TOF peak, and we do not obtain clear bimodal distributions in which the thermal and BEC part can easily be distinguished. Nonetheless, for the lowest final ODT powers we do observe a sharpening of the wings of the TOF distribution. In Fig. 3.10(a) we show a series of TOF spectra of the HT with $z_0 = 1.5$ mm for decreasing ODT power, for which $D > 1$. The narrowing of the TOF distributions can be explained by both a decreasing temperature and a decreasing chemical potential, due to reduction of trap frequencies. In Fig. 3.10(b)-(c) we show pure thermal and BEC fits to the situation of (b) $D \approx 1$ (c) and $D >> 1$.

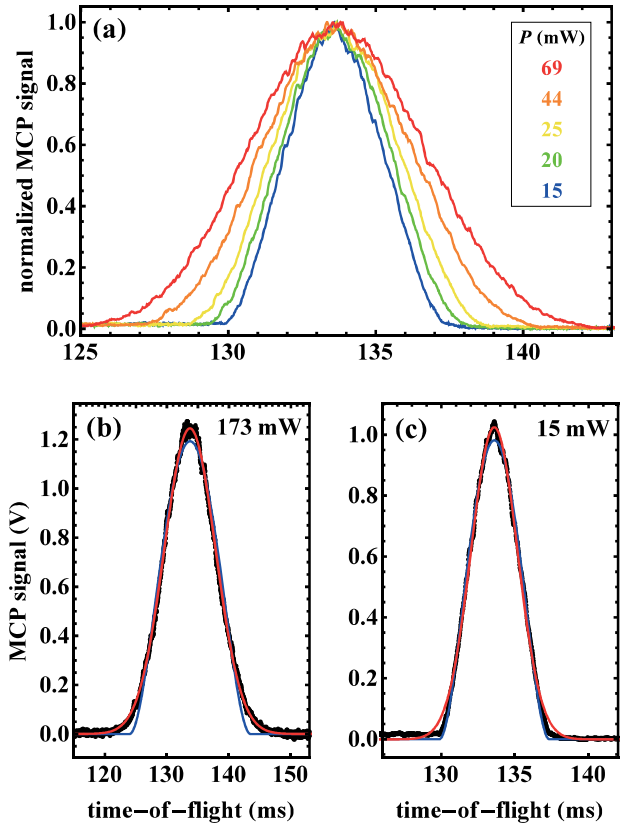

Figure 3.10: (a) Normalized TOF spectra of the HT with $z_0 = 1.5$ mm for different final ODT powers at which $D > 1$, showing a sharpening of the wings of the distributions. Panel (b) and (c) show TOF spectra for $P = 173$ mW and $P = 15$ mW, for which $D \approx 1$ and $D >> 1$, respectively, together with Gaussian fits (red) and BEC fits (blue, Eq. 3.2). Each TOF spectrum is an average over 5 experimental runs. The shot-to-shot fluctuation in the signal height is less than 5 %.

Indeed, the BEC distribution describes the TOF spectrum of panel (c) quite well, much better than the thermal fit. From this observation we estimate that we have reached a pure BEC of 5×10^4 atoms.

3.5 Conclusions

We have achieved Bose-Einstein condensation (BEC) of metastable triplet helium atoms via RF-induced evaporative cooling in a quadrupole magnetic trap, transfered to a single beam hybrid trap, and subsequent evaporative cooling in both the hybrid trap and pure optical dipole trap, using only moderate ODT power of less than 3 W. While evaporation in the pure ODT is much faster than that in the HT, a larger BEC is obtained in the HT. We reach the onset of BEC with 2×10^5 atoms and a pure BEC of 5×10^4 atoms. We observe small shot-to-shot fluctuations (less than 5%) and excellent day-to-day reproducibility. The total experimental cycle duration is between 8 to 10 s. This all could be improved by the implementation of a bright molasses [131] and gray molasses [130] before loading the QMT, which would provide better initial conditions of RF-induced forced evaporative cooling in the QMT and therefore shorten the duration of that stage, and finally lead to a larger BEC. Our present work provides the most simple scheme so far to obtain a ^{4}He* BEC, using limited experimental infrastructure. It also shows that a single beam hybrid trap can be applied for a light atom such as helium, despite several challenges caused by its small mass and small levitation gradient.

509242-L-bw-Flores
Processed on: 3-4-2017

Chapter 4

An ultracold, optically trapped mixture of ^{87}Rb and metastable ^{4}He atoms

This chapter is based upon: A.S. Flores, H.P. Mishra, W. Vassen and S. Knoop. "An ultracold, optically trapped mixture of ^{87}Rb and metastable ^{4}He atoms." *European Physical Journal D* 71, 49, 2017.

509242-L-bw-Flores
Processed on: 3-4-2017

Abstract

We report on the realization of an ultracold ($< 25\ \mu$K) mixture of rubidium (^{87}Rb) and metastable triplet helium (^{4}He) in an optical dipole trap. Our scheme involves laser cooling in a dual-species magneto-optical trap, simultaneous MW- and RF-induced forced evaporative cooling in a quadrupole magnetic trap, and transfer to a single-beam optical dipole trap. We observe long trapping lifetimes for the doubly spin-stretched spin-state mixture and measure much shorter lifetimes for other spin-state combinations. We discuss prospects for realizing quantum degenerate mixtures of alkali and metastable helium atoms.

4.1 Introduction

Ultracold mixtures of distinct atomic species serve for many scientific goals: sympathetic cooling of atomic species for which evaporative cooling is inefficient [28, 29, 52], creation of ultracold polar molecules [25], exploring many-body physics in quantum degenerate Bose-Bose, Bose-Fermi and Fermi-Fermi atomic mixtures [132–134], studying impurities immersed in Bose or Fermi gases [54–56, 135], heteronuclear few-body physics [70, 71], and testing universality of free-fall [57].

Most mixtures of chemically distinct atomic species consist of alkalis: Li+Na [52], Li+K [58, 133, 136], Li+K+Rb [60], Li+Rb [59], Li+Cs [61, 137, 138], Na+K [62], Na+Rb [63], K+Rb [28, 53, 139], K+Cs [64], Rb+Cs [65, 140]. These experimental efforts laid the foundation of the creation of ultracold heteronuclear ground-state molecules, which posses a large permanent dipole moment: KRb [25], RbCs [66, 67], NaK [68] and NaRb [69]. Another example is the observation of successive Efimov states in Li+Cs [70, 71], benefiting from the largest possible mass ratio within the alkali group. In most of these cases preparation in an optical dipole trap [100] is essential, in particular to allow for tunable interaction and magneto-association by means of magnetically induced Feshbach resonances [19].

Recently also mixtures of alkali and Yb or Sr atoms have become available: Rb+Yb [73, 74], Li+Yb [75, 76, 134], Rb+Sr [72], and efforts towards Cs+Yb [77]. Here the main interest comes from the doublet $^{2}\Sigma^{+}$ molecular ground state potential that gives rise to both electric and magnetic tunability of the associated molecules, in contrast to the singlet $^{1}\Sigma^{+}$ ground state potential of bialkali molecules. However, for these systems only very narrow Feshbach resonances are expected [141–143], and so far no resonance has been observed. This has triggered work towards mixtures involving metastable Yb(^{3}P$_{2}$) [144, 145], for which broader resonances are expected, however accompanied with strong inelastic two-body losses [146, 147].

Here we have realized an optically trapped, ultracold mixture of an alkali

and helium in the metastable 2 $^3S_1$ state (He*). Ultracold mixtures of alkali atoms and fermionic ^{3}He* or bosonic ^{4}He* provide new Bose-Bose, Bose-Fermi and Fermi-Fermi mixtures, with an extended range of possible mass ratios. The scattering properties of He*+alkali collisions are described by a shallow quartet $^4\Sigma^+$ potential and a deeper doublet $^2\Sigma^+$ potential. Accurate *ab initio* calculations of the quartet $^4\Sigma^+$ potentials and the corresponding quartet scattering lengths have recently become available for Li, K, Na and Rb [87], and while most of the doublet $^2\Sigma^+$ potentials have been studied experimentally and theoretically in the past (see e. g. [89, 148–151]), the doublet scattering lengths are unknown. Importantly, the large internal energy of 19.8 eV of He* leads to Penning ionization (PI):

$$\mathrm{He}(2\ ^3\mathrm{S}_1) + \mathrm{A}(^2\mathrm{S}_{1/2}) \rightarrow \mathrm{He}(1\ ^1\mathrm{S}_0) + \mathrm{A}^+(^1\mathrm{S}_0) + \mathrm{e}^-, \tag{4.1}$$

resulting in trap loss. Fortunately, PI is suppressed for pure quartet scattering due to spin-conservation, which is essential for realizing a stable ultracold mixture. This requires He* and the alkali atom to be both prepared in either the low-field or high-field spin-stretched spin-state. For other spin-state combinations, relevant for Feshbach resonances, the PI loss rate depends on the amount of doublet character of the particular entrance channel. A crucial assumption here is that the first excited (non-spin-singlet) A^+ state is energetically not available, which is true for all alkali atoms except Cs.

Our experiment involves an ultracold mixture of ^{4}He*+^{87}Rb, for which dual-species laser-cooling and trapping was first achieved by the Truscott group [91]. Magnetic trapping of the stable, doubly spin-stretched spin-state combination $|m_s = +1\rangle_{^4\mathrm{He}^*} + |f = 2, m_f = +2\rangle_{^{87}\mathrm{Rb}}$ (see Fig. 4.1) has also been reported [88, 92], providing upper limits of the PI loss rate for quartet scattering on the order of 10^{-12} cm^{3}s^{-1}, and revealing a small quartet scattering length in agreement with *ab initio* calculations [87, 88].

In this chapter, we focus on the experimental realization of the ultracold mixture in the optical dipole trap, giving a detailed discussion on the different preparation stages and emphasize the challenges of the mixture compared to the single-species situation. Finally, we present lifetime measurements, comparing the doubly spin-stretched spin-state with the energetically lowest spin-state combination $|m_s = -1\rangle_{^4\mathrm{He}^*} + |f = 1, m_f = +1\rangle_{^{87}\mathrm{Rb}}$, and outline the consequences for dual-species quantum degeneracy and Feshbach spectroscopy.

4.2 Experiment

Details of our experimental setup have been given in Ref(s). [88, 107, 108], and Chapters 2 and 3. In here, we focus on the scheme that is relevant for simultaneous loading of the two atomic species in an optical dipole trap. We start by loading both species in a three-dimensional magneto-optical

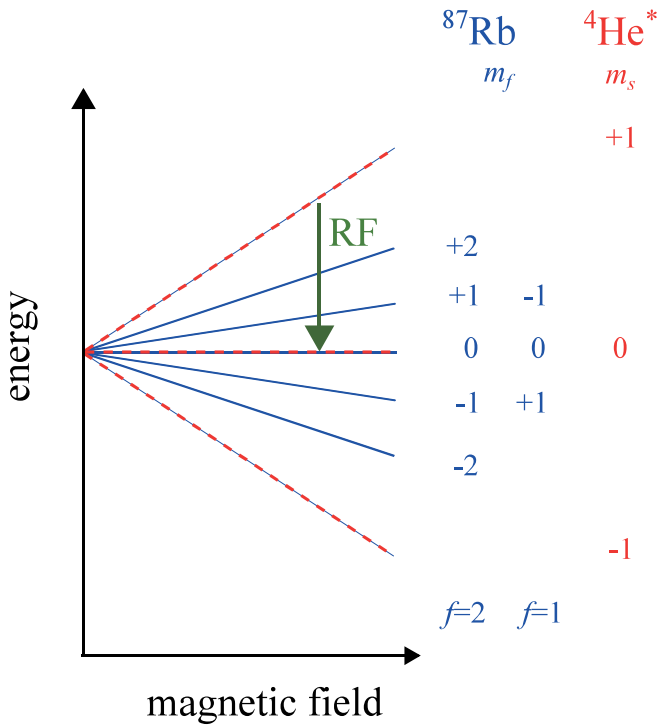

Figure 4.1: Ground state Zeeman splitting diagram of ^{87}Rb (blue) and ^{4}He* (red-dashed) showing the possible different spin-state combinations that can be prepared. Also depicted in the diagram is the difference in the Zeeman splitting between He* ($2\mu_{\mathrm{B}}B$) and Rb ($\mu_{\mathrm{B}}B/2$) allowing the possibility to transfer He* atoms between the Zeeman states using RF without affecting Rb. The hyperfine splitting between the $f = 2$ and $f = 1$ states of ^{87}Rb is 6.835 GHz and a MW sweep is used to transfer Rb atoms between these states.

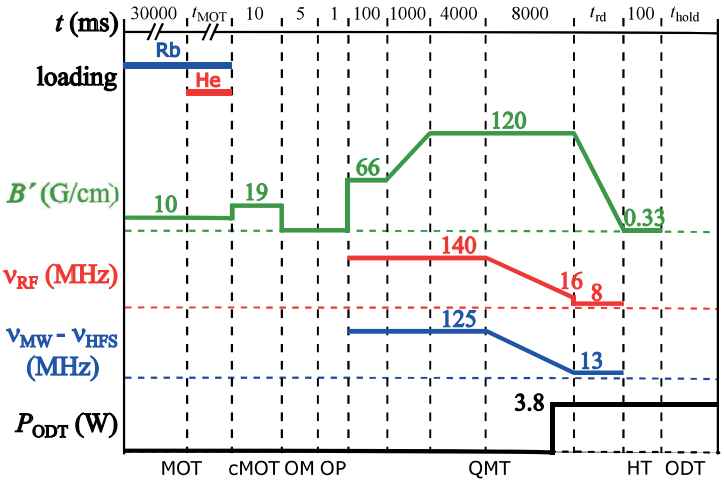

Figure 4.2: Summary of the loading scheme for the preparation of the ultracold mixture of ^{87}Rb and ^{4}He* in an optical trap. Shown are the magnetic field gradient, MW and RF frequencies, and ODT power corresponding to the different trapping stages. Typical MOT loading time t_{MOT} of He* is less than 1 s and the QMT ramp down duration t_{rd} is between 0.5 to 2 s.

trap (3D-MOT), after which the mixture is further cooled in an optical molasses (OM). After optical pumping (OP) to the desired low-field seeking doubly spin-stretched spin-state, the sample is transferred to a quadrupole magnetic trap (QMT) for further evaporative cooling using microwave (MW) and radiofrequency (RF) for Rb and He*, respectively. Finally, the sample is loaded into a single-beam optical dipole trap (ODT) using the hybrid trap (HT) as an intermediate stage. A summary of the loading scheme starting from the MOT stage towards the ODT is illustrated in Fig. 4.2.

In the following subsections, we briefly describe the different stages involved in the preparation of our ultracold mixture and discuss important issues regarding simultaneous loading as compared to our single-species experiments [107, 108] and previous mixture experiment [88]. We also describe our simultaneous detection scheme and explain the preparation of different spin-state samples using MW and RF frequency sweeps. An overview of the Zeeman states is given in Fig. 4.1.

4.2.1 Two-species MOT

Our 3D-MOT consists of three 2-inch retro-reflected beams containing the cooling light of both species. Changing from 1-inch [88, 107] to 2-inch 3D-MOT beams was motivated by the fact that sympathetic cooling of He* with Rb is not efficient, therefore forced evaporative cooling is required and thus the need to start with sufficient He* atom number. An order of

magnitude improvement is observed in the He* 3D-MOT atom number as already reported in Ref. [108]. Correspondingly, the Rb 3D-MOT atom number also improves by at least a factor of three compared to Ref. [107].

The quadrupole magnetic field is derived from a pair of coils in anti-Helmholtz configuration, and the magnetic field gradient is 10 G/cm along the weak axis. The total 3D-MOT incoming power for Rb is around 20 mW and the light is detuned by -20 MHz with respect to the laser cooling transition (natural linewidth is 6 MHz). For He*, the light is detuned by -33 MHz, about 20 times the natural linewidth of 1.6 MHz, to reduce light-assisted intraspecies Penning ionization loss [79, 80, 104]. The total incoming 3D-MOT power is around 30 mW. We deliver these beams to the setup via polarization maintaining (PM) fibers where we couple the 3D-MOT beams of the two species in the same fiber using dichroic mirrors. Rb atoms are loaded from a 2D-MOT with two distinct pushing beams [88, 105] and He* atoms are loaded from a Zeeman slower. We first load the Rb atoms in 30 s followed by He* loading typically in less than 1 s. To minimize the continuous flux of ground state He (metastable to ground state fraction is 10^{-4}), an in-vacuo shutter is introduced between the source and the Zeeman slower, which is only open during the He* loading. Typically, we lose between 15 to 20% of the Rb atoms in the 3D-MOT due to the combined effect of background collisions with thermal ground-state and metastable He atoms. At the end of this stage, we have at least 3×10^9 (Rb) and 3×10^8 (He*) atoms at a temperature of a few hundreds of μK (Rb) and 1 to 2 mK (He*), respectively. After loading the two atomic species, we compress the sample by abruptly increasing the gradient to 19 G/cm while the detunings are ramped to -15 MHz (Rb) and -5 MHz (He*) in 10 ms (cMOT stage). Afterward, the 3D-MOT gradient is switched off and the power of the 3D-MOT beams is reduced by almost a factor of 10 for further cooling in the OM stage. However, the power imbalance between the incoming and reflecting 3D-MOT beams limits the allowed duration of the OM stage in order for the clouds not to deviate too far from the center of the QMT. To compensate for this, we offset the alignment of the 3D-MOT beams with respect to the QMT center such that at the end of the OM, the clouds coincide with the position of the QMT. After a 5 ms OM stage, we apply simultaneous OP (around 150 μW each) on both species for a duration of 1 ms in order to prepare the sample in the doubly spin-stretched spin-state before transferring to the QMT for further cooling.

4.2.2 Simultaneous evaporative cooling in the QMT

For magnetic trapping, we have used the same coils to create the quadrupole magnetic trap as used in the 3D-MOT. After the OP stage, we abruptly increase the gradient to 66 G/cm and stay for 100 ms in order to facilitate the initial transfer to the QMT. The gradient is then ramped up to 120 G/cm

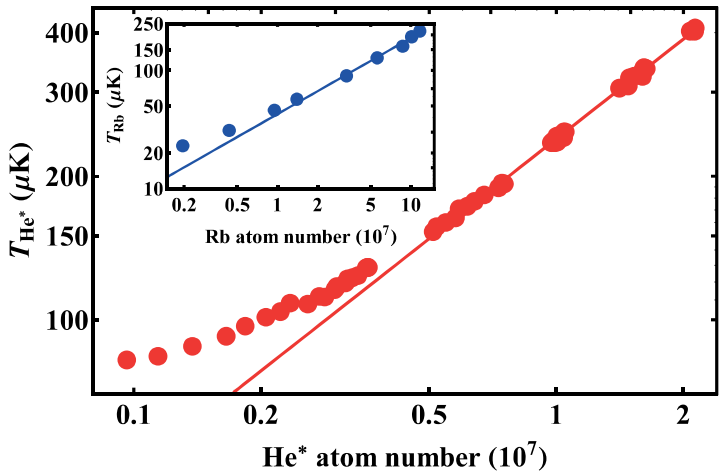

Figure 4.3: He* (red circles) and Rb (inset) temperatures as function of atom number during the evaporative cooling in the QMT. Solid lines are double-logarithmic fits that include only the first few points indicating the efficiency of the evaporation process. Data are measured in a single-species experiment.

in 1 s. We typically transfer about 30 to 40% of the atoms of both species from the 3D-MOT into the magnetic trap. Since sympathetic cooling is not efficient due to the small interspecies scattering length and large mass ratio [87, 88], we perform simultaneous MW-induced (Rb) and RF-induced (He*) forced evaporative cooling in the QMT. To generate the MW frequencies, we use a 6.8 GHz phase-locked oscillator (Amplus PLO) mixed with the frequency doubled output of a tunable 80 MHz signal generator. After a series of filtering and amplification stages, we send between 1 to 2 W of power to a MW horn. For the RF, we also use a tunable 80 MHz signal generator that is frequency doubled. We send around 5 W to an RF coil after a series of amplification stages.

The lowest temperature that can be achieved by evaporative cooling in a QMT is limited by Majorana loss and heating. The Majorana effect scales inversely with mass [9, 95] and is more pronounced for light atomic species such as He*. In Fig. 4.3, we show the measured temperature and number of atoms of He* and Rb during the evaporation process in the QMT. It is clear that the efficiency of the evaporative cooling for He* starts to go down at a much higher temperature (150 μK) as compared to the heavier Rb (below 50 μK). The data suggest that the lowest temperature that can be achieved for He*, while maintaining sufficient number of atoms, will be higher than for Rb. This temperature difference has to be taken into account

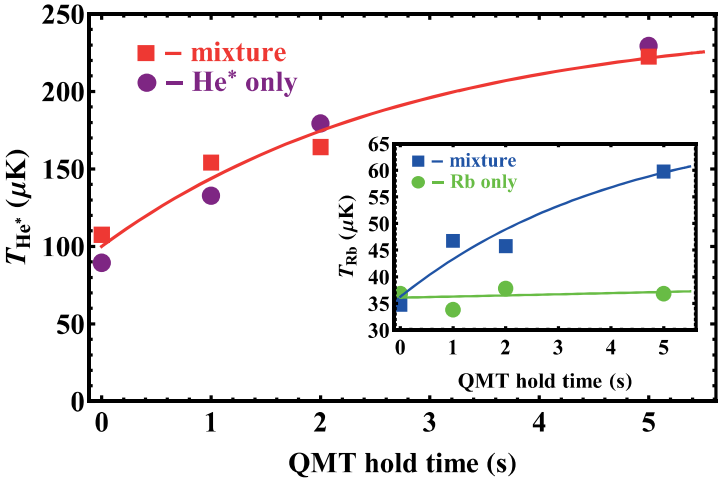

Figure 4.4: Time evolution of He* and Rb (inset) temperatures after the final stage of the evaporative cooling in the QMT. Solid lines are a guide to the eye. The increasing He* temperature is due to the Majorana heating. In the case of Rb, wherein the Majorana heating is still negligible (at least an order of magnitude slower than He* as exhibited in the green data), the temperature increase (blue data) is due to thermalization with the higher temperature He*.

during the simultaneous evaporative cooling because the overall efficiency of the evaporation process in the QMT will be affected by the interplay between the Majorana heating and interspecies thermalization. Generally, this means that we want to keep the temperatures of the two species as close as possible to minimize heating of Rb due to interspecies thermalization with the hotter He* atoms. An example of such a scenario is shown in Fig. 4.4. The increasing trend in the He* temperature is due to Majorana heating. There is no significant difference in the He* temperature with or without the presence of the Rb atoms. This is because Majorana heating dominates over the small effect of interspecies thermalization with Rb atoms. On the other hand, for the colder Rb sample wherein the Majorana effect is still small, the interspecies thermalization with hotter He* atoms dominates and causes a noticeable increase in the Rb temperature.

Other important issues to be considered during the simultaneous evaporation process are the MW and RF frequencies. The MW (between 6.8 GHz to 7.0 GHz) used for evaporative cooling of Rb will not affect the He* atoms in the magnetic trap, but the RF (160 MHz and lower) used for He* in principle can be in resonance with the Rb atoms. However, the Zeeman splitting of ^{4}He* is larger than that of ^{87}Rb (see Fig. 4.1), which is a general fea-

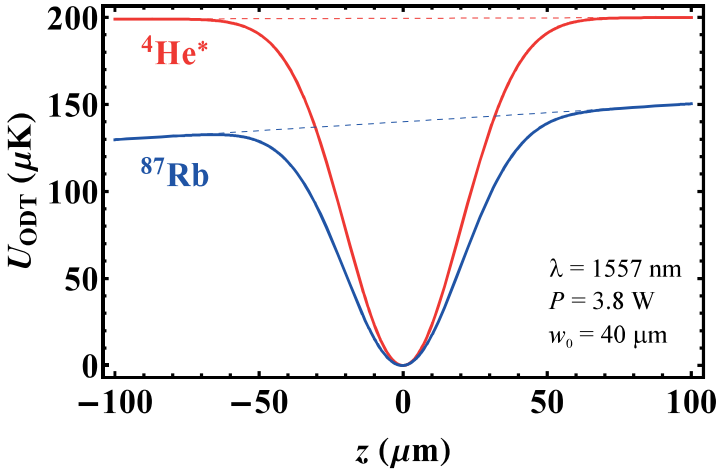

Figure 4.5: ODT trapping potentials along the radial (gravity) direction of He* (red) and Rb (blue). Note the asymmetry of the Rb potential due to gravity and the higher trap depth of He* due to the higher polarizability.

ture in He*+alkali mixtures. For Rb in the $|f = 2, m_f = +2\rangle$ state, the trap depth given by the RF is a factor of two larger than that for He*, and therefore RF can be selectively used for He*. The condition that the MW-truncated trap depth of Rb is lower than the RF-truncated one is given by: $\nu_{\mathrm{MW}} - \nu_{\mathrm{HFS}} < 3\nu_{\mathrm{RF}}$, where ν_{RF} and ν_{MW} are the RF and MW frequencies respectively, and ν_{HFS} is the hyperfine splitting of Rb. For the two species to have equal trap depths, the condition is $\nu_{\mathrm{MW}} - \nu_{\mathrm{HFS}} = 3\nu_{\mathrm{RF}}/2$.

During the initial transfer to the QMT, we send a fixed $\nu_{\mathrm{MW}} - \nu_{\mathrm{HFS}}$=125 MHz and ν_{RF}=140 MHz. After 4 s of thermalization and plain evaporation, we initiate forced evaporative cooling of the mixture. We use a total evaporation time of 8 s, in which we ramp down $\nu_{\mathrm{MW}} - \nu_{\mathrm{HFS}}$ to 13 MHz and ν_{RF} to 16 MHz. These values correspond to trap depths of 430 μK (Rb) and 800 μK (He*). At the end of the simultaneous evaporative cooling, we can have a few 10^6 atoms for both Rb and He* at temperatures of around 50 μK and 90 μK, respectively.

4.2.3 Transfer to single-beam ODT

Our ODT light has a wavelength $\lambda = 1557$ nm. A piezo-controlled mirror is used to precisely align the ODT beam with respect to the QMT center [107, 108]. The ratio in the polarizability of He* and Rb is 1.4 [110, 111]. With the available ODT power of around 4 W and a waist of 40 μm, the corresponding trap depths are around 200 μK (He*) and 140 μK (Rb), respectively. In Fig. 4.5, we show the ODT potentials of ^{4}He* and ^{87}Rb for an ODT power of

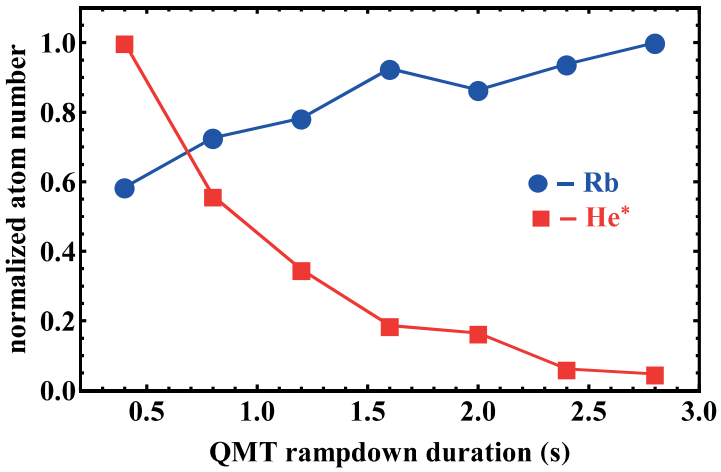

Figure 4.6: Normalized atom number showing the loading of He* (red) and Rb (blue) into the ODT as a function of the QMT ramp down duration. Solid lines are a guide to the eye.

3.8 W. The effect of gravity is noticeable for Rb by the asymmetry of the trapping potential, leading to a slight reduction of the trap depth. At low ODT powers, the differential gravitational sag will lead to a separation of the two clouds. Here, we stay at a high ODT power at which this effect is negligible.

After evaporative cooling in the QMT, the mixture is transferred to a hybrid trap (HT) by ramping down the gradient of the QMT to the levitation gradient (0.33 G/cm) of ^{4}He* [108]. Here, we only use the HT as a bridging stage to facilitate the transfer to the pure ODT. Loading the mixture into the HT or ODT is not as straightforward as in our single-species experiment [107, 108]. The difference in the initial conditions, such as temperature and density, and the different properties such as mass and polarizability imply different loading conditions. Most of these parameters are coupled and difficult to disentangle and investigate individually. Here, we focus on parameters that are crucial in the simultaneous loading and can be tuned in the loading scheme. In Fig. 4.6, we show the number of atoms loaded in the ODT as a function of the duration of QMT gradient ramp down, comparing Rb and He*. There is a clear difference in the duration for optimum loading between the two atomic species. Ideally, loading should be slow enough (adiabatic transfer), such that the atoms can smoothly follow the transition from the QMT to the ODT potential, as in the case of Rb, where the optimum transfer is toward longer duration. This is not surprising because we load Rb at a temperature that is much lower than the ODT

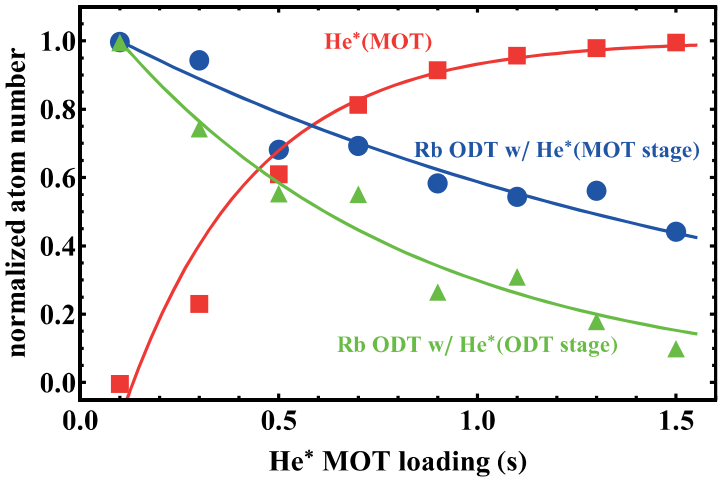

Figure 4.7: Rb atoms loaded in the ODT as a function of He* MOT loading time, comparing two situations. First is with He* atoms loaded up to the MOT stage (blue circles). Second is with He* atoms loaded up to the ODT stage (green triangles). The corresponding He* atoms during MOT loading is also shown (red squares). Solid lines are a guide to the eye.

trap depth. In fact, from our single-species experiment, we already observe a saturation in the loading of Rb above 2.5 W [107]. In the case of He*, the optimum transfer appears to be at a shorter duration of the QMT ramp down. A plausible explanation is because the temperature (limited by the Majorana effect) at which we load He* is just about half of the ODT trap depth. Correspondingly, from the single-species experiment we do not see a clear sign of saturation in the loading [108]. Furthermore, during the QMT ramp down, the He* cloud expands much faster than Rb due to the higher temperature and smaller mass. Here, we hypothesize that the geometrical size of the cloud with respect to the geometry of the ODT potential has a mismatch, limiting to short duration for the QMT ramp down in the case of He*. On an absolute scale, we generally observe that the transfer efficiency for Rb is higher than for He*. In future experiments, this can be improved by using higher ODT powers at which the He* loading can be also saturated.

More general, aside from the small interspecies loss in the MOT stage, there are no additional losses for He* as long the mixture stays in the doubly spin-stretched spin-state. For Rb, this is not the case particularly during the evaporative cooling in the QMT wherein the He* atoms can be a heat load for the Rb atoms as already discussed in Section 4.2.2. Additionally, the flux of ground state He that made it to the main chamber during the MOT loading also introduces additional loss for the Rb atoms. These issues

are summarized in Fig. 4.7, where we plot the number of Rb atoms loaded in the ODT as a function of He* MOT loading time. For the blue circles, the He* atoms are only introduced up to the MOT stage. Out of the total 50% loss in the number of Rb atoms in the ODT, around 20% can be accounted from the MOT stage (for a fully loaded He*) while the remaining 30% can be explained due to background collisions during the QMT stage and transfer to the ODT. For the green triangles, the He* atoms are present up to the ODT stage. The additional loss in the number of Rb atoms is due to heating from the hotter He* atoms during the simultaneous evaporative cooling in the QMT. Together with the QMT ramp down duration, we use the He* MOT loading to tune the ratio in the atom numbers of He* and Rb in the ODT. In our mixture experiment, we typically load He* in the 3D-MOT between 0.4 s to 0.8 s while the QMT ramp down duration is between 0.5 s to 2 s. We can tune between (0.2-1)$\times 10^5$ atoms for Rb and He* at temperatures around 15 μK (Rb) and 22 μK (He*).

4.2.4 Dual absorption imaging and MCP detection

Standard absorption imaging is used to measure the atom number and temperature of the samples (see Chapter 2 for the details about the cameras used and the geometry of the imaging beams). Absorption imaging of the two species can be done simultaneously. This is essential, especially during the optimization process, in which we can easily track the positions of the two clouds when aligning the 3D-MOT beams to optimize the OM stage and the subsequent transfer of the mixture to the QMT.

Additionally for He*, we also use a microchannel plate (MCP) detector that is positioned below the trap center (at angle 22° with respect to the direction of gravity) to measure the time-of-flight (TOF) distribution. A magnetic gradient pulse from a single deflection coil is applied to direct the atoms onto the MCP detector [108]. TOF signals of He* can also be obtained simultaneously with Rb imaging. After the clouds are released from the ODT, we first capture the images using ballistic expansions typically between 1 to 5 ms after which we apply the magnetic gradient pulse.

Our experiments involve mixtures of different spin-state combinations, for which state-selective detection is essential. In the case of our MCP TOF detection, the orientation of the deflection coil and the MCP position will already suffice for the purpose. In principle, we can only detect He* atoms in the $|m_s = +1\rangle$ state. To detect atoms in the $|m_s = -1\rangle$ state, we apply an RF sweep that transfers back the atoms to the $|m_s = +1\rangle$ state. For Rb, we use the repumping light during imaging to distinguish atoms between the two hyperfine states $|f = 2, m_f = +2\rangle$ and $|f = 1, m_f = +1\rangle$.

4.2.5 Preparation of different spin-states

To prepare a mixture of different spin-state combinations in the optical dipole trap, we perform rapid adiabatic transfer (see Chapter 2 for a detailed discussion) around a magnetic field of 2.5 G. For He*, a 0.5 MHz RF sweep is applied to transfer the atoms between the Zeeman states. A 25 ms RF sweep of around 1 W transfers all of the atoms from the $|m_s = +1\rangle$ to $|m_s = -1\rangle$ state. We confirm the transfer by applying a second sweep that transfers back the atoms to the $|m_s = +1\rangle$. For Rb, a 70 ms MW sweep of 0.2 MHz is used to transfer the atoms from the hyperfine state $|f = 2, m_f = +2\rangle$ to $|f = 1, m_f = +1\rangle$. However, we only manage to transfer 50% of the atoms to the $|f = 1, m_f = +1\rangle$, due to limited MW power. We immediately send resonant light for 15 ms to clean the remaining atoms in the $|f = 2, m_f = +2\rangle$. Among the various possible combinations, we work with $|m_s = -1\rangle + |f = 2, m_f = +2\rangle$ (single RF sweep on He*), $|m_s = +1\rangle + |f = 1, m_f = +1\rangle$ (single MW sweep on Rb) and $|m_s = -1\rangle + |f = 1, m_f = +1\rangle$ (MW sweep on Rb followed by RF sweep on He*). For the given magnetic field, the RF sweep used for He* does not affect the Rb atoms following a similar argument as described earlier in Section 4.2.2.

4.3 Lifetimes in optical dipole trap

For measurements of trapping lifetimes, we ramp down the QMT gradient in 2 s to allow for a smooth (and adiabatic) transfer. Afterward, we hold the mixture in the ODT for 2.5 s to ensure thermalization of each species before preparing a particular spin-state combination. We need to measure the initial temperatures of both species because the interspecies thermalization rate (0.01 s^{-1}) is absent on the experimentally relevant time scales. In here, we can assume a constant temperature of each species during lifetime measurements. We hold the mixture in the ODT for a variable time and measure the remaining atoms in the trap. We can measure both the remaining Rb and He* atoms simultaneously from the absorption imaging (Rb) and MCP TOF detection (He*). However, the signal-to-noise ratio from MCP detection is better than from absorption imaging. In this regard, our analysis of trap loss is based mostly on He* MCP data and we only use the Rb data as a counter-check [152].

We measure a long trapping lifetime for the doubly spin-stretched spin-state $|m_s = +1\rangle + |f = 2, m_f = +2\rangle$ mixture (see Fig. 4.8, black circles). We observe short lifetimes of a second to a few seconds for the other spin-state combinations, for which Penning ionization is spin-allowed. An example is also shown in Fig. 4.8 (red circles) for the case of $|m_s = -1\rangle + |f = 1, m_f = +1\rangle$.

To extract the interspecies two-body loss rates L_2 of the different spin-state combinations, we fit the trap loss data with the numerical solution of

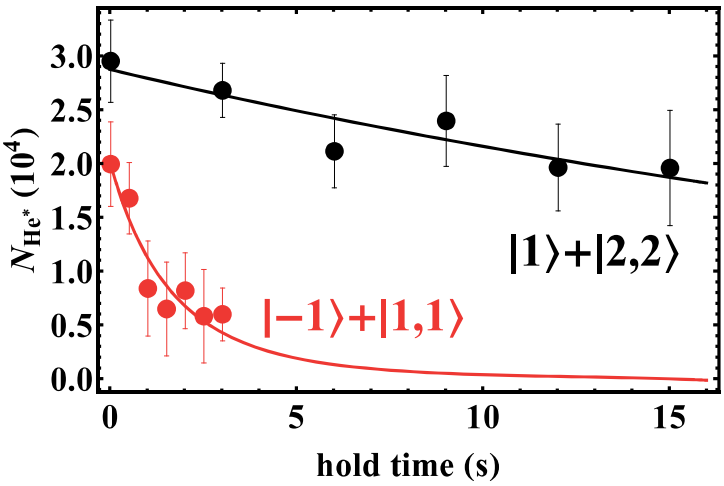

Figure 4.8: Remaining He* atoms in the ODT as a function of hold time showing the stable spin-state combination $|m_s = +1\rangle + |f = 2, m_f = +2\rangle$ (black) and the shorter lifetime spin-state combination $|m_s = -1\rangle + |f = 1, m_f = +1\rangle$ (red). The initial Rb atom numbers are $N_{\mathrm{Rb}} = (8.6 \pm 0.7) \times 10^4$ for $|m_s = +1\rangle + |f = 2, m_f = +2\rangle$ and $N_{\mathrm{Rb}} = (4.5 \pm 0.8) \times 10^4$ for $|m_s = -1\rangle + |f = 1, m_f = +1\rangle$. The approximately factor two difference in the initial Rb number is due to the MW transfer efficiency. Solid lines are numerical fit from the solution of Eq. 4.2, from which the two-body loss rates are obtained.

the two coupled equations,

$$\frac{d}{dt}N_{\mathrm{i}} = -\Gamma_{\mathrm{i}}N_{\mathrm{i}} - L_2 \int n_{\mathrm{i}}(\vec{r})n_{\mathrm{j}}(\vec{r})d\vec{r}, \tag{4.2}$$

where i or j can be assigned interchangeably to He* or Rb, N is the atom number, Γ is the one-body loss rate, $n(\vec{r}) = n_0 \exp[-U(\vec{r})/k_BT]$ is the density, $n_0 = N/\int \exp[-U(\vec{r})/k_BT]d\vec{r}$ is the peak density and $U(\vec{r})$ is the trapping potential wherein the contribution due to gravity is included. The one-body loss rates Γ are measured independently. Intraspecies two- and three-body loss processes, including homonuclear Penning ionization, can be fully neglected for the chosen spin-states under our conditions [153–155].

For the loss rate in the stable $|m_s = +1\rangle + |f = 2, m_f = +2\rangle$ mixture, we do not observe a significant difference compared to the single-species measurement, which suggests that it is only limited by background collisions. We obtain an upper limit in the total two-body loss rate, $L_2 = 1.3 \times 10^{-12}\mathrm{cm}^3\mathrm{s}^{-1}$, similar as previous upper limits obtained from magnetic trap experiments [88, 92].

For the other spin-state combinations, we obtain relatively large L_2 co-

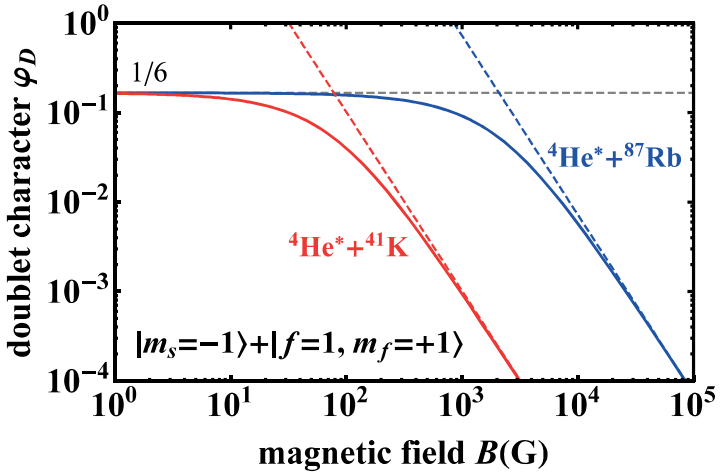

Figure 4.9: Doublet character φ_D as function of magnetic field for the energetically lowest spin-state combination $|m_s = -1\rangle + |f = 1, m_f = +1\rangle$, comparing ^{4}He*+^{87}Rb (blue) and ^{4}He*+^{41}K (red). Horizontal dashed line corresponds to $\varphi_D = 1/6$ and the dashed colored lines give the asymptotic B^{-2} dependence.

efficients on the order of $10^{-11} - 10^{-10}$cm^{3}s^{-1} [152]. For the energetically lowest spin-state combination $|m_s = -1\rangle + |f = 1, m_f = +1\rangle$, for which Penning ionization is the only possible two-body loss process, we obtain $L_2 = 5.3^{+2.0}_{-1.7} \times 10^{-11}$cm^{3}s^{-1}. This value is not far from the universal rate constant $L_2 = 4.5 \times 10^{-10}$cm^{3}s^{-1} [156], if one takes into account an additional factor that represent the amount of doublet character (φ_D), of the particular spin-state combination, which at small magnetic fields is 1/6 in this case. This observation suggests that at high magnetic fields, where for this spin-state combination φ_D goes to zero, two-body loss will be reduced. The magnetic field dependence of φ_D is given in Fig. 4.9, showing the case of ^{87}Rb and ^{41}K. The transition from a constant $\varphi_D = 1/6$ to a decreasing $\varphi_D \sim B^{-2}$ occurs at a magnetic field that scales with the hyperfine splitting. Thus, while this effect occurs for ^{87}Rb at rather high magnetic fields, for ^{41}K, which has the lowest hyperfine splitting of 254 MHz, this effect can be observed at experimentally feasible magnetic fields.

4.4 Conclusions and prospects

In conclusion, we have realized an ultracold, optically trapped mixture of ^{87}Rb and ^{4}He* atoms. We have demonstrated simultaneous RF-induced (He*) and MW-induced (Rb) forced evaporative cooling in the quadrupole

magnetic trap. We have measured a long trapping lifetime for the doubly spin-stretched spin-state combination exhibiting a strong suppression of Penning ionization loss. Realizing a dual-species BEC is in principle possible using this spin-state combination. Here, it is crucial to compensate (or control) the differential gravitational sag that leads to separation of the two clouds due to the huge mass ratio between Rb and He*. Among the possible solutions are the application of special optical dipole trap geometries that allow for strong vertical confinement in a shallow trap (see e. g. [133]), or the addition of an optical dipole beam that selectively supports the heavy species [157]. Another approach is to add a magnetic field gradient that will provide an additional species-dependent force [158].

Realizing a BEC of ^{87}Rb or ^{4}He* in a single-species preparation is relatively straightforward using our existing hybrid trap or single-beam ODT scheme [107, 108]. However for the mixture preparation, constraints as outlined in this chapter limit the transfer efficiency (and thus the initial phase-space density: at least an order of magnitude smaller compared to our single-species preparation) into the hybrid trap or single-beam ODT. The main issue is the Majorana effect that limits the lowest achievable temperature for He* in the magnetic trap. This is not a fundamental limit but rather an experimental consequence of using a QMT, and not present in an Ioffe-Pritchard type of magnetic trap. Another approach is to use higher ODT powers that provide higher trap depths, such that it is not necessary to push the evaporative cooling towards lower temperature in the QMT [130]. For the case of Rb and He*, we estimate that an ODT power of around 10 W will already provide sufficient transfer (a few 10^6 atoms at temperatures below 30 μK) in the HT or single-beam ODT for evaporative cooling towards dual quantum degeneracy.

Using an analogous experimental scheme as described in this chapter (i.e. simultaneous MW (alkali) and RF (He*) evaporative cooling), ultracold bosonic ^{4}He* and bosonic alkali mixtures all seem possible. For the fermionic alkali atoms, the cooling strategy will rely on sympathetic cooling with ^{4}He* and thus depend on a favorable interspecies quartet scattering length [87]. Similarly, for fermionic ^{3}He* and bosonic alkali mixtures, realizing two-species quantum degeneracy also depends on the quartet scattering length. In here, ^{4}He* can also be introduced to sympathetically cool ^{3}He* [36]. Finally, for ^{3}He* and fermionic alkali mixtures, sympathetic cooling with a third species is required which can either be ^{4}He* or another bosonic alkali with favorable quartet scattering length.

Feshbach resonances are in principle possible due to the hyperfine coupling between the doublet and quartet interaction potentials. This requires a mixture in a spin-state combination other than the purely quartet doubly spin-stretched spin-state and is thus accompanied by strong two-body loss, which limits the scattering length tunability around the Feshbach resonance [159] and the observation of (enhanced) three-body recombination loss. Still,

Feshbach spectroscopy can be performed, as we expect a modification of the Penning ionization loss rate around the Feshbach resonances due to coupling between the doublet and quartet interaction potentials.

Chapter 5

Quantum-state-controlled Penning-ionization reactions between ultracold alkali and metastable helium atoms

This chapter is based upon: A.S. Flores, W. Vassen and S. Knoop. "Quantum-state-controlled Penning-ionization reactions between ultracold alkali-metal and metastable helium atoms." *Physical Review A* 94, 050701(R), 2016.

509242-L-bw-Flores
Processed on: 3-4-2017

Abstract

In an ultracold, optically trapped mixture of ^{87}Rb and metastable triplet ^{4}He atoms we have studied trap loss for different spin-state combinations, for which interspecies Penning ionization is the main two-body loss process. We observe long trapping lifetimes for the purely quartet spin-state combination, indicating strong suppression of Penning ionization loss by at least two orders of magnitude. For the other spin-mixtures we observe short lifetimes that depend linearly on the doublet character of the entrance channel. We compare the extracted loss rate coefficient with recent predictions of multichannel quantum-defect theory for reactive collisions involving a strong exothermic loss channel and find near-universal loss for doublet scattering. Our work demonstrates control of Penning ionization reactive collisions by internal atomic state preparation.

5.1 Introduction

Ultracold inelastic and reactive collisions are important processes in atomic and molecular samples [160, 161], determining their trapping lifetimes and the success of evaporative and sympathetic cooling. Conversely, measurements of these lifetimes reveal the rate coefficients of the dominant inelastic or reactive collision processes, opening the fields of ultracold few-body physics [43, 162] and ultracold chemistry [163, 164]. The ultracold regime offers exquisite control over the initial internal and external quantum states, and the possibility to experimentally control collision properties or even steer chemical reactions with external fields [165].

Understanding of inelastic and reactive collisions is in general very difficult due to the many degrees of freedom involved. This has motivated recent work based on multichannel quantum-defect theory (MQDT) [156, 166, 167], in which analytic expressions of collision rates were derived in the case of a strong exothermic reactive channel. In particular, if the probability of an inelastic or reactive process in the short-range part of the collision is 100%, i. e. if $P^{\mathrm{re}} = 1$, theory predicts universal rate constants that only depend on the reduced mass of the collision partners and the leading long-range coefficient [156, 166], independent of the complicated short-range dynamics. If the reaction probability is less than 100% ($P^{\mathrm{re}} < 1$), still only two parameters are required to include the (non-universal) short-range physics, i. e. the scattering length a and P^{re} [167]. These analytical models have been applied to atom-exchange reactions between ground state KRb molecules below 1 μK [156, 163], and Penning ionization reactions between argon and helium atoms in the metastable triplet 2 ^{3}S$_1$ state (He*) in merged-beam experiments from 10 mK up to 30 K [167, 168].

In this chapter, we study ultracold Penning ionizing collisions between

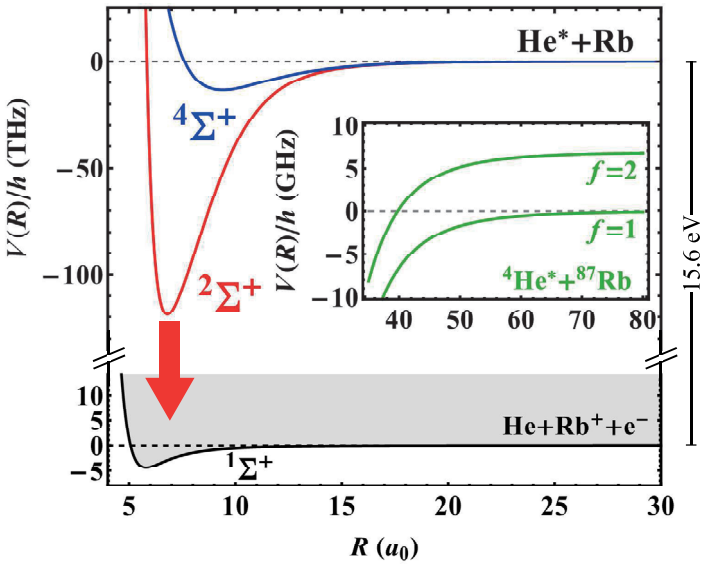

Figure 5.1: Potential energy curves of the $^2\Sigma^+$ [89] and $^4\Sigma^+$ [88] states of the He*Rb molecule that correlate with the He*+Rb atomic asymptote, and the $^1\Sigma^+$ [169] state of the $HeRb^+$ molecule that correlates with the He+Rb^++e^- asymptote, which lies 15.6 eV lower and forms the Penning ionization continuum (where the internuclear distance R is given in Bohr radii, $a_0 = 0.05292$ nm). The inset shows the long-range adiabatic potentials of ^{4}He*^{87}Rb near its dissociation threshold, including the hyperfine splitting of ^{87}Rb.

He* atoms (internal energy 19.8 eV) and alkali atoms A in their electronic ground state:

$$\mathrm{He}(2\,^3\mathrm{S}_1) + \mathrm{A}(^2\mathrm{S}_{1/2}) \rightarrow \mathrm{He}(1\,^1\mathrm{S}_0) + \mathrm{A}^+(^1\mathrm{S}_0) + \mathrm{e}^-, \tag{5.1}$$

which are described by two interaction potentials, doublet $^2\Sigma^+$ and quartet $^4\Sigma^+$, and a strongly exothermic Penning ionization (PI) reaction channel (see Fig. 5.1 for the specific case of He*+Rb). The description of the PI loss rate in terms of MQDT would require at least four parameters, namely the scattering lengths and the reaction probabilities of both doublet and quartet potentials. However, PI from the $^4\Sigma^+$ potential is spin-forbidden, because the total electron spin in the PI channel is only 1/2 (see Eq. 5.1). Thus PI proceeds predominantly via the doublet $^2\Sigma^+$ potential. Therefore one expects the PI loss rate to be determined by the $^2\Sigma^+$ potential only, however, including an additional factor that takes into account the doublet character of the particular entrance channel. This makes the PI loss rate experimentally controllable by internal atomic state preparation and magnetic field.

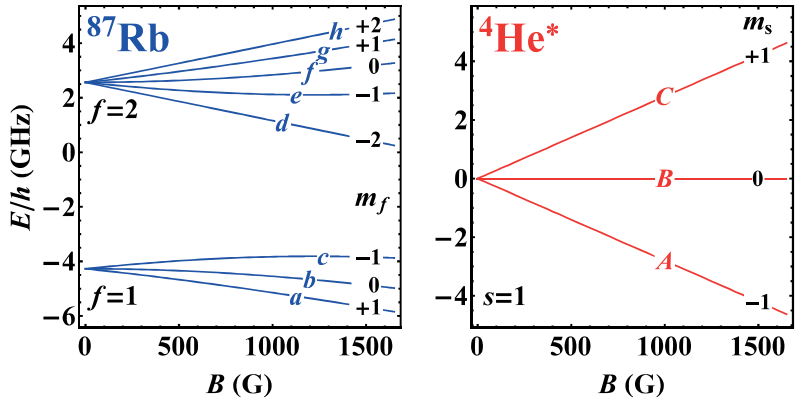

Figure 5.2: Magnetic field dependence of the atomic ground-state energies of ^{87}Rb and ^{4}He*, indicating the labeling of the different internal states as used throughout the chapter.

We have realized an ultracold mixture of ^{4}He* and ^{87}Rb in an optical dipole trap (ODT), and performed lifetime measurements for different spin-state combinations (the labeling of the atomic spin-states is shown in Fig. 5.2, $(a-h)$ for ^{87}Rb and $(A-C)$ for ^{4}He*). ODTs provide spin-independent confinement, applicable to both low- and high-field seeking spin-states, which allows direct comparison between trap losses of different spin-mixtures. Previous experimental studies of He*+alkali collisions have been performed at thermal energies in stationary afterglow and merged-beam experiments (see e. g. [89, 90]). Simultaneous laser cooling and trapping of ^{4}He* and ^{87}Rb was first demonstrated by the Truscott group [91]. Magnetic trapping of the $h+C$ spin-state combination, which is purely quartet, provided upper limits of the PI rate on the order of 10^{-12} cm^{3}s^{-1} for pure quartet scattering [88, 92], and revealed a small quartet scattering length a_Q [88], in agreement with *ab initio* calculations of the quartet $^{4}\Sigma^{+}$ potential [87, 88]. In contrast, the knowledge on the doublet $^{2}\Sigma^{+}$ potential is limited [89], and the doublet scattering length a_D is unknown.

5.2 Experiment

Starting point of our measurements is an ultracold mixture of 3×10^{4} ^{4}He* and 9×10^{4} ^{87}Rb atoms in a single-beam ODT at a temperature of 22 and 15 μK, respectively. A detailed description of the experimental setup used in this measurement is presented in Chapter 4. We apply simultaneous RF- and MW-forced evaporative cooling in the QMT for He* and Rb, respectively, before transfer to the single-beam ODT, which has a waist of 40 μm and a wavelength of 1557 nm. We use a fixed ODT power of 3.8 W, corresponding

to an effective trap depth of 200 and 140 μK for He* and Rb, respectively [1].

Throughout the preparation stages in the QMT and ODT we use the stable $h + C$ spin-state combination [88]. To prepare other spin-mixtures we transfer ^{87}Rb from h to a and/or ^{4}He* from C to A, by single adiabatic MW and RF frequency sweeps, respectively, at a bias magnetic field of 2.5 G. While our RF transfer has a 100% efficiency, our MW transfer is only 50% due to limited MW power. We remove the non-transferred Rb atoms in state h with resonant light immediately after the MW sweep. After a variable hold time we switch off the ODT and simultaneously measure the number of atoms by using standard absorption imaging for Rb and microchannel plate (MCP) detection for He* [85].

5.3 Interspecies two-body loss rate

We obtain the interspecies Penning ionization loss rate coefficients by measuring the time-evolution of the number of He* atoms, and fit the solution of two coupled equations:

$$\dot{N}_i = -\Gamma_i N_i - L_2 \int n_i(\vec{r}) n_j(\vec{r}) \mathrm{d}\vec{r} \tag{5.2}$$

where (i, j) is (He*, Rb), L_2 is the total interspecies two-body loss rate coefficient, N_i and $n_i(\vec{r})$ are the atom number and density profile for species i. Intraspecies two- and three-body loss processes [153–155] can be fully neglected for the chosen spin-states under our conditions. We only fit the time-evolution of He*, using the measured initial Rb atom number, because of the higher sensitivity being the minority species and the better signal-to-noise of the He* MCP detection compared to the absorption imaging of Rb. The density profiles are calculated numerically, using measured temperatures T_i, via $n_i(\vec{r}) = n_i^0 \exp\left[-U_i(\vec{r})/k_B T_i\right]$, where $U_i(\vec{r})$ is the trapping potential, including gravity, and $n_i^0 = N_i / \int \exp\left[-U_i(\vec{r})/k_B T_i\right] \mathrm{d}\vec{r}$ is the peak density. In our case the vertical confinement is strong enough such that the reduction of the overlap between the two clouds due to the differential gravitational sag is negligible. Single-species lifetimes are measured to determine the one-body loss rates Γ_i.

In Fig. 5.3 we present our lifetime measurements (at the bias magnetic field of 2.5 G), showing the time-evolution of the He* atom number of the different spin-mixtures. We observe a long trapping lifetime for the purely quartet h+C spin-combination, which we cannot distinguish from the single-species lifetimes. This means that the trapping lifetime is fully dominated

[1] The polarizability of He* is 1.4 times larger than Rb at a wavelength of 1557 nm [110, 111], while at our ODT power gravity gives a 5% reduction on the Rb trap depth (which for He* is well below 1%). The interspecies thermalization rate is small (0.01 s^{-1}) due to the small interspecies scattering length [88] and the large mass ratio, and only intraspecies thermalization takes place (for which the rate is about 1 s^{-1} for both species).

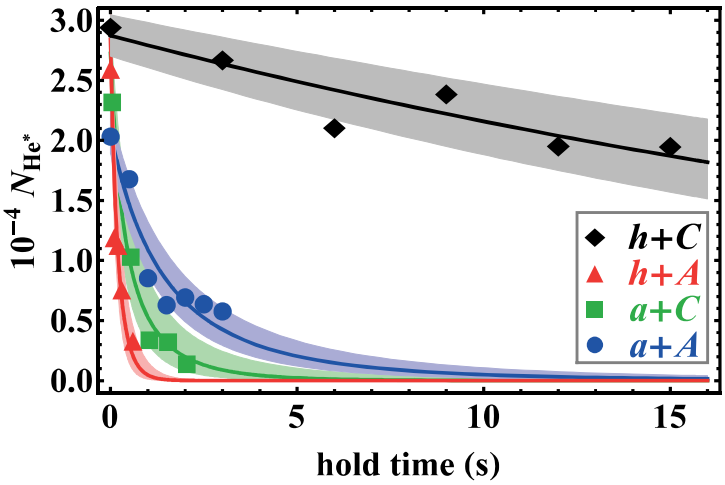

Figure 5.3: Time-evolution of the number of He* atoms for different spin-mixtures. The displayed data represent an average over several experimental runs (3-6). The solid lines are fits of Eq. 5.2 to all the data. The colored bands around the lines indicate the standard error of the fit. The initial Rb atom numbers are: $h + A$ and $h + C$: $N_{\mathrm{Rb}} = (8.6 \pm 0.7) \times 10^4$; $a + A$: $N_{\mathrm{Rb}} = (4.5 \pm 0.8) \times 10^4$; $a + C$: $N_{\mathrm{Rb}} = (3.9 \pm 0.6) \times 10^4$.

by one-body loss and we can only obtain an upper limit of the two-body loss rate, namely 1.3×10^{-12} cm^{3}s^{-1}. Together with our knowledge of a_Q [88], we obtain a constraint on the reaction probability for the quartet $^4\Sigma^+$ potential of $P^{\mathrm{re}} < 0.01$, using Eq. 5.5 below. We expect the actual quartet PI loss rate to be on the order of 10^{-14} cm^{3}s^{-1}, on basis of the suppression of PI in homonuclear He* collisions [85] and the similar s character of the valence electron of He* and alkali atoms. In the following we simply neglect the quartet contribution to the PI loss.

For the $h + A$, $a + C$ and $a + A$ spin-mixtures we observe orders of magnitude faster losses, and especially for the $h+A$ and $a+C$ spin-mixtures the He* sample is depleted within a few seconds. Here one should note the approximately factor of two difference in initial Rb atom numbers between the $h + A$ mixture and the $a + A$ and $a + C$ mixtures, mainly due to the MW transfer efficiency. We obtain the two-body loss rate coefficients L_2 by fitting Eq. 5.2 to the data, and the results are shown in Fig. 5.4. The error bars contain the fit error and uncertainty in the initial Rb atom number, as well as the uncertainty in the temperatures, which are required to calculate the density profile.

We analyze our data in terms of the doublet character φ_D, which represents the amount of doublet scattering. Provided that PI is the dominant

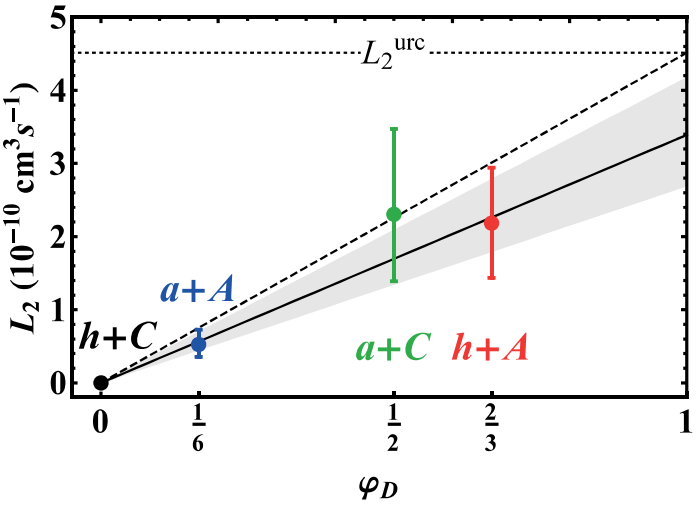

Figure 5.4: Compilation of measured two-body loss rates L_2, sorted by the corresponding doublet character φ_D, and comparison with the universal loss rate L_2^{urc} (dotted line) via $L_2 = \varphi_D L_2^{\mathrm{urc}}$ (dashed line). The solid line is a linear fit through the data points (and its colored band indicates the standard error of the fit). See Appendix D for an overview of the different loss rates.

loss process, we expect the loss rate to scale linearly with φ_D,

$$L_2 = \varphi_D L_2^{\mathrm{PI}}, \tag{5.3}$$

where L_2^{PI} is the loss rate due to PI for pure doublet scattering. φ_D is obtained by expanding the long-range atomic product states on to the short-range doublet molecular state (see Appendix A). In the limit of low magnetic fields, i. e. $B << E_{\mathrm{HFS}}/4\mu_B$ (where E_{HFS} is the alkali hyperfine splitting and μ_B is the Bohr magneton), and the case of an alkali atom with nuclear spin of 3/2, φ_D takes values of $q/6$, where q is an integer number between 0 and 4. The value of φ_D for the different spin-state combinations is indicated in Fig. 5.4. Fitting Eq. 5.3 to our data gives $L_2^{\mathrm{PI}} = 3.4^{+0.8}_{-0.7} \times 10^{-10}$ cm^{3}s^{-1} for Penning ionization loss via the doublet potential.

In general the doublet character φ_D is magnetic field dependent, and therefore also the loss rate. For instance, for the energetically lowest spin-channel $a+A$, φ_D becomes significantly less than 1/6 when $B \sim E_{\mathrm{HFS}}/4\mu_B$, and $\varphi_D \to 0$ as B^{-2} for $B >> E_{\mathrm{HFS}}/4\mu_B$ (see Appendix A). While for ^{87}Rb this behavior occurs at rather high magnetic fields ($E_{\mathrm{HFS}}/4\mu_B = 1.2$ kG), due to the large E_{HFS}, for an alkali atom with a small E_{HFS}, like ^{41}K, this effect takes place within an experimentally accessible range of magnetic fields ($E_{\mathrm{HFS}}/4\mu_B = 45$ G). This provides interesting prospects for realizing stable

ultracold mixtures in a variety of spin-state combinations, and the application of Feshbach resonances to tune the scattering length, which requires small two-body losses [159].

5.4 Comparison with multichannel quantum-defect theory

We compare the obtained value of L_2^{PI} with analytic expressions from MQDT. For the universal case, $P^{\mathrm{re}} = 1$, the zero-temperature limit universal loss rate is given by [156, 166]:

$$L_2^{\mathrm{urc}} = 2\frac{h}{\mu}\bar{a} \tag{5.4}$$

where $\bar{a} = 0.478\ldots\left(2\mu C_6/\hbar^2\right)^{1/4}$ is the so-called mean scattering length that solely depends on the reduced mass μ and the leading long-range van der Waals coefficient C_6. For He*+Rb $C_6 = 3858$ a.u. [88], resulting for ^{4}He*+^{87}Rb in $\bar{a} = 41a_0$ and $L_2^{\mathrm{urc}} = 4.5 \times 10^{-10}$ cm^{3}s^{-1}. In Fig. 5.4 L_2^{urc} and $\varphi_D L_2^{\mathrm{urc}}$ are shown as the dotted and dashed lines, respectively. Our extracted value of L_2^{PI} lies slightly below L_2^{urc}. However, taking into account a small finite temperature correction of 8% reduces the universal loss rate to 4.2×10^{-10} cm^{3}s^{-1} (see Appendix B), which is consistent with our L_2^{PI} and the reaction probability for PI in the doublet potential might be 100%.

Still, L_2^{PI} could also correspond to the non-universal case, $P^{\mathrm{re}} < 1$, where the zero-temperature limit loss rate is given by [167]:

$$L_2^{\mathrm{nurc}} = L_2^{\mathrm{urc}} y \frac{1 + (s-1)^2}{1 + y^2 (s-1)^2}, \tag{5.5}$$

where y is related to P^{re} via $P^{\mathrm{re}} = 4y/(1+y)^2$, and $s = a/\bar{a}$ is the rescaled scattering length, where a is the scattering length (here the doublet scattering length a_D). The combinations of P^{re} and s that matches L_2^{PI} are shown in Fig. 5.5 as the purple colored band (for which we have also included finite temperature corrections). A typical scattering length of $a \approx \bar{a}$, i. e. $s \approx 1$, would mean a high reaction probability of $P^{\mathrm{re}} \geq 0.94$. While for $P^{\mathrm{re}} = 1$ sensitivity to the scattering length is lost (and $L_2^{\mathrm{nurc}} = L_2^{\mathrm{urc}}$), a tiny reduction of less than 0.001 already results in a constraint on the possible scattering length range of about $0 \leq s \leq 2$. A match with a small reaction probability would require the less likely cases of either a large positive or large negative scattering length.

In principle, P^{re} can be calculated from the complex potential $U(r) = V(r) - (i/2)\Gamma(r)$ [170], where $\Gamma(r)$ represent the ionization width. For He*+alkali collisions *ab initio* calculations on the doublet potential $V(r)$ and corresponding $\Gamma(r)$ are available for Li, Na and K [148–151], from which

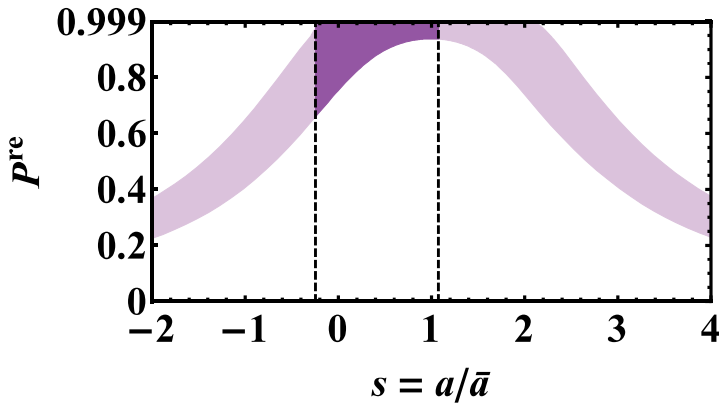

Figure 5.5: Comparison between the measured PI loss rate and the MQDT prediction for non-universal loss (Eq. 5.5 including finite temperature corrections), where the purple colored band represents the combinations of P^{re} and s that matches L_2^{PI}. The vertical dashed lines give the bounds on the scattering length from our analysis of hyperfine changing collisions, which constraints the possible combinations to the darker part of the purple colored band.

one can estimate $P^{\mathrm{re}} \approx 0.6 - 0.7$. For He*+Rb information on the doublet potential $V(r)$ is limited [89], while $\Gamma(r)$ is completely lacking. Stationary afterglow experiments at thermal energies [90] gave an anomalously large loss rate for Rb, compared to Na, K and Cs, and from this loss rate one estimates $P^{\mathrm{re}} \approx 1$ using the classical Gorin model [171] and assuming a statistical weight of 1/3 for doublet scattering. The presence of autoionizing Rb states close to the excitation energy of He* was suggested as a possible explanation of this anomaly [90], however, no fingerprint of these additional ionization channels was found in the electron emission spectrum [89]. *Ab initio* calculations of $V(r)$ and $\Gamma(r)$ are required to resolve this issue, however, it is probably safe to assume that $P^{\mathrm{re}} > 0.5$.

While for $a + A$ and $a + C$ PI is the only exothermic, spin-allowed two-body loss process, for $h + A$ hyperfine changing collisions (HCC) provide an additional two-body loss channel. However, comparing the loss rates for $a + C$ and $h + A$ suggests that the HCC contribution is small. By determining L_2^{PI} on basis of $a + A$ and $a + C$ only, and obtaining a lower limit of the PI contribution for $h + A$ via $\varphi_D L_2^{\mathrm{PI}}$, we derive an upper limit of HCC loss rate of 1.2×10^{-10} cm^{3}s^{-1}. According to the theory of ultracold spin-exchange collisions, as derived for hydrogen or alkali atoms, the HCC loss rate depends on the difference between the scattering lengths of the two interaction potentials. Applying the analytical result of Ref. [172] directly to He*+alkali collisions, with our HCC upper limit we derive that $|a_D -$

$a_Q| < 23a_0$ (see Appendix C). With our previously determined value $a_Q = 17(4)a_0$ [88], this would corresponds to $-10a_0 < a_D < 44a_0$. This constraint significantly reduces possible values of P^{re}, as indicated by the darker part of the purple colored band in Fig. 5.5. However, this analysis assumes that there is no influence of the PI channel on the HCC process, which may be too simplistic.

5.5 Conclusions

In conclusion, we have realized an ultracold, optically trapped mixture of ^{4}He* and ^{87}Rb atoms and obtained the two-body loss rate coefficients for four different spin-mixtures. We find long trapping lifetimes for the purely quartet spin-state combination, indicating a strong suppression of Penning ionization by at least two orders of magnitude, providing good prospects of realizing dual Bose-Einstein condensates. For the other spin-mixtures we observe short lifetimes that depend on the doublet character, which suggests suppression of Penning ionization at higher magnetic fields, experimentally feasible for alkali atoms with a small hyperfine splitting. We have compared our measured loss rates with recent predictions of MQDT for reactive collisions involving a strong exothermic loss channel. We observe near-universal loss for the doublet potential, and obtain a constraint on the unknown doublet scattering length.

Ultracold collisions between He* and alkali atoms can exhibit magnetically-induced Feshbach resonances [19] due to the hyperfine coupling between the doublet $^2\Sigma^+$ and quartet $^4\Sigma^+$ potentials. In combination with PI these atomic collision systems provide a relatively simple and experimentally feasible platform to study the effect of a strong exothermic loss channel on Feshbach resonances [159, 173], which may be important for evaporative and sympathetic cooling for molecules. Our analysis of the Penning ionization loss rate assumes no coupling between the doublet and quartet interaction potentials, which is corroborated by the observed linear dependence of the doublet character. However, around interspecies Feshbach resonances we expect a breakdown of this simple scaling, which opens the possibility of Feshbach spectroscopy despite strong two-body losses. More elaborate MQDT calculations [174] or numerical coupled-channel calculations using *ab initio* potentials are needed to investigate the behavior of the Penning ionization loss rate around these Feshbach resonances.

Appendix A: Doublet character

The doublet φ_D and quartet φ_Q character of the different spin-state combinations can be obtained by expanding the long-range atomic product states on to the short-range doublet and quartet molecular states, respectively. In

the low and high magnetic field limits, φ_S ($S = D$ or Q) is obtained by standard angular momentum algebra. In the following we consider the general case of a pair of atoms with electron spin s_a and nuclear spin i_a, and their respective projections m_{s_a} and m_{i_a}, where $a = (1, 2)$. The hyperfine quantum numbers and their projections are $f_a = s_a + i_a$ and $m_{f_a} = m_{s_a} + m_{i_a}$. The molecular electron spin is $S = s_1 + s_2$, and its projection $m_S = m_{s_1} + m_{s_2}$. For the case of He*+alkali atoms, $s_1 = 1$, $s_2 = 1/2$, and $S = 1/2$ (doublet potential) or $S = 3/2$ (quartet potential).

In the high magnetic field limit (Paschen-Back regime), $B >> E_{\rm HFS}/\mu_B$ (where $E_{\rm HFS}$ is the largest hyperfine splitting of the two atoms), the atomic states are labeled $|m_{s_1}, m_{i_1}; m_{s_2}, m_{i_2}\rangle$. They are projected on the molecular states via the following expansion:

$$|S, m_S\rangle = \sum_{m_{s_1}=-s_1}^{+s_1} \sum_{m_{s_2}=-s_2}^{+s_2} C^{S,m_S}_{s_1,m_{s_1};s_2,m_{s_2}} |s_1, m_{s_1}; s_2, m_{s_2}\rangle, \tag{5.6}$$

with Clebsch-Gordan coefficients

$$C^{S,m_S}_{s_1,m_{s_1};s_2,m_{s_2}} = (-1)^{-s_2+s_1-m_S} \sqrt{2S+1} \begin{pmatrix} s_1 & s_2 & S \\ m_{s_1} & m_{s_2} & -m_S \end{pmatrix}, \tag{5.7}$$

and the doublet and quartet character is simply given by

$$\varphi_S^{\rm PB}(m_{s_1}, m_{s_2}) = \sum_{m_S=-S}^{+S} \left| C^{S,m_S}_{s_1,m_{s_1};s_2,m_{s_2}} \right|^2, \tag{5.8}$$

independent of the nuclear spins. Therefore this result is the same for each He*+alkali combination, and $\varphi_D = 0$ in case $|m_{s_1} + m_{s_1}| = 3/2$, and $\varphi_D = 1/3$ or $2/3$ otherwise.

In the low magnetic field limit (Zeeman regime), $B << E_{\rm HFS}/\mu_B$ (where $E_{\rm HFS}$ is the smallest hyperfine splitting of the two atoms), the atomic states are labeled with the hyperfine quantum numbers, $|f_1, m_{f_1}; f_2, m_{f_2}\rangle$. For each atom the hyperfine states are given by:

$$|f, m_f\rangle = \sum_{m_s=-s}^{+s} \sum_{m_i=-i}^{+i} C^{f,m_f}_{s,m_s;i,m_i} |s, m_s; i, m_i\rangle, \tag{5.9}$$

involving the Clebsch-Gordan coefficients (Eq. 5.7). To obtain the characters first one has to project $|f_1, m_{f_1}; f_2, m_{f_2}\rangle$ states on to the $|s_1, m_{s_1}; s_2, m_{s_2}\rangle$ states, which are subsequently projected on the molecular states, as in Eq. 5.6. The final result is:

$$\varphi_S^{\rm ZR}(f_1, m_{f_1}; f_2, m_{f_2}) = \sum_{m_{s_1}=-s_1}^{+s_1} \sum_{m_{s_2}=-s_2}^{+s_2} \sum_{m_S=-S}^{+S} \left| C^{f_1,m_{f_1}}_{s_1,m_{s_1};i_1,m_{i_1}} C^{f_2,m_{f_2}}_{s_2,m_{s_2};i_2,m_{i_2}} C^{S,m_S}_{s_1,m_{s_1};s_2,m_{s_2}} \right|^2 \tag{5.10}$$

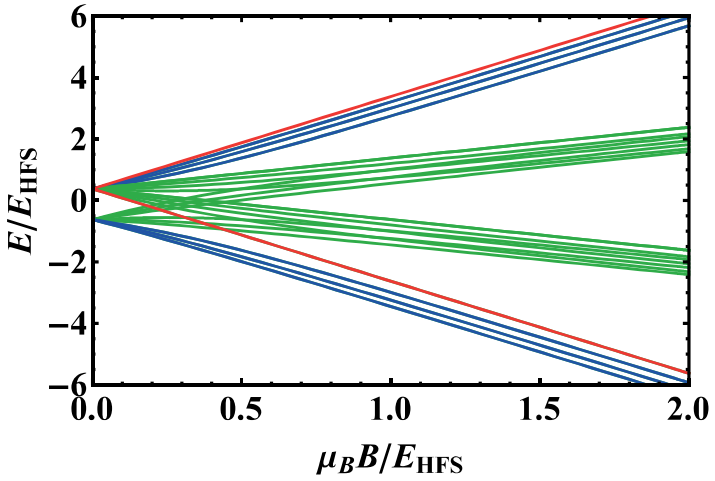

Figure 5.6: The energy spectrum of ^{4}He*+^{87}Rb. The blue lines indicate spin-state combinations for which $\varphi_D = 0$ in the limit of high magnetic fields, the green lines $\varphi_D = 1/3$ or $2/3$. The red lines are the two doubly spin-stretched state combinations, for which $\varphi_D = 0$ for each magnetic field.

with $m_{i_a} = m_{f_a} - m_{s_a}$. Here φ_S^{ZR} depends explicitly on i_1 and i_2, and therefore on the particular He* and alkali isotopes. In all cases, for the doubly spin-stretched state combination, $|f_1^{\max}, \pm f_1^{\max}; f_2^{\max}, \pm f_2^{\max}\rangle$, $\varphi_D = 0$.

In case of ^{4}He*, which has no nuclear spin (i. e. $i_1 = 0$), only m_{s_1} determines the spin-state of ^{4}He* and Eq. 5.10 is simplified to:

$$\varphi_S^{\mathrm{ZR},^4\mathrm{He}^*}(m_{s_1}; f_2, m_{f_2}) = \sum_{m_{s_2}=-s_2}^{+s_2} \sum_{m_S=-S}^{+S} \left| C^{f_2,m_{f_2}}_{s_2,m_{s_2};i_2,m_{i_2}} C^{S,m_S}_{s_1,m_{s_1};s_2,m_{s_2}} \right|^2 . \tag{5.11}$$

At intermediate magnetic fields the expansion of the $|f, m_f\rangle$ states in terms of $|s, m_s; i, m_i\rangle$ states is magnetic field dependent, and one has to numerically calculate the eigenvectors of the Hamiltonian that contains the hyperfine and Zeeman interactions.

The energy spectrum of ^{4}He*+^{87}Rb is shown in Fig. 5.6, which contains 24 atom pair states. The energy and magnetic field are rescaled with the hyperfine energy, such that the spectrum applies to all $i = 3/2$ alkali atoms (apart from a very small correction due to the nuclear g-factor). At high magnetic fields one recognizes four groups of states, corresponding to $m_S = -3/2, -1/2, 1/2, 3/2$. The outer two groups with $|m_S| = 3/2$ are purely quartet, while the inner two groups $|m_S| = 1/2$ have both doublet and quartet character. The blue lines indicate spin-state combinations for which

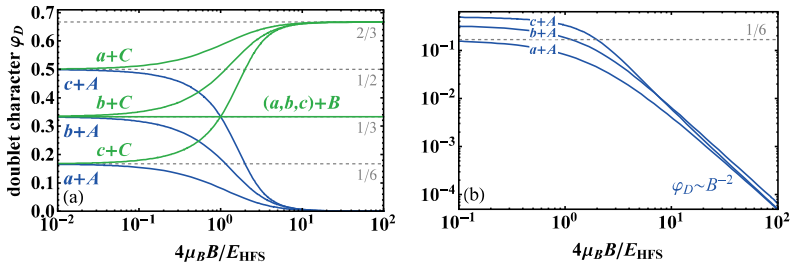

Figure 5.7: (a) Doublet character φ_D as function of magnetic field for all spin-state combinations involving the $f = 1$ hyperfine state of an $i = 3/2$ alkali atom (labeling as shown in Fig. 5.2); (b) same as (a) but showing φ_D for $(a, b, c) + A$ on a logarithmic scale.

$\varphi_D \to 0$ in the limit of high magnetic fields, the green lines $\varphi_D = 1/3$ or $2/3$. At low magnetic fields these spin-state combinations have $\varphi_D = q/6$, where $q = 0, \ldots, 4$. The red lines are the two doubly spin-stretched state combinations, for which $\varphi_D = 0$ for any magnetic field.

In Fig. 5.7(a) φ_D is plotted as function of magnetic field for all spin-state combinations involving the $f = 1$ hyperfine state of an $i = 3/2$ alkali atom, showing a smooth transition between the low and high magnetic field limits. In Fig. 5.7(b) φ_D is plotted on a logarithmic scale for $(a, b, c) + A$, emphasizing the asymptotic $\varphi_D \sim B^{-2}$ behavior for $4\mu_B B/E_{\rm HFS} >> 1$.

Appendix B: Finite temperature correction

The universal and non-universal MQDT loss rates given in Eq. 5.4 and Eq. 5.5 are the zero-temperature limits. Even though our effective collision temperature of $T = \mu(T_{\rm He^*}/m_{\rm He^*} + T_{\rm Rb}/m_{\rm Rb}) \approx T_{\rm He^*} = 22$ μK is far below the van der Waals energy and p-wave centrifugal barrier ($k_B \times 3.1$ mK and $k_B \times 3.4$ mK, respectively), it may be necessary to include a finite temperature correction. For the universal case, $P^{\rm re} = 1$, the energy dependent, thermal averaged, loss rate is given in Ref. [166] and is shown in Fig. 5.8(a), specifying the contributions from the s-wave and p-wave scattering. The loss rate is reduced by 8% at 22 μK compared to the zero-temperature limit.

For the non-universal case, $P^{\rm re} < 1$, the energy dependence itself also depends on P^{re} and a [167, 171], most notably in case of a potential resonance ($|a| >> \bar{a}$) or shape resonances [171], such as p-wave shape resonances, correlated with $a \approx 2\bar{a}$. The finite temperature corrections to Eq. 5.5 at 22 μK as function of $s = a/\bar{a}$ for several values of $P^{\rm re}$ are shown in Fig. 5.8(b).

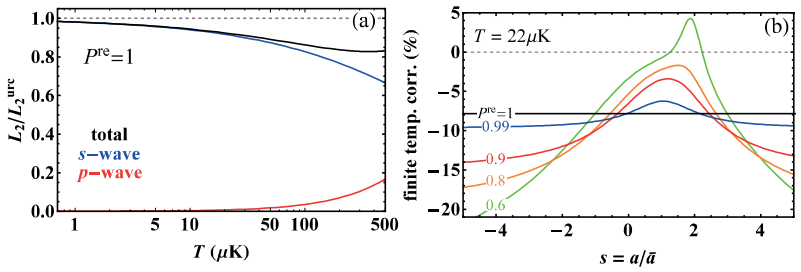

Figure 5.8: (a) Universal loss rate as function of temperature [166], indicating the s- and p-wave contribution. (b) Finite temperature corrections to L_2 at 22 μK for the non-universal case [167, 171] with respect to the zero-temperature limit (Eq. 5.5).

Appendix C: Spin-exchange collisions

For some spin-state combinations exothermic spin-exchange collisions (i. e. Zeeman and hyperfine state changing collisions) are spin-allowed and could in principle have a significant contribution to the total two-body loss rate. A simple expression of the spin-exchange rate coefficient in the zero-temperature limit has been derived for the case of atomic hydrogen (and also directly applicable to alkali atoms), namely Eq. 38 of Ref. [172]. For the case of He*+alkali collisions this expression becomes:

$$L_2^{\rm ex} = \pi \sqrt{\frac{2\Delta E}{\mu}} \, (a_Q - a_D)^2 \, |\langle \psi_f | P_Q - P_D | \psi_i \rangle|^2 \,, \tag{5.12}$$

where ΔE is the energy gain, μ is the reduced mass, a_Q (a_D) is the quartet (doublet) scattering length, ψ_i (ψ_f) is the initial (final) spin-state, and P_Q (P_D) the projection operator on the quartet (doublet) spin subspace.

For low magnetic fields the spin-factor $|\langle \psi_f | P_Q - P_D | \psi_i \rangle|^2$ can be expressed in terms of Clebsch-Gordan coefficients. For the ^{4}He*+^{87}Rb case the spin-state is given by $|\psi\rangle = |s_1, m_{s_1}; f_2, m_{f_2}\rangle$. Defining

$$\zeta_\alpha(S, m_S) \equiv \sum_{m_{s_2}} \sum_{m_{i_2}} C^{f_2, m_{f_2}}_{s_2, m_{s_2}; i_2, m_{i_2}} \, C^{S, m_S}_{s_1, m_{s_1}; s_2, m_{s_2}} \,, \tag{5.13}$$

where $\alpha = \{s_1, m_{s_1}; f_2, m_{f_2}; s_2, i_2\}$ is the set of spin quantum numbers of state ψ, then

$$\langle \psi_f | P_S | \psi_i \rangle = \sum_{m_S} \zeta_i(S, m_S) \zeta_f(S, m_S). \tag{5.14}$$

For the $h + A$ spin-state combination, in which the spin-allowed spin-exchange process is the hyperfine changing collision process $h + A \rightarrow a + B$, $|\langle \psi_f | P_Q - P_D | \psi_i \rangle|^2 = 2/3$. In Fig. 5.9 $L_2^{\rm ex}$ for $h + A$ is shown as function of

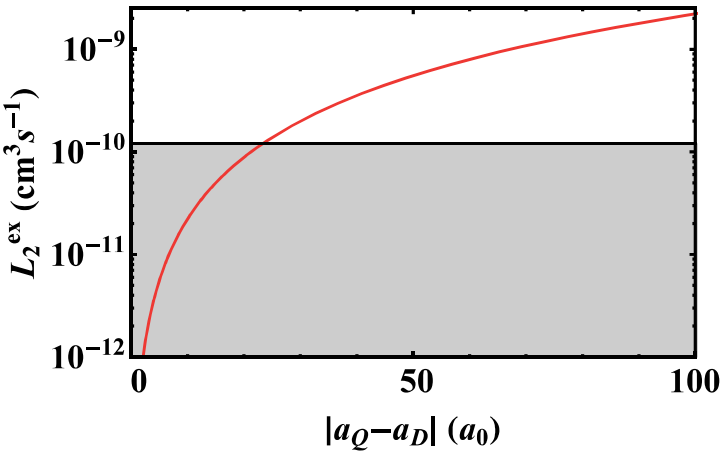

Figure 5.9: Loss rate $L_2^{\rm ex}$ due to hyperfine changing collisions for the $h + A$ mixture as function of the difference between the doublet and quartet scattering lengths $|a_Q - a_D|$. The gray area indicates a possible contribution to the measured total two-body loss.

$|a_Q - a_D|$, which together with our derived upper limit of 1.2×10^{10} cm^{3}s^{-1} gives the constraint $|a_Q - a_D| < 23a_0$ to the difference between the doublet and quartet scattering length.

At finite temperature the spin-exchange rate is given by Eq. 36 of Ref. [172], involving the (energy-dependent) phase shifts instead of the scattering lengths. Finite temperature corrections to the zero-temperature limit are expected to be small in our case, as our temperature of 22 μK is well below the van der Waals energy and p-wave centrifugal barrier. The only exceptions would be in case of a potential resonance ($|a| >> \bar{a}$) or a p-wave shape resonance ($a \approx 2\bar{a}$) in one of the two potentials, which is not the case for the quartet potential [87, 88]. The knowledge of the doublet potential is very limited, and the doublet scattering length is unknown. However, the relatively small total two-body loss rate for $h + A$, in combination with our analysis of the PI loss rate, does not support the presence of a potential resonance or p-wave shape resonance.

Appendix D: Overview of loss rates

An overview of the measured and derived two-body loss rates are given in Table 5.1. We have also added the two-body unitarity limit,

$$L_2^{\rm unitarity}(T) = \frac{\sqrt{2\pi}\hbar^2}{\mu^{3/2}\sqrt{k_B T}} \approx \frac{1.5 \times 10^{-8}}{\sqrt{T(\mu\mathrm{K})}}\mathrm{cm}^3\mathrm{s}^{-1} \qquad (5.15)$$

which at our temperature is more than one order of magnitude larger than our measured loss rates. Compared to other systems, here the unitarity limit is relatively high due to the small reduced mass μ.

Table 5.1: Overview of the measured and derived two-body loss rates for ^{4}He*+^{87}Rb, and comparison with the universal loss rate constant and unitarity limit (all units of 10^{-10} cm^{3}s^{-1}).

L_2^{h+C}	L_2^{a+A}	L_2^{a+C}	L_2^{h+A}	L_2^{PI}	L_2^{urc}		$L_2^{\mathrm{unitarity}}$
					$T = 0$	$T = 22$ μK	$T = 22$ μK
< 0.013	$0.53^{+0.20}_{-0.17}$	$2.3^{+1.2}_{-0.9}$	$2.2^{+0.8}_{-0.7}$	$3.4^{+0.8}_{-0.7}$	4.5	4.2	32

509242-L-bw-Flores
Processed on: 3-4-2017

Chapter 6

Outlook

In this chapter, the highlights of our experiments on ultracold samples (single-species and mixture) of ^{4}He* and ^{87}Rb are presented. Important issues and features of the preparation stage, in particular that of a mixture, using our single-beam optical dipole trap (or hybrid trap) scheme are emphasized. Finally, prospect towards realizing a dual-species Bose-Einstein condensate and observation of interspecies Feshbach resonances are outlined.

509242-L-bw-Flores
Processed on: 3-4-2017

6.1 Highlights

Our experiments involve an ultracold sample of ^{87}Rb and ^{4}He* atoms. In a single-species preparation, we are able to transfer a few 10^6 Rb atoms at a temperature below 20 μK into a hybrid trap, after MW-induced forced evaporative cooling in a quadrupole magnetic trap (QMT). By performing further forced evaporation in the hybrid trap, a BEC of a few 10^5 atoms is realized (see Ref. [107]; also briefly discussed in Chapter 2). We can also prepare a thermal sample of around 10^6 atoms at a temperature below 1 μK in a pure single-beam optical dipole trap (ODT) after evaporation in the hybrid trap. For He*, at least 10^6 atoms at a temperature below 25 μK can be transferred into a single-beam ODT (or hybrid trap) after RF-induced forced evaporation in a QMT (see Chapter 3), which is quite remarkable given that the lowest achievable temperature in a QMT for a light atomic species such as He* is strongly limited by Majorana spin-flips. A BEC of a few 10^4 to 10^5 atoms has been realized after forced evaporation in a single-beam ODT and hybrid trap.

For preparation of a mixture, we have demonstrated simultaneous RF-induced (He*) and MW-induced (Rb) forced evaporative cooling in a QMT (see Chapter 4). We have managed to transfer between 10^4 to 10^5 atoms at temperatures below 25 μK for both species into a pure single-beam ODT, which, however, is limited due to a couple of issues such as Majorana heating and interspecies loss during the magneto-optical trap (MOT) stage. Nonetheless, these initial atom numbers in the ODT have allowed us to study Penning-ionization (PI) reactions of spin-state combinations other than the pure quartet (see Chapter 5), for which a high density sample is not needed because the two-body loss rates are on the order of $10^{-11} - 10^{-10}$ cm^{3}s^{-1} and easily dominate over one-body loss. For the pure quartet doubly spin-stretched spin-state combination, an upper limit of the interspecies PI loss rate of 1.3×10^{-12} cm^{3}s^{-1} could be obtained because there is no significant difference between single species and mixture lifetimes. This suggests that the lifetime is only limited by background collisions. Still, it is worthwhile to improve the initial densities of both species in the ODT. For example, a more stringent constraint of the interspecies PI loss rate for pure quartet scattering can be obtained by performing lifetime measurements with a higher density sample, in which the interspecies two-body loss can be resolved from the one-body loss (and still dominates over three-body loss) contribution.

6.2 Towards a dual-species BEC in a single-beam ODT

Using the doubly spin-stretched spin-state combination, realizing a dual-species BEC is in principle possible. However, our currently limited initial atom numbers in the ODT hinders further forced evaporative cooling. In this section, proposed changes in the existing setup are discussed, which may lead to an improvement in the number of atoms of the mixture in the ODT. Firstly, the transfer efficiency of the mixture from the three-dimensional magneto-optical trap (3D-MOT) to the QMT is limited to around 40%, which is almost a factor of two lower compared to the single-species case. This constraint occurs during the optical molasses (OM) stage, in which a power imbalance between the incoming and reflected 3D-MOT beams is apparent due to losses from the vacuum chamber window, quarter waveplate and mirror, significantly shifting the position of the cloud away from the QMT center, thereby reducing the transfer efficiency to the QMT. In a single-species preparation, we compensate for this by initially offsetting the alignment of the MOT beams with respect to the QMT center such that after the OM stage loading the cloud still coincides with the QMT center.

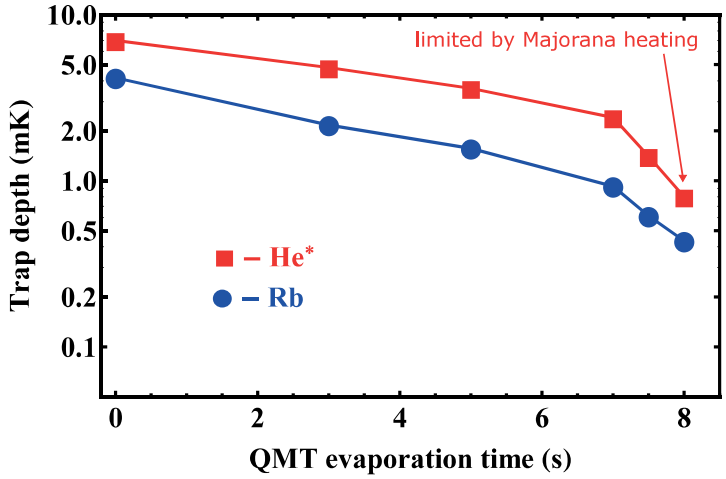

Figure 6.1: Trap depths of Rb (blue circles) and He* (red squares) during the coarse of simultaneous evaporative cooling in the QMT. Measured actual temperatures typically correspond to a truncation parameter $\eta \approx 10$. The lowest achievable temperature of He* (around 100 μK) is limited by Majorana heating, while the Rb temperature in principle can be pushed down to 20 μK before Majorana heating significantly affects the evaporation efficiency. Solid lines are a guide to the eye.

However, in a mixture, for which we send both beams of the two species in the same fiber, this flexibility in alignment is limited. Here, using an AR coated vacuum windows and optical elements better suited for 780 nm and 1083 nm can be a direct solution to minimize the power imbalance or at least provide similar optical power losses for the two wavelengths.

Secondly, additional losses in the Rb atom number due to heating from He^* during evaporative cooling in a QMT can in principle be minimized by keeping the temperatures of both species equal (or comparable) during the coarse of the evaporation process. This can be achieved by synchronizing the trap depths of both Rb and He^* (see Fig. 6.1 for the typical setting used during the simultaneous evaporation). This synchronization is possible based on the requirement of RF and MW frequencies for equal trap depths: $\nu_{\mathrm{MW}} - \nu_{\mathrm{HFS}} = 3\nu_{\mathrm{RF}}/2$, which still satisfies the condition: $\nu_{\mathrm{MW}} - \nu_{\mathrm{HFS}} < 3\nu_{\mathrm{RF}}$, for which RF frequencies used for He^* will not affect Rb (see Chapters 2 and 4). However, due to the limit on the lowest achievable temperature for He^* in a QMT (around 100 μK for the typical magnetic field gradient used in our experiment), this can only be realized by not pushing towards lower temperature in the evaporative cooling of Rb (i. e. at least 100 μK), which also reduces the subsequent transfer efficiency of Rb into the ODT. Here, a straightforward solution is to use higher ODT power that can provide sufficient trap depth for both species even when loading from a QMT at a temperature around 100 μK. An available ODT power of 10 W should already provide flexibility in loading from a QMT into a ODT with a transfer of a few 10^6 to 10^7 atoms at temperatures below 50 μK. A more sophisticated approach is by using a Ioffe-Pritchard type of magnetic trap instead of a QMT in which there is no Majorana heating. In here, the trap depths during simultaneous evaporative cooling in the QMT of both species can be synchronized without constraint, and the evaporation can be pushed towards lower temperature or even dual BEC such that the requirement in trap depth for a subsequent transfer into ODT becomes less stringent (i. e. lower ODT power or larger waist) [48, 155].

6.3 Prospect for interspecies Feshbach resonances

Feshbach resonances have become an indispensable tool in ultracold atom experiments, providing the possibility of experimentally tunable interatomic interactions and association of ultracold molecules. Observation of Feshbach resonances also reveals the binding energies of the least-bound vibrational molecular levels of the interaction potentials (see e. g. [175]). For He^*+alkali mixtures, Feshbach spectroscopy might be the only experimental technique to obtain detailed information about the doublet and quartet potentials. Furthermore, the PI reaction in He^*+Rb collisions offers a platform to study Feshbach resonances in the presence of a strong loss channel.

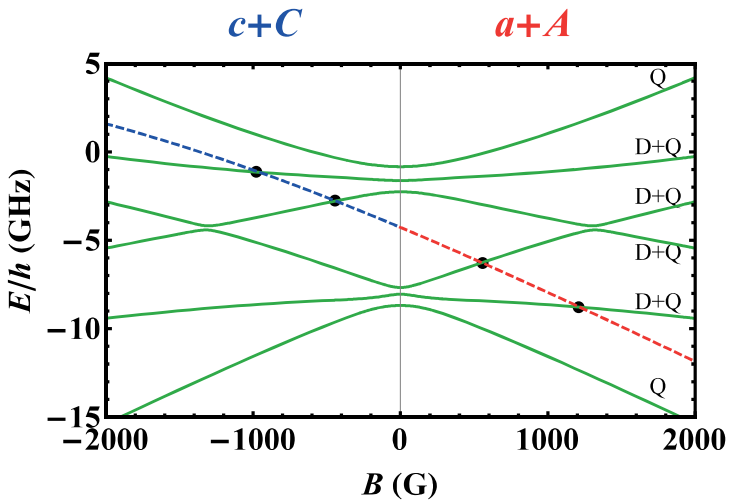

Figure 6.2: Near-threshold molecular spectra (green curves) obtained from the ABM calculation for the two spin-state combinations $c + C$ and $a + A$, consisting of 4 quartet (Q) and 2 doublet (D) states, for which 4 states (as indicated) are mixed by the hyperfine interaction. The input binding energies are $E_Q/h = 3.4$ GHz and $E_D/h = 5.2$ GHz, respectively (see text). The dashed (red and blue) curves correspond to the atomic threshold energies of the entrance channel. The negative magnetic field for the case of $c + C$ is artificial and only indicates a change in sign of the projection quantum number. Feshbach resonances occur at positions indicated by the black solid circles.

For interspecies s-wave Feshbach resonances for a ^{4}He*+^{87}Rb mixture to occur, spin-state combinations other than a pure quartet one are required, which are, however, accompanied by strong two-body losses. As the peak in the elastic cross-section around a Feshbach resonance and the signature of an enhanced loss feature are expected to be suppressed in the presence of a large two-body loss [159], the most promising spin-state combinations to start with are the ones with the smallest two-body loss. This corresponds to a combination with the smallest doublet character, i. e. $a + A$ or $c + C$ combination (see Chapter 5 and Fig. 5.2 for the labeling of spin-states). We have used the asymptotic-bound-state model (ABM), introduced by Tiecke *et al.* [176], to calculate the near-threshold molecular spectrum and predict the positions of possible s-wave Feshbach resonances, for which, however, a PI contribution is not included, similar to the pure He* case discussed in Ref. [177]. To be able to calculate the near-threshold molecular spectrum using the ABM, the inputs required are the binding energies of the least-bound quartet and doublet states, and a Franck-Condon factor (which for simplicity is taken as unity, see e. g. Ref. [176]). For the quartet bind-

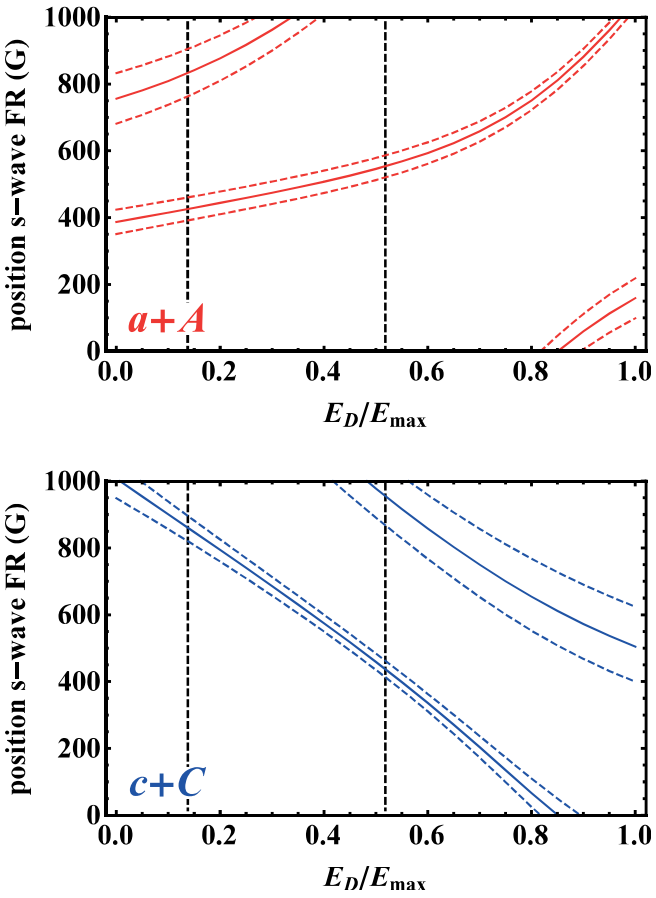

Figure 6.3: Positions of s-wave Feshbach resonances (FR) as function of the doublet binding energy normalized by the maximum binding energy of the least-bound vibrational state ($E_D/E_{\max}$), for spin-state combinations $a + A$ (top panel) and $c + C$ (bottom panel). The solid curves correspond to a fixed quartet binding energy $E_Q/h = 3.4 \pm 0.3$ GHz, while the dashed curves represents the error margin. The vertical dashed lines are bounds on the doublet scattering length ($-10a_0 < a_D < 44a_0$).

ing energy, we have obtained $E_Q/h = 3.4 \pm 0.3$ GHz, which is taken from our previously measured scattering length $a_Q = (17 \pm 4)a_0$ [88] following Ref. [178]. We have also obtained a range in the doublet binding energy 1.4 GHz $< E_D/h <$ 5.2 GHz, from the recently measured bounds on the doublet scattering length $-10a_0 < a_D < 44a_0$ (see Chapter 5). In Fig. 6.2, near-threshold molecular spectra for the two spin-state combinations $c + C$ and $a + A$, calculated with fixed input binding energies $E_Q/h = 3.4$ GHz and $E_D/h = 5.2$ GHz, respectively, are shown, demonstrating 6 molecular bound states (green curves) corresponding to the 4 quartet and 2 doublet states. The mixing of molecular states at zero magnetic field, which eventually leads to two subgroups consisting of three states is due to hyperfine coupling. The atomic threshold energies corresponding to the entrance channel are also shown (red and blue dashed curves), where crossings with a molecular bound state indicate the positions of the Feshbach resonances. In Fig. 6.3, the positions (in units of magnetic field) of the predicted Feshbach resonances for the two spin-state combinations $a + A$ (top panel) and $c + C$ (bottom panel) are illustrated as a function of the doublet binding energy (normalized by the maximum binding energy of the least-bound vibrational state $E_{\max}/h = 10$ GHz) indicating at least one Feshbach resonance at an experimentally accessible magnetic field (below 1000 G).

Typically, Feshbach spectroscopy is based on observing enhanced three-body loss as function of magnetic field. This is not possible with He*+alkali because of the presence of a large two-body loss. So instead, a signature of a Feshbach resonance will be based on a modification of the two-body loss due to PI, as we expect the coupling between the doublet and quartet interaction potentials at the Feshbach resonance to modify this PI loss. To perform Feshbach spectroscopy, the remaining atom number in the ODT for a fixed hold time should be measured as function of an applied magnetic field, corresponding to the range shown in Fig. 6.3. In our existing setup, this can be done using the same coils as in the QMT (or MOT) by switching to Helmholtz configuration. However, the magnetic field produced has a curvature at the center, which already above 50 G can provide a sufficient force for high-field seeking state atoms to escape from the trap. This constrains the possible combination for Feshbach spectroscopy only to the spin-state combination $c + C$.

Bibliography

[1] V. I. Balykin, V. S. Letokhov, and V. I. Mishin, "Observation of the cooling of free sodium atoms in a resonance laser field with a scanning frequency," *JETP Lett.*, vol. 29, p. 560, 1979.

[2] V. I. Balykin, V. S. Letokhov, and V. I. Mishin, "Cooling of sodium atoms by resonant laser emission," *Sov. Phys. JETP*, vol. 51, p. 692, 1980.

[3] S. V. Andreev, V. I. Balykin, V. S. Letokhov, and V. G. Minogin, "Radiative slowing and reduction of the energy spread of a beam of sodium atoms to 1.5 K in an oppositely directed laser beam," *JETP Lett.*, vol. 34, p. 442, 1981.

[4] W. D. Phillips and H. Metcalf, "Laser deceleration of an atomic beam," *Phys. Rev. Lett.*, vol. 48, p. 596, 1982.

[5] S. V. Andreev, V. I. Balykin, V. S. Letokhov, and V. G. Minogin, "Radiative slowing down and monochromatization of a beam of sodium atoms in a counterpropagating laser beam," *Sov. Phys. JETP*, vol. 55, p. 828, 1982.

[6] J. V. Prodan, W. D. Phillips, and H. Metcalf, "Laser production of a very slow monoenergetic atomic beam," *Phys. Rev. Lett.*, vol. 49, p. 1149, 1982.

[7] S. Chu, L. Hollberg, J. E. Bjorkholm, A. Cable, and A. Ashkin, "Three-dimensional viscous confinement and cooling of atoms by resonance radiation pressure," *Phys. Rev. Lett.*, vol. 55, p. 48, 1985.

[8] E. L. Raab, M. Prentiss, A. Cable, S. Chu, and D. E. Pritchard, "Trapping of neutral sodium atoms with radiation pressure," *Phys. Rev. Lett.*, vol. 59, p. 2631, 1987.

[9] W. Petrich, M. H. Anderson, J. R. Ensher, and E. A. Cornell, "Stable, tightly confining magnetic trap for evaporative cooling of neutral atoms," *Phys. Rev. Lett.*, vol. 74, p. 3352, 1995.

[10] K. B. Davis, M.-O. Mewes, M. A. Joffe, M. R. Andrews, and W. Ketterle, "Evaporative cooling of sodium atoms," *Phys. Rev. Lett.*, vol. 74, p. 5202, 1995.

[11] M. H. Anderson, J. R. Ensher, M. R. Matthews, C. E. Wieman, and E. A. Cornell, "Observation of Bose-Einstein condensation in a dilute atomic vapor," *Science*, vol. 269, p. 198, 1995.

[12] K. B. Davis, M.-O. Mewes, M. R. Andrews, N. J. van Druten, D. S. Durfee, D. M. Kurn, and W. Ketterle, "Bose-Einstein condensation in a gas of sodium atoms," *Phys. Rev. Lett.*, vol. 75, p. 3969, 1995.

[13] B. DeMarco and D. S. Jin, "Onset of Fermi degeneracy in a trapped atomic gas," *Science*, vol. 285, p. 1703, 1999.

[14] A. Ashkin, "Applications of laser radiation pressure," *Science*, vol. 210, p. 1081, 1980.

[15] D. Guéry-Odelin, J. Söding, P. Desbiolles, and J. Dalibard, "Is Bose-Einstein condensation of atomic cesium possible?," *Europhys. Lett.*, vol. 44, p. 26, 1998.

[16] S. Chu, J. E. Bjorkholm, A. Ashkin, and A. Cable, "Experimental observation of optically trapped atoms," *Phys. Rev. Lett.*, vol. 57, p. 314, 1986.

[17] D. M. Stamper-Kurn, M. R. Andrews, A. P. Chikkatur, S. Inouye, H. J. Miesner, J. Stenger, and W. Ketterle, "Optical confinement of a Bose-Einstein condensate," *Phys. Rev. Lett.*, vol. 80, 1998.

[18] S. Inouye, M. R. Andrews, J. Stenger, H. J. Miesner, D. M. Stamper-Kurn, and W. Ketterle, "Observation of Feshbach resonances in a Bose-Einstein condensate," *Nature*, vol. 392, p. 151, 1998.

[19] C. Chin, R. Grimm, P. S. Julienne, and E. Tiesinga, "Feshbach resonances in ultracold gases," *Rev. Mod. Phys.*, vol. 82, p. 1225, 2010.

[20] S. L. Cornish, N. R. Claussen, J. L. Roberts, E. A. Cornell, and C. E. Wieman, "Stable ^{85}Rb Bose-Einstein condensates with widely tunable interactions," *Phys. Rev. Lett.*, vol. 85, p. 1795, 2000.

[21] T. Weber, J. Herbig, M. Mark, H.-C. Nägerl, and R. Grimm, "Bose-Einstein condensation of cesium," *Science*, vol. 299, p. 232, 2003.

[22] C. A. Regal, C. Ticknor, J. L. Bohn, and D. S. Jin, "Creation of ultracold molecules from a Fermi gas of atoms," *Nature*, vol. 424, p. 47, 2003.

[23] J. Herbig, T. Kraemer, M. Mark, T. Weber, C. Chin, H.-C. Nägerl, and R. Grimm, "Preparation of a pure molecular quantum gas," *Science*, vol. 301, p. 1510, 2003.

[24] J. G. Danzl, E. Haller, M. Gustavsson, M. J. Mark, R. Hart, N. Bouloufa, O. Dulieu, H. Ritsch, and H.-C. Nägerl, "Quantum gas of deeply bound ground state molecules," *Science*, vol. 321, p. 1062, 2008.

[25] K.-K. Ni, S. Ospelkaus, M. H. G. de Miranda, A. Pe'er, B. Neyenhuis, J. J. Zirbel, S. Kotochigova, P. S. Julienne, D. S. Jin, and J. Ye, "A High phase-space-density gas of polar molecules," *Science*, vol. 322, p. 231, 2008.

[26] J. G. Danzl, M. J. Mark, E. Haller, M. Gustavsson, R. Hart, J. Aldegunde, J. M. Hutson, and H.-C. Nägerl, "An ultracold high-density sample of rovibronic ground-state molecules in an optical lattice," *Nature Phys.*, vol. 6, p. 265, 2010.

[27] C. C. Bradley, C. A. Sackett, J. J. Tollett, and R. G. Hulet, "Evidence of Bose-Einstein condensation in an atomic gas with attractive interactions," *Phys. Rev. Lett.*, vol. 75, p. 1687, 1995.

[28] G. Modugno, G. Ferrari, G. Roati, R. J. Brecha, A. Simoni, and M. Inguscio, "Bose-Einstein condensation of potassium atoms by sympathetic cooling," *Science*, vol. 294, p. 1320, 2001.

[29] A. G. Truscott, K. E. Strecker, W. I. M. Alexander, G. B. Partridge, and R. G. Hulet, "Observation of Fermi pressure in a gas of trapped atoms," *Science*, vol. 291, p. 2570, 2001.

[30] G. Roati, M. Zaccanti, C. D'Errico, J. Catani, M. Modugno, A. Simoni, M. Inguscio, and G. Modugno, "^{39}K Bose-Einstein condensate with tunable interaction," *Phys. Rev. Lett.*, vol. 99, p. 010403, 2007.

[31] S. Stellmer, M. K. Tey, B. Huang, R. Grimm, and F. Schreck, "Bose-Einstein condensation of strontium," *Phys. Rev. Lett.*, vol. 103, p. 200401, 2009.

[32] S. Kraft, F. Vogt, O. Appel, F. Riehle, and U. Sterr, "Bose-Einstein condensation of alkaline earth atoms: ^{40}Ca," *Phys. Rev. Lett.*, vol. 103, p. 130401, 2009.

[33] A. Robert, O. Sirjean, A. Browaeys, J. Poupard, S. Nowak, D. Boiron, C. I. Westbrook, and A. Aspect, "A Bose-Einstein condensate of metastable atoms," *Science*, vol. 292, p. 461, 2001.

[34] F. Pereira Dos Santos, J. Léonard, J. Wang, C. J. Barrelet, F. Perales, E. Rasel, C. S. Unnikrishnan, M. Leduc, and C. Cohen-Tannoudji,

"Bose-Einstein condensation of metastable helium," *Phys. Rev. Lett.*, vol. 86, p. 3459, 2001.

[35] A. S. Tychkov, T. Jeltes, J. M. McNamara, P. J. J. Tol, N. Herschbach, W. Hogervorst, and W. Vassen, "Metastable helium Bose-Einstein condensate with a large number of atoms," *Phys. Rev. A*, vol. 73, p. 031603(R), 2006.

[36] J. M. McNamara, T. Jeltes, A. S. Tychkov, W. Hogervorst, and W. Vassen, "Degenerate Bose-Fermi mixture of metastable atoms," *Phys. Rev. Lett.*, vol. 97, p. 080404, 2006.

[37] A. Griesmaier, J. Werner, S. Hensler, J. Stuhler, and T. Pfau, "Bose-Einstein condensation of chromium," *Phys. Rev. Lett.*, vol. 94, p. 160401, 2005.

[38] Y. Takasu, K. Maki, K. Komori, T. Takano, K. Honda, M. Kumakura, T. Yabuzaki, and Y. Takahashi, "Spin-singlet Bose-Einstein condensation of two-electron atoms," *Phys. Rev. Lett.*, vol. 91, p. 040404, 2003.

[39] T. Fukuhara, Y. Takasu, M. Kumakura, and Y. Takahashi, "Degenerate Fermi gases of ytterbium," *Phys. Rev. Lett.*, vol. 98, p. 030401, 2007.

[40] M. Lu, N. Q. Burdick, S. H. Youn, and B. L. Lev, "Strongly dipolar Bose-Einstein condensate of dysprosium," *Phys. Rev. Lett.*, vol. 107, p. 190401, 2011.

[41] M. Lu, N. Q. Burdick, and B. L. Lev, "Quantum degenerate dipolar Fermi gas," *Phys. Rev. Lett.*, vol. 108, p. 215301, 2012.

[42] K. Aikawa, A. Frisch, M. Mark, S. Baier, A. Rietzler, R. Grimm, and F. Ferlaino, "Bose-Einstein condensation of erbium," *Phys. Rev. Lett.*, vol. 108, p. 210401, 2012.

[43] T. Kraemer, M. Mark, P. Waldburger, J. G. Danzl, C. Chin, B. Engeser, A. D. Lange, K. Pilch, A. Jaakkola, H.-C. Nägerl, and R. Grimm, "Evidence for Efimov quantum states in an ultracold gas of cesium atoms," *Nature*, vol. 440, p. 315, 2006.

[44] Y. Wang, J. P. D. Incao, and B. D. Esry, "Ultracold few-body systems," *Adv. At. Mol. Opt. Phys.*, vol. 62, p. 1, 2013.

[45] I. Bloch, J. Dalibard, and W. Zwerger, "Many-body physics with ultracold gases," *Rev. Mod. Phys.*, vol. 80, p. 885, 2008.

[46] M. Greiner, O. Mandel, T. Esslinger, T. W. Hänsch, and I. Bloch, "Quantum phase transition from a superfluid to a Mott insulator in a gas of ultracold atoms," *Nature*, vol. 415, p. 39, 2002.

[47] I. Bloch, J. Dalibard, and S. Nascimbène, "Quantum simulations with ultracold quantum gases," *Nature Phys.*, vol. 8, p. 267, 2012.

[48] R. van Rooij, J. S. Borbely, J. Simonet, M. D. Hoogerland, K. S. E. Eikema, R. A. Rozendaal, and W. Vassen, "Frequency metrology in quantum degenerate helium: Direct measurement of the $2^3S_1 \rightarrow 2^1S_0$ transition," *Science*, vol. 333, p. 196, 2011.

[49] R. P. M. J. W. Notermans, R. J. Rengelink, and W. Vassen, "Comparison of spectral linewidths for quantum degenerate bosons and fermions," *Phys. Rev. Lett.*, vol. 117, p. 213001, 2016.

[50] U. Schlöder, H. Engler, U. Schünemann, R. Grimm, and M. Weidemüller, "Cold inelastic collisions between lithium and cesium in a two-species magneto-optical trap," *Eur. Phys. J. D*, vol. 7, p. 331, 1999.

[51] J. Goldwin, S. B. Papp, B. DeMarco, and D. S. Jin, "Two-species magneto-optical trap with ^{40}K and ^{87}Rb," *Phys. Rev. A*, vol. 81, p. 043637, 2010.

[52] Z. Hadzibabic, C. A. Stan, K. Dieckmann, S. Gupta, M. W. Zwierlein, A. Görlitz, and W. Ketterle, "Two-species mixture of quantum degenerate Bose and Fermi gases," *Phys. Rev. Lett.*, vol. 88, p. 160401, 2002.

[53] L. Wacker, N. B. Jorgensen, D. Birkmose, R. Horchani, W. Ertmer, C. Klempt, N. Winter, J. Sherson, and J. Arlt, "Tunable dual-species Bose-Einstein condensates of ^{39}K and ^{87}Rb," *Phys. Rev. A*, vol. 92, p. 053602, 2015.

[54] N. Spethmann, F. Kindermann, S. John, C. Weber, D. Meschede, and A. Widera, "Dynamics of single neutral impurity atoms immersed in an ultracold gas," *Phys. Rev. Lett.*, vol. 109, p. 235301, 2012.

[55] R. Scelle, T. Rentrop, A. Trautmann, T. Schuster, and M. K. Oberthaler, "Motional coherence of fermions immersed in a Bose gas," *Phys. Rev. Lett.*, vol. 111, p. 070401, 2013.

[56] M.-G. Hu, M. Van de Graaff, D. Kedar, J. P. Corson, E. A. Cornell, and D. S. Jin, "Bose polarons in the strongly interacting regime," *Phys. Rev. Lett.*, vol. 117, p. 055301, 2016.

[57] D. Schlippert, J. Hartwig, H. Albers, L. L. Richardson, C. Schubert, A. Roura, W. P. Schleich, W. Ertmer, and E. M. Rasel, "Quantum test of the universality of free fall," *Phys. Rev. Lett.*, vol. 112, p. 203002, 2014.

[58] F. M. Spiegelhalder, A. Trenkwalder, D. Naik, G. Kerner, E. Wille, G. Hendl, F. Schreck, and R. Grimm, "All-optical production of a degenerate mixture of ^{6}Li and ^{40}K and creation of heteronuclear molecules," *Phys. Rev. A*, vol. 81, p. 043637, 2010.

[59] C. Silber, S. Günther, C. Marzok, B. Deh, Ph. W. Courteille, and C. Zimmermann, "Quantum-degenerate mixture of fermionic lithium and bosonic rubidium gases," *Phys. Rev. Lett.*, vol. 95, p. 170408, 2005.

[60] M. Taglieber, A.-C. Voigt, T. Aoki, T. Hänsch, and K. Dieckmann, "Quantum degenerate two-species Fermi-Fermi mixture coexisting with a Bose-Einstein condensate," *Phys. Rev. Lett.*, vol. 100, p. 010401, 2008.

[61] A. Mosk, S. Kraft, M. Mudrich, K. Singer, W. Wohlleben, R. Grimm, and M. Weidemüller, "Mixture of ultracold lithium and cesium atoms in an optical dipole trap," *Appl. Phys. B*, vol. 73, p. 791, 2001.

[62] J. W. Park, C.-H. Wu, I. Santiago, T. G. Tiecke, S. Will, P. Ahmadi, and M. W. Zwierlein, "Quantum degenerate Bose-Fermi mixture of chemically different atomic species with widely tunable interactions," *Phys. Rev. A*, vol. 85, p. 051602(R), 2012.

[63] F. Wang, X. Li, D. Xiong, and D. Wang, "A double species ^{23}Na and ^{87}Rb Bose-Einstein condensate with tunable miscibility via an interspecies Feshbach resonance," *J. Phys. B*, vol. 49, p. 015302, 2016.

[64] M. Gröbner, P. Weinmann, F. Meinert, K. Lauber, E. Kirilov, and H.-C. Nägerl, "A new quantum gas apparatus for ultracold mixtures of K and Cs and KCs ground-state molecules," *J. Mod. Opt.*, vol. 63, p. 1829, 2016.

[65] A. Lercher, T. Takekoshi1, M. Debatin, B. Schuster, R. Rameshan, F. Ferlaino, R. Grimm, and H.-C. Nägerl, "Production of a dual-species Bose-Einstein condensate of Rb and Cs atoms," *Eur. Phys. J. D*, vol. 65, p. 3, 2011.

[66] T. Takekoshi, L. Reichsöllner, A. Schindewolf, J. M. Hutson, C. R. L. Sueur, O. Dulieu, F. Ferlaino, R. Grimm, and H.-C. Nägerl, "Ultracold dense samples of dipolar RbCs molecules in the rovibrational and hyperfine ground state," *Phys. Rev. Lett.*, vol. 113, p. 205301, 2014.

[67] P. K. Molony, P. D. Gregory, Z. Ji, B. Lu, M. P. Köppinger, C. R. L. Sueur, C. L. Blackley, J. M. Hutson, and S. L. Cornish, "Creation of ultracold ^{87}Rb^{133}Cs molecules in the rovibrational ground state," *Phys. Rev. Lett.*, vol. 113, p. 255301, 2014.

[68] J. W. Park, S. A. Will, and M. W. Zwierlein, "Ultracold dipolar gas of fermionic ^{23}Na^{40}K molecules in their absolute ground state," *Phys. Rev. Lett.*, vol. 114, p. 205302, 2015.

[69] M. Guo, B. Zhu, B. Lu, X. Ye, F. Wang, R. Vexiau, N. Bouloufa-Maafa, G. Quéméner, O. Dulieu, and D. Wang, "Creation of an ultracold gas of ground-state dipolar ^{23}Na^{87}Rb molecules," *Phys. Rev. Lett.*, vol. 116, p. 205303, 2016.

[70] R. Pires, J. Ulmanis, S. Häfner, M. Repp, A. Arias, E. D. Kuhnle, and M. Weidemüller, "Observation of Efimov resonances in a mixture with extreme mass imbalance," *Phys. Rev. Lett.*, vol. 112, p. 250404, 2014.

[71] S.-K. Tung, K. Jiménez-García, J. Johansen, C. Parker, and C. Chin, "Geometric scaling of Efimov states in a ^{6}Li-^{133}Cs mixture," *Phys. Rev. Lett.*, vol. 113, p. 240402, 2014.

[72] B. Pasquiou, A. Bayerle, S. M. Tzanova, S. Stellmer, J. Szczepkowski, M. Parigger, R. Grimm, and F. Schreck, "Quantum degenerate mixtures of strontium and rubidium atoms," *Phys. Rev. A*, vol. 88, p. 023601, 2013.

[73] N. Nemitz, F. Baumer, F. Münchow, S. Tassy, and A. Görlitz, "Production of heteronuclear molecules in an electronically excited state by photo-association in a mixture of ultracold Yb and Rb," *Phys. Rev. A*, vol. 79, p. 061403(R), 2009.

[74] V. D. Vaidya, J. Tiamsuphat, S. L. Rolston, and J. V. Porto, "Degenerate Bose-Fermi mixtures of rubidium and ytterbium," *Phys. Rev. A*, vol. 92, p. 043604, 2015.

[75] H. Hara, Y. Takasu, Y. Yamaoka, J. M. Doyle, and Y. Takahashi, "Quantum degenerate mixtures of alkali and alkaline-earth-like atoms," *Phys. Rev. Lett.*, vol. 106, p. 205304, 2011.

[76] A. H. Hansen, A. Khramov, W. H. Dowd, A. O. Jamison, V. V. Ivanov, and S. Gupta, "Quantum degenerate mixture of ytterbium and lithium atoms," *Phys. Rev. A*, vol. 84, p. 011606(R), 2011.

[77] S. L. Kemp, K. L. Butler, R. Freytag, S. A. Hopkins, E. A. Hinds, M. R. Tarbutt, and S. L. Cornish, "Production and characterization

of a dual species magneto-optical trap of cesium and ytterbium," *Rev. Sc. Instr.*, vol. 87, p. 023105, 2016.

[78] F. Bardou, O. Emile, J. M. Courty, C. I. Westbrook, and A. Aspect, "Magneto-optical trapping of metastable helium: Collisions in the presence of resonant light," *Europhys. Lett.*, vol. 20, p. 681, 1992.

[79] W. Rooijakkers, W. Hogervorst, and W. Vassen, "Laser deceleration and trapping of metastable helium atoms," *Opt. Commun.*, vol. 135, p. 149, 1997.

[80] P. J. J. Tol, N. Herschbach, E. A. Hessels, W. Hogervorst, and W. Vassen, "Large numbers of cold metastable helium atoms in a magneto-optical trap," *Phys. Rev. A*, vol. 60, p. 761(R), 1999.

[81] G. V. Shlyapnikov, J. T. M. Walraven, U. M. Rahmanov, and M. W. Reynolds, "Decay kinetics and Bose condensation in a gas of spin-polarized triplet helium," *Phys. Rev. Lett.*, vol. 73, p. 3247, 1994.

[82] N. Herschbach, P. J. J. Tol, W. Hogervorst, and W. Vassen, "Suppression of Penning ionization by spin polarization of cold He(2^3S) atoms," *Phys. Rev. A*, vol. 61, p. 050702, 2000.

[83] S. Nowak, A. Browaeys, J. Poupard, A. Robert, D. Boiron, C. Westbrook, and A. Aspect, "Magnetic trapping of metastable helium atoms," *Appl. Phys. B*, vol. 70, p. 455, 2000.

[84] S. Moal, M. Portier, J. Kim, J. Dugué, U. D. Rapol, M. Leduc, and C. Cohen-Tannoudji, "Accurate determination of the scattering length of metastable helium atoms using dark resonances between atoms and exotic molecules," *Phys. Rev. Lett.*, vol. 96, p. 023203, 2006.

[85] W. Vassen, C. Cohen-Tannoudji, M. Leduc, D. Boiron, C. Westbrook, A. Truscott, K. Baldwin, G. Birkl, P. Cancio, and M. Trippenbach, "Cold and trapped metastable noble gases," *Rev. Mod. Phys.*, vol. 84, p. 175, 2012.

[86] J. E. Sansonetti, "Wavelengths, transition probabilities, and energy levels for the spectra of cesium (Cs I - Cs LV)," *J. Phys. Chem. Ref. Data*, vol. 38, p. 761, 2009.

[87] D. Kędziera, Ł. Mentel, P. S. Żuchowski, and S. Knoop, "Ab initio interaction potentials and scattering lengths for ultracold mixtures of metastable helium and alkali-metal atoms," *Phys. Rev. A*, vol. 91, p. 062711, 2015.

[88] S. Knoop, P. S. Żuchowski, D. Kędziera, Ł. Mentel, M. Puchalski, H. P. Mishra, A. S. Flores, and W. Vassen, "Ultracold mixtures of

metastable He and Rb: Scattering lengths from ab initio calculations and thermalization measurements," *Phys. Rev. A*, vol. 90, p. 022709, 2014.

[89] M.-W. Ruf, A. J. Yencha, and H. Hotop, "The interaction of metastable helium atoms with alkali atoms," *Z. Phys. D*, vol. 5, p. 9, 1987.

[90] C. E. Johnson, C. A. Tipton, and H. G. Robinson, "Penning ionisation of Na, K, Rb and Cs by He(2^3S_1) in a stationary afterglow," *J. Phys. B: At. Mol. Phys.*, vol. 11, p. 927, 2013.

[91] L. J. Byron, R. G. Dall, and A. G. Truscott, "Trap loss in a metastable helium-rubidium magneto-optical trap," *Phys. Rev. A*, vol. 81, p. 013405, 2010.

[92] L. J. Byron, R. G. Dall, W. Rugway, and A. G. Truscott, "Suppression of Penning ionization in a spin-polarized mixture of rubidium and He*," *New. J. Phys.*, vol. 12, p. 013004, 2010.

[93] T. W. Hänsch and A. L. Schawlow, "Cooling of gases by laser radiation," *Opt. Comm.*, vol. 13, p. 68, 1975.

[94] A. L. Migdall, J. V. Prodan, W. D. Phillips, T. H. Bergeman, and H. J. Metcalf, "First observation of magnetically trapped neutral atoms," *Phys. Rev. Lett.*, vol. 54, p. 2596, 1985.

[95] R. Dubessy, K. Merloti, L. Longehambon, P. E. Pottie, T. Liennard, A. Perrin, V. Lorent, and H. Perrin, "Rubidium 87 Bose-Einstein condensate in an optically plugged quadrupole trap," *Phys. Rev. A*, vol. 85, p. 013643, 2012.

[96] J. D. Miller, R. A. Cline, and D. J. Heinzen, "Far-off-resonance optical trapping of atoms," *Phys. Rev. A*, vol. 47, p. 4568(R), 1993.

[97] Y.-J. Lin, A. R. Perry, R. L. Compton, I. B. Spielman, and J. V. Porto, "Rapid production of ^{87}Rb Bose-Einstein condensates in a combined magnetic and optical potential," *Phys. Rev. A*, vol. 79, p. 063631, 2009.

[98] H. Metcalf and P. van der Straten, *Laser cooling and trapping of neutral atoms.* Springer Verlag, 1999.

[99] W. Ketterle and N. J. van Druten, "Evaporative cooling of trapped atoms," *Adv. At. Mol. Opt. Phys.*, vol. 37, p. 181, 1996.

[100] R. Grimm, M. Weidemüller, and Y. B. Ovchinnikov, "Optical dipole traps for neutral atoms," *Adv. At. Mol. Opt. Phys.*, vol. 42, p. 95, 2000.

[101] R. Stas, *Trapping fermionic and bosonic helium atoms.* PhD thesis, Vrije Universiteit Amsterdam, 2005.

[102] R. J. W. Stas, J. M. McNamara, W. Hogervorst, and W. Vassen, "Simultaneous magneto-optical trapping of a boson-fermion mixture of metastable helium atoms," *Phys. Rev. Lett.*, vol. 93, p. 053001, 2004.

[103] E. A. Donley, T. P. Heavner, F. Levi, M. O. Tataw, and S. R. Jefferts, "Double-pass acousto-optic modulator system," *Rev. Sci. Instrum.*, vol. 76, p. 063112, 2005.

[104] H. C. Mastwijk, J. W. Thomsen, P. van der Straten, and A. Niehaus, "Optical collisions of cold, metastable helium atoms," *Phys. Rev. Lett.*, vol. 80, p. 5516, 1998.

[105] S. J. Park, J. Noh, and J. Mun, "Cold atomic beam from a two-dimensional magneto-optical trap with two-color pushing laser beams," *Opt. Commun.*, vol. 285, p. 3950, 2012.

[106] R. J. W. Stas, J. M. McNamara, W. Hogervorst, and W. Vassen, "Homonuclear ionizing collisions between laser-cooled metastable helium atoms," *Phys. Rev. A*, vol. 73, p. 032713, 2006.

[107] H. P. Mishra, A. S. Flores, W. Vassen, and S. Knoop, "Efficient production of an ^{87}Rb $F = 2$, $m_F = 2$ Bose-Einstein condensate in a hybrid trap," *Eur. Phys. J. D*, vol. 69, p. 52, 2015.

[108] A. S. Flores, H. P. Mishra, W. Vassen, and S. Knoop, "Simple method for producing Bose-Einstein condensates of metastable helium in a single beam optical dipole trap," *Appl. Phys. B*, vol. 121, p. 391, 2015.

[109] G. B. Partridge, J.-C. Jaskula, M. Bonneau, D. Boiron, and C. I. Westbrook, "Bose-Einstein condensation and spin mixtures of optically trapped metastable helium," *Phys. Rev. A*, vol. 81, p. 053631, 2010.

[110] M. S. Safronova, B. Arora, and C. W. Clark, "Frequency-dependent polarizabilities of alkali-metal atoms from ultraviolet through infrared spectral regions," *Phys. Rev. A*, vol. 73, p. 022505, 2006.

[111] R. P. M. J. W. Notermans, R. J. Rengelink, K. A. H. van Leeuwen, and W. Vassen, "Magic wavelengths for the $2^3\mathrm{S} \rightarrow 2^1\mathrm{S}$ transition in helium," *Phys. Rev. A*, vol. 90, p. 052508, 2014.

[112] T. van Leent, *Saturated fluorescence imaging and spin-polarization of ultracold metastable helium.* BSc thesis, Vrije Universiteit Amsterdam, 2013.

[113] L. D. Landau, "Theory of energy transfer II," *Phys. Z. Sow.*, vol. 2, p. 46, 1932.

[114] C. Zener, "Non-adiabatic crossing of energy levels," *Proc. R. Soc.*, vol. 137, p. 696, 1932.

[115] T. P. Crowley, E. A. Donley, and T. P. Heavner, "Quantum-based microwave power measurements: Proof-of-concept experiment," *Rev. Sci. Instrum.*, vol. 75, p. 2575, 2004.

[116] M. L. Goldman, *Landau-Zener transition and a Feshbach resonance in spinor Bose-Einstein condensates*. BSc thesis, Amherst College, 2008.

[117] G. Kleine Büning, J.Will, W. Ertmer, C. Klempt, and J. Arlt, "A slow gravity compensated atom laser," *Appl. Phys. B*, vol. 100, p. 117, 2010.

[118] M. Schellekens, R. Hoppeler, A. Perrin, J. Viana Gomes, D. Boiron, A. Aspect, and C. I. Westbrook, "Hanbury Brown-Twiss effect for ultracold quantum gases," *Science*, vol. 310, p. 648, 2005.

[119] T. Jeltes, J. M. McNamara, W. Hogervorst, W. Vassen, V. Krachmalnicoff, M. Schellekens, A. Perrin, H. Chang, D. Boiron, A. Aspect, and C. I. Westbrook, "Comparison of the Hanbury Brown-Twiss effect for Bosons and Fermions," *Nature*, vol. 445, p. 402, 2007.

[120] S. S. Hodgman, R. G. Dall, A. G. Manning, K. G. H. Baldwin, and A. G. Truscott, "Direct measurement of long-range third-order coherence in Bose-Einstein condensates," *Science*, vol. 331, p. 1046, 2011.

[121] R. Lopes, A. Imanaliev, A. Aspect, M. Cheneau, D. Boiron, and C. I. Westbrook, "Atomic Hong-Ou-Mandel experiment," *Nature*, vol. 520, p. 66, 2015.

[122] A. G. Manning, R. I. Khakimov, R. G. Dall, and A. G. Truscott, "Wheelers delayed-choice gedanken experiment with a single atom," *Nature Phys.*, vol. 11, p. 539, 2015.

[123] R. P. M. J. W. Notermans and W. Vassen, "High-precision spectroscopy of the forbidden $2^3S_1 \rightarrow 2^1P_1$ transition in quantum degenerate metastable helium," *Phys. Rev. Lett.*, vol. 112, p. 253002, 2014.

[124] B. M. Henson, R. I. Khakimov, R. G. Dall, K. G. H. Baldwin, L.-Y. Tang, and A. G. Truscott, "Precision measurement of the 413 nm tune-out wavelength for metastable helium," *Phys. Rev. Lett.*, vol. 115, p. 043004, 2015.

[125] F. Pereira Dos Santos, J. Léonard, J. Wang, C. J. Barrelet, F. Perales, E. Rasel, C. S. Unnikrishnan, M. Leduc, and C. Cohen-Tannoudji,

"Production of a Bose-Einstein condensate of metastable helium atoms," *Eur. Phys. J. D*, vol. 19, p. 103, 2002.

[126] R. G. Dall and A. G. Truscott, "Bose-Einstein condensation of metastable helium in a bi-planar quadrupole Ioffe configuration trap," *Opt. Commun.*, vol. 270, p. 255, 2007.

[127] S. C. Doret, C. B. Connolly, W. Ketterle, and J. M. Doyle, "Buffer-gas cooled Bose-Einstein condensate," *Phys. Rev. Lett.*, vol. 103, p. 103005, 2009.

[128] M. Keller, M. Kotyrba, F. Leupold, M. Singh, M. Ebner, and A. Zeilinger, "A Bose-Einstein condensate of metastable helium for quantum correlation experiments," *Phys. Rev. A*, vol. 90, p. 063607, 2014.

[129] R. G. Dall, S. S. Hodgman, M. T. Johnsson, K. G. H. Baldwin, and A. G. Truscott, "Transverse mode imaging of guided matter waves," *Phys. Rev. A*, vol. 81, p. 011602(R), 2010.

[130] Q. Bouton, R. Chang, A. L. Hoendervanger, F. Nogrette, A. Aspect, C. I. Westbrook, and D. Clément, "Fast production of Bose-Einstein condensates of metastable helium," *Phys. Rev. A*, vol. 91, p. 061402(R), 2015.

[131] R. Chang, A. L. Hoendervanger, Q. Bouton, Y. Fang, T. Klafka, K. Audo, A. Aspect, C. I. Westbrook, and D. Clément, "Three-dimensional laser cooling at the doppler limit," *Phys. Rev. A*, vol. 90, p. 063407, 2014.

[132] I. Ferrier-Barbut, M. Delehaye, S. Laurent, A. T. Grier, M. Pierce, B. S. Rem, F. Chevy, and C. Salomon, "A mixture of Bose and Fermi superfluids," *Science*, vol. 345, p. 1035, 2014.

[133] X.-C. Yao, H.-Z. Chen, Y.-P. Wu, X.-P. Liu, X.-Q. Wang, X. Jiang, Y. Deng, Y.-A. Chen, and J.-W. Pan, "Observation of coupled vortex lattices in a mass-imbalance Bose and Fermi superfluid mixture," *Phys. Rev. Lett.*, vol. 117, p. 145301, 2016.

[134] R. Roy, A. Green, R. Bowler, and S. Gupta, "Two-element mixture of Bose and Fermi superfluids," *arXiv:1607.03221*, 2016.

[135] M. Cetina, M. Jag, R. S. Lous, J. T. M. Walraven, R. Grimm, R. S. Christensen, and G. M. Bruun, "Decoherence of impurities in a Fermi sea of ultracold atoms," *Phys. Rev. Lett.*, vol. 115, p. 135302, 2015.

[136] C.-H. Wu, I. Santiago, J. W. Park, P. Ahmadi, and M. W. Zwierlein, "Strongly interacting isotopic Bose-Fermi mixture immersed in a Fermi sea," *Phys. Rev. A*, vol. 84, p. 011601(R), 2011.

[137] S.-K. Tung, C. Parker, J. Johansen, C. Chin, Y. Wang, and P. S. Julienne, "Ultracold mixtures of atomic ^{6}Li and ^{133}Cs with tunable interactions," *Phys. Rev. A*, vol. 87, p. 010702(R), 2013.

[138] M. Repp, R. Pires, J. Ulmanis, R. Heck, E. D. Kuhnle, M. Weidemüller, and E. Tiemann, "Observation of interspecies ^{6}Li-^{133}Cs Feshbach resonances," *Phys. Rev. A*, vol. 87, p. 010701(R), 2013.

[139] G. Roati, F. Riboli, G. Modugno, and M. Inguscio, "Fermi-Bose quantum degenerate ^{40}K-^{87}Rb mixture with attractive interaction," *Phys. Rev. Lett.*, vol. 89, p. 150403, 2002.

[140] D. J. McCarron, H. W. Cho, D. L. Jenkin, M. P. Köppinger, and S. L. Cornish, "Dual-species Bose-Einstein condensate of ^{87}Rb and ^{133}Cs," *Phys. Rev. A*, vol. 84, p. 011603(R), 2011.

[141] P. S. Żuchowski, J. Aldegunde, and J. M. Hutson, "Ultracold RbSr molecules can be formed by magnetoassociation," *Phys. Rev. Lett.*, vol. 105, p. 153201, 2010.

[142] D. A. Brue and J. M. Hutson, "Magnetically tunable Feshbach resonances in ultracold Li-Yb mixtures," *Phys. Rev. Lett.*, vol. 108, p. 043201, 2012.

[143] D. A. Brue and J. M. Hutson, "Prospects of forming ultracold molecules in $^{2}\Sigma^{+}$ states by magneto-association of alkali-metal atoms with Yb," *Phys. Rev. A*, vol. 87, p. 052709, 2013.

[144] A. Khramov, A. Hansen, W. Dowd, R. J. Roy, C. Makrides, A. Petrov, S. Kotochigova, and S. Gupta, "Ultracold heteronuclear mixture of ground and excited state atoms," *Phys. Rev. Lett.*, vol. 112, p. 033201, 2014.

[145] W. Dowd, R. J. Roy, R. K. Shrestha, A. Petrov, C. Makrides, S. Kotochigova, and S. Gupta, "Magnetic field dependent interactions in an ultracold Li-Yb($^{3}P_{2}$) mixture," *New. J. Phys.*, vol. 17, p. 055007, 2015.

[146] M. L. González-Martínez and J. M. Hutson, "Magnetically tunable Feshbach resonances in Li+Yb(3PJ)," *Phys. Rev. A*, vol. 88, p. 020701(R), 2013.

[147] A. Petrov, C. Makrides, and S. Kotochigova, "Magnetic control of ultracold ^{6}Li and ^{174}Yb(^{3}P$_{2}$) atom mixtures with Feshbach resonances," *New. J. Phys.*, vol. 17, p. 045010, 2015.

[148] J. S. Cohen, R. L. Martin, and N. F. Lane, "Theoretical calculation of Penning-ionization cross sections for collisions of He ($2^{1,3}$S) with sodium atoms," *Phys. Rev. A*, vol. 31, p. 152, 1985.

[149] K. F. Scheibner, J. S. Cohen, R. L. Martin, and N. F. Lane, "Role of atomic resonances in the ionization of potassium atoms in slow collisions with He ($2^{1,3}$S)," *Phys. Rev. A*, vol. 36, p. 2633, 1987.

[150] A. Merz, M. Müller, M.-W. Ruf, and H. Hotop, "Experimental and theoretical studies of simple attractive Penning ionization systems," *Chem. Phys.*, vol. 145, p. 219, 1990.

[151] M. Movre, L. Thiel, and W. Meyer, "Theoretical investigation of the autoionization process in molecular collision complexes: He*(2^3S)+Li(2^2S)→He+Li^++e^-," *J. Chem. Phys.*, vol. 113, p. 1484, 2000.

[152] A. S. Flores, W. Vassen, and S. Knoop, "Quantum-state controlled Penning-ionization reactions between ultracold alkali-metal and metastable helium atoms," *Phys. Rev. A*, vol. 94, p. 050701(R), 2016.

[153] J. Söding, D. Guéry-Odelin, P. Desbiolles, F. Chevy, H. Inamori, and J. Dalibard, "Three-body decay of a rubidium Bose-Einstein condensate," *Appl. Phys. B*, vol. 69, p. 257, 1999.

[154] A. Marte, T. Volz, J. Schuster, S. Dürr, G. Rempe, E. G. M. van Kempen, and B. J. Verhaar, "Feshbach resonances in rubidium 87: Precision measurement and analysis," *Phys. Rev. Lett.*, vol. 89, p. 283202, 2002.

[155] J. S. Borbely, R. van Rooij, S. Knoop, and W. Vassen, "Magnetic-field-dependent trap loss of ultracold metastable helium," *Phys. Rev. A*, vol. 85, p. 022706, 2012.

[156] Z. Idziaszek and P. S. Julienne, "Universal rate constants for reactive collisions of ultracold molecules," *Phys. Rev. Lett.*, vol. 104, p. 113202, 2010.

[157] J. Ulmanis, S. Häfner, R. Pires, F. Werner, D. S. Petrov, E. D. Kuhnle, and M. Weidemüller, "Universal three-body recombination and Efimov resonances in an ultracold Li-Cs mixture," *Phys. Rev. A*, vol. 93, p. 022707, 2016.

[158] A. H. Hansen, A. Khramov, W. H. Dowd, A. O. Jamison, B. Plotkin-Swing, R. J. Roy, and S. Gupta, "Production of quantum-degenerate mixtures of ytterbium and lithium with controllable interspecies overlap," *Phys. Rev. A*, vol. 87, p. 013615, 2013.

[159] J. M. Hutson, "Feshbach resonances in ultracold atomic and molecular collisions: threshold behaviour and suppression of poles in scattering lengths," *New J. Phys.*, vol. 9, p. 152, 2007.

[160] P. S. Julienne and F. H. Mies, "Collisions of ultracold trapped atoms," *J. Opt. Soc. Am. B*, vol. 6, p. 2257, 1989.

[161] G. Quéméner and P. S. Julienne, "Ultracold molecules under control!," *Chem. Rev.*, vol. 112, p. 4949, 2012.

[162] S. Knoop, F. Ferlaino, M. Mark, M. Berninger, H. Schöbel, H.-C. Nägerl, and R. Grimm, "Observation of an Efimov-like resonance in ultracold atom-dimer scattering," *Nature Phys.*, vol. 5, p. 227, 2009.

[163] S. Ospelkaus, K.-K. Ni, D. Wang, M. H. G. de Miranda, B. Neyenhuis, G. Quéméner, P. S. Julienne, J. L. Bohn, D. S. Jin, and J. Ye, "Quantum-state controlled chemical reactions of ultracold potassium-rubidium molecules," *Science*, vol. 327, p. 853, 2010.

[164] S. Knoop, F. Ferlaino, M. Berninger, M. Mark, H.-C. Nägerl, R. Grimm, J. P. DIncao, and B. D. Esry, "Magnetically controlled exchange process in an ultracold atom-dimer mixture," *Phys. Rev. Lett.*, vol. 104, p. 053201, 2010.

[165] R. V. Krems, "Cold controlled chemistry," *Phys. Chem. Chem. Phys.*, vol. 10, p. 4079, 2008.

[166] B. Gao, "Universal model for exoergic bimolecular reactions and inelastic Processes," *Phys. Rev. Lett.*, vol. 105, p. 263203, 2010.

[167] K. Jachymski, M. Krych, P. S. Julienne, and Z. Idziaszek, "Quantum theory of reactive collisions for $1/r^n$ potentials," *Phys. Rev. Lett.*, vol. 110, p. 213202, 2013.

[168] A. B. Henson, S. Gersten, Y. Shagam, J. Narevicius, and E. Narevicius, "Observation of resonances in Penning ionization reactions at sub-kelvin temperatures in merged beams," *Science*, vol. 338, p. 234, 2012.

[169] H. L. Hickling, L. A. Viehland, D. T. Shepherd, P. Soldán, E. P. F. Lee, and T. G. Wright, "Spectroscopy of M^+Rg and transport coefficients of M^+ in Rg (M=Rb-Fr; Rg=He-Rn)," *Phys. Chem. Chem. Phys.*, vol. 6, p. 4233, 2004.

[170] W. H. Miller, "Theory of Penning ionization. I. Atoms," *J. Chem. Phys.*, vol. 52, p. 3563, 1970.

[171] K. Jachymski, M. Krych, P. S. Julienne, and Z. Idziaszek, "Quantum-defect model of a reactive collision at finite temperature," *Phys. Rev. A*, vol. 90, p. 042705, 2014.

[172] H. T. C. Stoof, J. M. C. A. Koelman, and B. J. Verhaar, "Spin-exchange and dipole relaxation rates in atomic hydrogen: Rigorous and simplified calculations," *Phys. Rev. B*, vol. 38, p. 4688, 1988.

[173] J. M. Hutson, M. Beyene, and M. L. González-Martínez, "Dramatic reductions in inelastic cross sections for ultracold collisions near Feshbach resonances," *Phys. Rev. Lett.*, vol. 103, p. 163201, 2009.

[174] Z. Idziaszek and P. S. Julienne, "Multichannel quantum-defect theory for ultracold atom-ion collisions," *New J. Phys.*, vol. 13, p. 083005, 2011.

[175] T. Schuster, R. Scelle, A. Trautmann, S. Knoop, M. K. Oberthaler, M. M. Haverhals, M. R. Goosen, S. J. J. M. F. Kokkelmans, and E. Tiemann, "Feshbach spectroscopy and scattering properties of ultracold Li+Na mixtures," *Phys. Rev. A*, vol. 85, p. 042721, 2012.

[176] T. G. Tiecke, M. R. Goosen, J. T. M. Walraven, and S. J. J. M. F. Kokkelmans, "Asymptotic-bound-state model for Feshbach resonances," *Phys. Rev. A*, vol. 82, p. 042712, 2010.

[177] M. R. Goosen, T. G. Tiecke, W. Vassen, and S. J. J. M. F. Kokkelmans, "Feshbach resonances in ^{3}He*-^{4}He* mixtures," *Phys. Rev. A*, vol. 82, p. 042713, 2010.

[178] P. Raab and H. Friedrich, "Quantization function for deep potentials with attractive tails," *Phys. Rev. A*, vol. 78, p. 022707, 2008.

List of Publications

As chapter (or part) of this thesis:

A.S. Flores, H.P. Mishra, W. Vassen, and S. Knoop. "An ultracold, optically trapped mixture of ^{87}Rb and metastable ^{4}He atoms." *European Physical Journal D*, 71: 49, 2017.

A.S. Flores, W. Vassen, and S. Knoop. "Quantum-state-controlled Penning-ionization reactions between ultracold alkali-metal and metastable helium atoms." *Physical Review A*, 94: 050701(R), 2016.

A.S. Flores, H.P. Mishra, W. Vassen, and S. Knoop. "Simple method for producing Bose-Einstein condensates of metastable helium using a single-beam optical dipole trap." *Applied Physics B*, 121: 391, 2015.

H.P. Mishra, A.S. Flores, W. Vassen, and S. Knoop. "Efficient production of an ^{87}Rb F=2, m_F=2 Bose-Einstein condensate in a hybrid trap." *European Physical Journal D*, 69: 52, 2015.

S. Knoop, P.S. Żuchowski, D. Kędziera, Ł. Mentel, M. Puchalski, H.P. Mishra, A.S. Flores, and W. Vassen. "Ultracold mixtures of metastable He and Rb: Scattering lengths from *ab initio* calculations and thermalization measurements." *Physical Review A*, 90: 022709, 2014.

Co-authored paper but not part of this thesis:

F.M.J. Cozijn, J. Biesheuvel, A.S. Flores, W. Ubachs, G. Blume, A. Wicht, K. Paschke, G. Erbert, and J.C.J. Koelemeij. "Laser cooling of beryllium ions using a frequency-doubled 626 nm diode laser." *Optics Letters*, 38: 2370, 2013.

509242-L-bw-Flores
Processed on: 3-4-2017

Summary

The exquisite control of the internal and external degrees of freedom makes ultracold atomic samples an ideal platform to study various fascinating physical phenomena, examples of which can be found in few-body physics such as the observation of Efimov quantum states and many-body physics where ultracold samples could be used to simulate condensed-matter systems. The ultracold regime implies samples that are below a millikelvin, and to reach these temperatures, techniques such as laser cooling, magneto-optical trapping, and evaporative cooling in a magnetic or optical trap are employed. Sample temperatures can even reach below a microkelvin and surpass a critical limit such that Bose-Einstein condensation (bosons) or a quantum degenerate Fermi gas (fermions) is realized. Experiments with ultracold samples are not limited to single atomic species but also involve chemically distinct atomic mixtures, application for example is the creation of ultracold heteronuclear molecules. Mostly, ultracold mixtures consist of alkali atoms while recently also mixtures between alkali and alkaline-earth atoms are explored.

The main goal of the experiment described in this thesis is to realize an ultracold mixture of helium (in its metastable state: ^{4}He*) and rubidium (^{87}Rb) atoms in an optical dipole trap. Generally, mixtures between alkali and metastable helium atoms are still unexplored and prior to this experiment, trapping in an optical dipole trap had not been achieved. Pure optical trapping allows trapping of atoms in any spin state and is essential in applications where the interaction requires tuning using an external magnetic field via a so-called Feshbach resonance. The application of metastable helium in ultracold atom experiment could provide an extended range of possible mass ratios for heteronuclear mixtures. The metastable state of helium is used for laser cooling as ground state atoms cannot be directly laser cooled because the wavelength needed is in the extreme ultraviolet and no laser is available at that wavelength. The metastable state cannot decay directly to the ground state and has a lifetime of approximately 8000 s, which is more than sufficient to perform any (ultra)cold atom experiment. Another important property of metastable helium is the large internal energy of 19.8 eV. This provides a strong inelastic two-body process known as Penning ionization, which limits the trapping lifetime, however is strongly suppressed for

a mixture prepared in a doubly spin-stretched state. The Penning ionization reactions, in mixtures prepared in various spin-state combinations, have been investigated in a single-beam optical dipole trap by measuring trapping lifetimes. Details of this experiment are presented in Chapter 5, where control of Penning-ionization reactions by internal atomic state preparation was demonstrated.

The approach to realize an ultracold sample is based on a relatively simple scheme that starts with laser cooling and magneto-optical trapping to slow down, collect and cool atoms from basically room temperature. In the experiment, $10^8 - 10^9$ atoms are confined at temperatures between 1 and 2 millikelvin (^{4}He*) and a few hundreds microkelvin (^{87}Rb) in a magneto-optical trap. To efficiently transfer atoms into an optical dipole trap, the sample is first transferred to a pure quadrupole magnetic trap, which is the simplest configuration among magnetic traps. Forced evaporative cooling is performed by lowering the quadrupole magnetic trap depth in a controlled way such that the more energetic atoms can escape and the remaining atoms rethermalize to a lower temperature. Afterward the sample is transferred into a single-beam optical dipole trap via a recently invented scheme known as a hybrid trap, which is simply a single-beam optical dipole trap combined with a weak quadrupole magnetic trap. In the hybrid trap or single-beam optical dipole trap, typical sample temperatures for both Rb and He* reach below 25 microkelvin.

One major limitation of using a quadrupole magnetic trap is the presence of Majorana spin-flips at the bottom of the trap, which limits the lowest temperature that can be achieved by evaporative cooling and puts constraints on the subsequent transfer into an optical dipole trap. The Majorana effect scales inversely with mass and is more pronounced for light atomic species such as helium. In fact, it is for this reason that the hybrid trap scheme is applied mostly to heavy atomic species such as rubidium. Furthermore, in the hybrid trap scheme the weak quadrupole magnetic field gradient should provide a force that is equal or lower than the force due gravity, which is known as the levitation gradient, to ensure that atoms are confined by the single-beam optical dipole trap and not by the weak quadrupole magnetic trap. Thus, for light atomic species the extra confinement provided by the weak quadrupole magnetic gradient is also limited due to the small levitation gradient.

In a single species preparation, sufficiently low temperature could be reached (below 1 microkelvin) such that Bose-Einstein condensation of ^{87}Rb atoms was achieved using the hybrid trap scheme. Similarly, also Bose-Einstein condensation of ^{4}He* atoms was realized both in the hybrid trap and in a single-beam optical trap (details of the experiment are discussed in Chapter 3), which is a remarkable achievement given the constraints mentioned earlier. However, in the mixture preparation (details are presented in Chapter 4), the additional interspecies losses and constraints due to the

Majorana effect reduced the transfer efficiency into the hybrid trap or single-beam optical dipole trap by at least an order of magnitude compared to the single-species preparation. The limited number of atoms of both species hinders further forced evaporative cooling in the hybrid trap or single-beam optical trap towards dual Bose-Einstein condensation. In Chapter 6, changes in the existing experimental setup that can improve the transfer efficiency of the mixture into the single-beam optical dipole trap are proposed.

The work described in this thesis did not only demonstrate the first realization of an optically trapped ultracold mixture of an alkali and metastable helium atoms but also triggered theoretical work about the scattering properties of this mixture. For instance, *ab initio* calculations of the interaction potentials have been performed for various alkali (Li, Na, K and Rb) and metastable helium (^{3}He* and ^{4}He*) combinations revealing important information such as the scattering lengths, which is in good agreement with experiments (for example in ^{87}Rb and ^{4}He* mixture). In addition, the detailed outline of the experimental issues and features presented in this thesis, for example the successful application of simultaneous microwave (^{87}Rb) and radiofrequency (^{4}He*) based forced evaporative cooling in the magnetic trap, will guide future experiments using these type of mixtures. Moreover, from the observed near-universal loss and dependence of the Penning ionization reaction on the internal state preparation of the atoms, one can estimate the two-body losses in other alkali and metastable helium isotope combinations.

509242-L-bw-Flores
Processed on: 3-4-2017

Samenvatting

Ultrakoude atomaire gaswolkjes zijn een ideaal platform om verschillende fascinerende fysische fenomenen experimenteel te bestuderen vanwege de hoge mate van controle over de interne en externe vrijheidsgraden. Voorbeelden kunnen worden gevonden in weinig-deeltjes fysica, zoals de ontdekking van Efimov quantum driedeeltjes toestanden, en in veel-deeltjes fysica voor het simuleren van gecondenseerde materie systemen. Het ultrakoude regime betekent een gaswolkje van atomen onder de millikelvin, en om deze lage temperaturen te bereiken worden experimentele technieken zoals laserkoeling en verdampingskoeling in een magneet of optische dipool val gebruikt. Temperaturen onder de microkelvin zijn zelfs haalbaar, waarbij de kritische grens voor Bose-Einstein condensatie (bosonen) of een quantum ontaard Fermi gas (fermionen) bereikt kan worden. Experimenten met ultrakoude atomaire gassen bevatten vaak een enkele atoomsoort, maar ook mengsels van meerdere atoomsoorten zijn mogelijk. Toepassingen zijn bijvoorbeeld het creëren van ultrakoude heteronucleaire moleculen. Deze ultrakoude mengsels bevatten meestal alkalimetalen, maar sinds kort zijn ook mengsels met alkali- en aardalkalimetalen in gebruik.

Het hoofddoel van de experimenten die in dit proefschrift beschreven zijn, is het realiseren van een ultrakoud mengsel van helium (in een metastabiele aangeslagen toestand, ^{4}He*) en rubidium (^{87}Rb) atomen in een optische dipool val. Mengsels van alkalimetalen en metastabiel helium atomen zijn amper bestudeerd en bij de start van dit experiment was het opsluiten van zo'n mengsel in een optische dipool val ook nog niet gerealiseerd. In een optische dipool val kunnen atomen worden opgesloten onafhankelijk van de spin toestand. Verder geeft dit de mogelijkheid om een magneetveld aan te leggen, wat de mogelijkheid geeft voor het experimenteel instellen van de interatomaire interactie door middel van zogenaamde Feshbach resonanties.

De toepassing van het lichte helium zorgt voor een uitgebreidere schaal van mogelijke massa-verhoudingen voor ultrakoude mengsels van twee atoomsoorten. De metastabiele toestand van helium wordt gebruikt aangezien laserkoeling niet kan worden toegepast op de grondtoestand door de afwezigheid van een laser bij de benodigde extreem ultraviolette golflengte. De metastabiele aangeslagen toestand kan niet rechtstreeks vervallen naar de grondtoestand en heeft een lange levensduur van ongeveer

8000 s, wat meer dan genoeg is om experimenten met (ultra)koude atomen uit te voeren. Een andere belangrijke eigenschap van metastabiel helium is de hoge interne energie van 19.8 eV. Dit resulteert in een sterk inelastisch twee-deeltjes proces, bekend als Penning ionisatie, wat de levensduur in de val limiteert. Dit proces is echter sterk onderdrukt als het mengsel is gepreppareerd in de maximale spin toestand. In dit werk zijn de Penning-ionisatie reacties voor verschillende spin toestand combinaties onderzocht, door de levensduur van het mengsel in de optische dipool val te meten. Details van dit experiment zijn gepresenteerd in Hoofdstuk 5, waarbij de controle over Penning-ionisatie reacties door middel van interne atomaire toestand preparatie was gedemonstreerd.

De aanpak om een ultrakoud mengsel te realiseren is gebaseerd op een relatief eenvoudig schema dat begint met laserkoeling om atomen van kamertemperatuur af te remmen, te verzamelen en af te koelen. In een magneto-optische val worden $10^8 - 10^9$ atomen opgesloten bij temperaturen tussen de 1 en 2 millikelvin (^{4}He*) en een paar honderd microkelvin (^{87}Rb). Om efficiënt atomen in een optische dipool val om te laden, worden de atomen eerst in een simpele quadrupool magneetval geladen. Geforceerde verdampingskoeling wordt gedaan door het gecontroleerd verlagen van de diepte van de magneetval zodat de meest energetische atomen kunnen ontsnappen en achtergebleven atomen thermaliseren naar een lagere temperatuur. Daarna worden de atomen overgebracht naar een optische dipool val via een recent uitgevonden schema, bekend als een hybride val, bestaande uit de combinatie van een optische dipool val en een zwakke magnetische val. In de hybride of pure optische dipool val liggen de typische temperaturen voor zowel ^{4}He* als ^{87}Rb onder de 25 microkelvin.

Een grote beperking voor het gebruik van een quadrupool magneet val is de mogelijkheid van Majorana spin-flips rond de bodem van val, wat een beperking geeft aan de laagst mogelijke temperatuur die met verdampingskoeling bereikbaar is, en daarmee ook het efficiënt laden van een optische dipool val. Het Majorana effect schaalt omgekeerd evenredig met de massa en speelt dus een grotere rol voor lichtere atoomsoorten, zoals helium. In feite is dit de reden dat de hybride val vooral wordt toegepast op zwaardere atoomsoorten, zoals rubidium. Bovendien, in de hybride val moet de zwakke magneetveld gradiënt gelijk zijn aan of zwakker zijn dan de levitatie gradiënt, waarbij de magneetveld kracht die op de atomen werkt de zwaartekracht compenseert, waardoor de atomen ook echt zijn opgesloten door de optische dipool val component van de hybride val. Aangezien lichte atoomsoorten een kleine levitatie gradiënt hebben, is de additionele opsluiting van de zwakke magneetval zeer beperkt, in vergelijking tot zwaardere atoomsoorten.

In experimenten met alleen ^{87}Rb atomen konden voldoende lage temperaturen worden bereikt (onder 1 microkelvin) in de hybride val zodanig dat Bose-Einstein condensatie werd gerealiseerd. Op dezelfde wijze is ook

Bose-Einstein condensatie van ^{4}He* atomen gelukt, in zowel de hybride val als de pure optische dipool val (details van het experiment zijn besproken in Hoofdstuk 3), wat een uitzonderlijke prestatie is gezien de al eerder besproken beperkingen. Echter, in de preparatie van het mengsel (details gepresenteerd in Hoofdstuk 4), bijkomende interspecies verliezen en beperkingen door het Majorana effect, verlaagde de transfer efficiëntie naar de hybride val of optische dipool val met zeker een orde-grootte in vergelijking met experimenten met alleen helium of rubidium atomen. De beperkte aantallen atomen van beide atoomsoorten belemmert verdere geforceerde verdampingskoeling in de hybride val of optische dipool val naar Bose-Einstein condensatie. In Hoofdstuk 6 zijn veranderingen in de bestaande experimentele opstelling voorgesteld die de transfer efficiëntie van het mengsel naar de optische dipool val kan verbeteren.

Het werk beschreven in dit proefschrift demonstreert niet alleen de eerste realisatie van een optisch gevangen ultrakoud mengsel van alkali en metastabiel helium atomen, maar heeft ook aangezet tot theoretisch werk aan de botsingseigenschappen van dit mengsel. Bijvoorbeeld, *ab initio* berekeningen van de interactie potentialen zijn uitgevoerd voor bijna alle alkalimetalen (Li, Na, K en Rb) en metastabiel helium (^{3}He* en ^{4}He*) combinaties, met als uitkomst belangrijke informatie over de verstrooiingslengtes, welke goed overeenkomt met onze experimenten (voor het ^{87}Rb en ^{4}He* mengsel). Bovendien zal de gedetailleerde beschrijving van experimentele kwesties en kenmerken zoals gepresenteerd in dit proefschrift, bijvoorbeeld het succesvol toepassen van gelijktijdig microgolf (^{87}Rb) en radiofrequentie (^{4}He*) gebaseerde verdampingskoeling in de magneetval, toekomstige experimenten met dit type mengsels sturen. Daarbij kan men, uit de gemeten bijna-universele twee-deeltjes verliezen en afhankelijkheid van de Penning ionisatie reacties met de interne toestand preparatie, een inschatting maken van deze verliezen voor combinaties van andere alkalimetalen met metastabiel helium.

509242-L-bw-Flores
Processed on: 3-4-2017

Acknowledgements

Learning is an endless journey for search of knowledge and self-realization. The last four years has been a great part of that journey which provided me a high level of experience and challenges in both professional and personal aspects. Interacting and working with culturally diverse individuals helped widened my perspective beyond my usual boundaries which made me a better person. In these last few pages, I would like to take the opportunity of expressing my gratitude to everyone who in one way or another has influenced in achieving the completion of this PhD thesis.

I am indebted to my supervisor Steven Knoop. Thank you for giving me the opportunity to work in the project despite the limited background I had in the beginning. I worked with experimental plasma physics during my masters which is a bit far from the field of this study, but, the first few words that you told me were reassuring. You mentioned that the reason a PhD is 4 years, is because it is a learning process which I will gain and develop along the way. Those words gave me the confidence I needed. Thank you for providing the direction and support, they were essential in the completion of my PhD study and this thesis. Indeed, the important learning and experience I have while working with you will certainly be an asset in my future endeavours.
To my co-supervisor, Wim Vassen. Thank you also for the supervision and insights about our experiment, the comments and suggestions in our published manuscripts and this thesis. The sub-group meetings we have were helpful not only for the scientific discussions but also, they served as venues for me to learn how to express myself. I may still need to work on my social skill, but compared to 4 years ago, I think it has quite improved. To my promotor, Wim Ubachs, thank you for the opportunity and for the additional administrative work you have done both during my PhD and my short visit in the Lab prior to the PhD period. To Jeroen Koelemeij, thank you too for the opportunity to work with your project during the short visit before the PhD. I am privileged to have partly contributed to the work that had led to one of my co-authored publications. Steven once mentioned, that the 1 week you allowed me to work in his project that time was a way of assessment. That turn of event I believe had been a significant contributing

factor for Steven to offer me the position. To Edcel Salumbides, thank you also for all the support and advices. You are not only a friend but also a good mentor as well. The discussions we have about my experiment certainly offered additional guidance; made me think from a different perspective; and helped me find solutions to some experimental issues we encountered.
To Hari Mishra, I really appreciate working with you. Operating our experiment is complex, in the first year it was a bit overwhelming but you were there to help me out and build up my confidence. Thank you and I wish you success in your endeavours as well. To Tim Berrier and Tim van Leent, thank you too for your contributions. I also acknowledge our collaborators, Piotr Żuchowski, Dariusz Kędziera, Łukasz Mentel, and Mariusz Puchalski for their theoretical work. To Remy Notermans, Bob Rengelink and Ruud van der Beek, thank you for both the professional and "the other" discussions we shared together. I think it helped improved my social skill. We shared a lot of things, from lasers to electronics, and unfortunately including our scattered lights (but at least they are reduced to a minimum). To Itan Barmes, thank you for the help when we needed a temporary place to live after our first month here in the Netherlands. We knew that housing in Amsterdam is difficult, however, we are very thankful that you vouched for us to be able stay in your friend's apartment. To all my colleagues in the LaserLab, thank you very much for the warm and friendly atmosphere. The cakes and the 'borrels' are really nice. I am very glad to have worked in our Lab. To Rob Kortekaas, thank you for the technical support. I owe you chapters 4 and 5 of this thesis. If not for your quick response and solution to the unfortunate and unexpected breakdown of some parts in our experimental setup, we would have not been able to finish our latest measurements in time. To Jacques Bouma, and the people from electronics and mechanical workshop, thank you too for the technical support.
To Gerrit Kuik and Mel Bacabac. Thank you for arranging my initial visit in the LaserLab at the VU. The exposure to the experiments offered valuable knowledge and experience in preparation for this major growth of my personal development. It had been significant in making this career achievement a reality. To Gerrit, May Ann and kids, I (and Jane) am very grateful for the support you have provided, the winter clothes that kept us warm during our first snowy experience and the invitation at your place for one of our first summer barbecue events. We still remember that when we arrive in the Netherlands in 2012, you came to meet us in the airport despite the early morning arrival and made sure we are settled in our apartment. To Dia Eek, thank you also for the administrative work you have done during my short visit in the Lab. To Marja Herronen, thank you for all the administrative assistance you have provided to us. As a foreigner, the first year I believe is the most difficult time but we are very glad that we can always drop by your office for questions and guidance.
To University of San Carlos, your support helped shape the advancement

of my career, thank you. To my colleagues at the Physics Department, the experiences with you certainly have influenced my academic profession. To Sir Ed and Maam Daday van den Berg, your commitment and enthusiasm to physics teaching have always inspired us. Thank you too for the warm hospitality, the invitations at your place, for always so happy to give us a tour in Alkmaar and for the fatherly and motherly assurance that we can reach out to you in case we need help especially when you knew we were moving to our 4th apartment that time. To Father Herman van Engelen, your perpetual dedication and continuous interest in physics inspire us as well.

To the 'bisdaks', Albert, Edcel, Marian, and Xavier, there may be no other place like home, but to me and Jane, with your friendship being like family, we feel at home. From Cebu to Amsterdam, it is a rare circumstance to be 'almost' working together until this time. Thank you for the unconditional camaraderie; for the understanding and respect of each other's differences and opinions; for the knowledge sharing, intellectual discussions, trust, advice, adventure and fun. To Marc and Joy, Onats and Yoli, it seems we have known you guys for long, thank you too for considering us like family. Marc and Joy, thank you for the support and help when we had to move apartments. Onats and Yoli, Ate Hermie and Piet, thank you too for the advice and tips about living in the Netherlands. Together with Kuya Eddie and Ate Connie, Ronald and Tessa, Carmi and Russell, Marites and Laurent, Danny and Rhoda, Nonong and Iris, the kiddos and Min, we are grateful to have known you all, it feels great to have fun, laughter and music in our get together parties.

To my family in the Philippines, Nanay and Tatay, Papa (and in memory of Mama), brothers, sisters, my in-laws, nephews and nieces, thank you for your support. Distance doesn't seem to matter, via technology, you have always involved us in the family gatherings which made us feel like we are just at home.

And to my wife Mary Jane, in all ways you inspire me.

509242-L-bw-Flores
Processed on: 3-4-2017

Tussenschiet vel: PAGINA WORDT VERWIJDERD IN EINDPRODUCT

Seperation sheet: PAGE WILL BE REMOVED IN FINAL PRODUCT

IPSKAMP printing
books and more

509242-L-bw-Flores
Processed on: 3-4-2017

Tussenschiet vel: PAGINA WORDT VERWIJDERD IN EINDPRODUCT

Seperation sheet: PAGE WILL BE REMOVED IN FINAL PRODUCT

IPSKAMP printing
books and more

509242-L-bw-Flores
Processed on: 3-4-2017